HIGH RESOLUTION INTERFEROMETRY OF

ASTROPHYSICAL OBJECTS

K.P. RAJU

PHYSICAL RESEARCH LABORATORY

AHMEDABAD

INDIA

043

B14747

A THESIS

SUBMITTED TO THE GUJARAT UNIVERSITY

FOR THE DEGREE OF
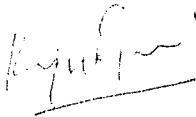
DOCTOR OF PHILOSOPHY

DEDICATED TO

My Parents

CERTIFICATE

I hereby declare that the work presented in this thesis is original and has not formed the basis for the award of any degree or diploma by any University or Institution.

Author

K. P. Raju

Physical Research Laboratory

Ahmedabad - 380 009

India.

Certified by

Thesis Supervisor

Prof. J. N. Desai

Physical Research Laboratory

Ahmedabad - 380 009

India.

The human mind is not capable of grasping the universe. We are like a little child entering a huge library. The walls are covered to the ceilings with books in many different tongues. The child knows that someone must have written these books. It does not know who or how. It does not understand the languages in which they are written. But the child notes a definite plan in the arrangement of books—a mysterious order which it does not comprehend, but only dimly suspects.

A.Einstein

Contents

Acknowledgements

Research Publications

1. Kinematics of Discrete Components in Solar Coronal Plasma in Relation to Coronal Magnetic Fields (1989). **K.P.Raju**, J.N.Desai, T.Chandrasekhar and N.M.Ashok Paper presented in the 13th ASI meeting held at Srinagar, India.

2. Fabry-Perot Interferogram Profiles in λ 5303 Å in Relation to Coronal Structures: 1980 and 1983 Eclipses (1990). J.N.Desai, **K.P.Raju**, T.Chandrasekhar, N.M.Ashok and J.M.Pasachoff 'Basic Plasma Processes on the Sun', p.251, (eds) E.R.Priest and V.Krishan, D.Reidel, Dordrecht.

3. The Excitation Mechanism of [FeXIV] 5303 Å line in the Inner Regions of Solar Corona (1991) **K.P.Raju**, J.N.Desai, T.Chandrasekhar and N.M.Ashok J.Astrophys.Astr., **12**, 311.

4. A Kinematic Study of Orion Nebula in the emission line [SII] λ 6731 Å (1992). T. Chandrasekhar, **K.P. Raju**, Debi Prasad and J.N. Desai. (To be communicated).

5. Line of sight Velocities in the Inner Corona (1992). **K.P.Raju**, J.N.Desai, T.Chandrasekhar and N.M.Ashok (In Preparation)

ABSTRACT

Astrophysical plasma is encountered over a wide range of circumstances, ranging from solar corona, cometary ion tails, planetary nebulae, HII regions, supernova remnants and a number of other scenarios. Emission line profile studies provide a convenient means of knowing the physical conditions like velocity fields, temperatures, turbulence, densities etc. This thesis deals with such a study, carried out in the case of two widely differing situations, namely the solar corona and an HII region–the Orion Nebula. Coronal plasma is a high temperature plasma with strong local magnetic fields ($\sim 10 - 10^2$ G) while HII region plasma is relatively cool with extremely weak magnetic fields ($\sim 10^{-6}$ G). Both are extended objects, fairly bright sources and hence make good objects for excellent ground based observations. Both of them emit strongly in visible forbidden lines. Fabry-Pérot spectrometer with its superior light collecting power and high spectral resolution, is an ideal instrument for the study of these objects.

The solar corona is the tenuous outer envelope of the Sun. It expands into the interplanetary medium and beyond, and in this form, is known as solar wind. The temperature of the solar atmosphere is found to increase from 6000 K in the photosphere to about 2×10^6 K in the corona. Due to its high temperature, most elements exist in the ionized form in the corona. The electron density is about $10^8 - 10^9$ cm^{-3} in the inner corona and decreases outwards. Recent observations stress the importance of the magnetic field in the energetics and dynamics of the corona (Withbroe & Noyes 1977). Throughout the corona, the ratio of material pressure to magnetic pressure (plasma β) is much less than one, and hence the magnetic field dominates the plasma. In fact, the various features in a coronal picture such as

streamers, coronal holes, polar rays and coronal loops manifest the underlying coronal magnetic fields. Another interesting feature of the corona is the changes associated with the 11 year solar cycle. A solar dynamo with a period of 22 years, operating from the interior of the Sun, is believed to be the mechanism behind it, though the details are not yet fully understood.

The drastic increase in temperature from the photosphere to the corona, remains as one of the most outstanding problems of solar physics. The high temperature of the corona was reported in 1942 from the identification of spectral lines from highly ionized atoms (Edlén 1942). It was generally accepted that shock wave dissipation could heat the solar atmosphere; however, space-borne measurements in recent years have convincingly shown that the shock wave flux cannot provide the required heating (Athay & White 1977). It is observationally found that the temperature of the active regions where the magnetic field is strong and predominantly closed, is higher than that of quiet regions where the magnetic field is weak and open. It is now generally accepted that coronal heating is a magnetic field related phenomena, but the exact mechanisms are not clear. Magnetic heating can be expected either due to the dissipation of magnetohydrodynamic waves and/or due to different current heating mechanisms in the regions of large electric current densities. The generation of electrodynamic energy arises when plasma is forced to flow across the magnetic field lines. The velocity spectrum in relation to the magnetic field is the most important deciding factor in accepting or rejecting a particular heating mechanism (Kuperus et al., 1981).

The thesis also deals with the studies of a different astrophysical situation-the interstellar matter. It is estimated that the interstellar matter contains 5–10 % of the total mass of a galaxy. The average particle density of the medium is 1 atom per

cm^{-3} , but often high concentrations ($\sim 10^3$ cm^{-3}) in the form of clouds are seen. When an early type (spectral type O or B) star is born in such a cloud, it ionizes the surrounding medium considerably by its copious supply of UV radiation. Such a region is known as an ionized hydrogen region or an HII region. Well known examples are the Orion (M42), Rosette, Trifid (M20) and Lagoon (M8) Nebulae. Interstellar clouds are 'stellar nurseries', where new stars are born and reared. The nearest such stellar nursery being the well known Orion Nebula. Kinematical studies of HII regions provide very valuable informations on star formation processes.

The thesis addresses the following problems;

- The nature of velocity fields in the inner solar corona and its relation to the magnetic field structure at the two epochs of solar activity cycle, one at a solar maximum phase and the other at a declining phase;

- The excitation mechanism of the coronal green line and its variations in different coronal regions;

- The kinematics of an HII region in the farthest regions from the ionizing star in the nebula.

The thesis is subdivided into seven chapters. In the following section, a brief summary of the individual chapters and the important results are discussed.

- Chapter 1.

  This chapter gives an introduction to the solar corona. The basic properties and various physical processes are discussed in some detail. Various coronal heating mechanisms, line emission processes and the need of observational inputs are also discussed. The relevance and the importance of the present study

is stressed.

- **Chapter 2.**

  This chapter deals with the instrumentation, observations and data reduction methods. The basic theory of Fabry-Pérot spectrometer and the photodigitizing system used are discussed. The observations on the solar corona were carried out by the Physical Research Laboratory group during the total solar eclipses of 1980 and 1983, using Fabry-Pérot techniques and coronal photography. The various steps involved in the data reduction are described in detail.

- **Chapter 3.**

  In this chapter, some of the results of the analysis of solar eclipse interferograms are given. Radial scans of the interferograms show considerable intensity at the line wings. The excess intensity in the wing regions were calculated in about 500 line profiles, following a procedure given by Chabbal (Chabbal 1953). The contribution of the continuum intensity to the wing regions of a Fabry-Pérot fringe was calculated for a typical coronal line profile. It was found that the excess intensity seen in the wing regions of Fabry-Pérot fringes is mainly due to the presence of fast moving (~100 km s^{-1}) discrete components in the corona. From the behavior of the wing intensity and the fringe peak intensity, we infer that the line excitation conditions existing in the coronal loops and the ambient medium are a function of the activity of the particular coronal region.

- **Chapter 4.**

  This chapter deals with the velocity field observed in the solar corona during 1980 and 1983 eclipses. The velocity fields in the corona were studied by a detailed analyses of the line profiles obtained from the eclipse interferograms. The

present study indicates that corona can be viewed as made up of, an ambient plasma medium with embedded discrete moving components associated with the coronal loop plasma. The velocity fields in the corona show large differences at the solar maximum phase of 1980 and at the declining phase of 1983. It was also found that the velocity fields depend upon the detailed magnetic structure of the corona. A typical coronal line profile was modelled to study the effects of mass motions in the corona. The model line profile successfully explains the main features in the observed line profiles.

- Chapter 5.

  This chapter deals with the excitation mechanism of the coronal green line and the line to continuum ratios observed in various coronal regions. Line to continuum ratios were derived from a narrow band filtergram and a white light photograph of the solar corona, obtained during the 1980 total solar eclipse. These values were then compared with the theoretically calculated line to continuum ratios. It was found that collisional mechanisms dominate the line excitation in the inner corona (1.4 $R_\odot$) while radiative mechanisms become predominant outwards.

- Chapter 6.

  This chapter deals with the observations, data reduction and results on the Orion HII region. An imaging Fabry-Pérot interferometric observation was carried out on the Orion Nebula in the emission line [SII]λ6731, to study the kinematics of the HII region. The relative line of sight velocities were calculated at about 1500 points on the face of the nebula in a $6' \times 6'$ field around the Trapezium stars. Evidences of jet phenomena were seen at some locations in the nebula which could be due to the out flows from the embedded protostars.

- Chapter 7.

This chapter gives the conclusions of the present study and some directions for future work in the field.

Chapter 1

Introduction

Solar corona is the outermost solar atmosphere, which is seen as a tenuous halo around the Sun during solar eclipse; it expands into the interplanetary medium and beyond and in this form, known as the solar wind. The three components of solar corona are, the K-corona which arises due to the scattering of photospheric light by electrons, the E-corona which is the component due to emission spectral lines and the F-corona which arises due to the scattering of light by dust particles in the interplanetary medium.

1.1   A Brief History of Coronal Science

The oldest recorded observation of solar corona, seen in the old Chinese reports, dates back to more than 4000 years. One of the most famous antique eclipses reported is that which occurred in Thales in 585 BC and about which Herodotus writes in 'History' that 'the day suddenly changed into night'. Hipparchus, the famous Greek

1

astronomer, used eclipse observations to estimate the moon's distance from the earth in 130 BC. The first western astronomer to comment about the appearance of the solar corona was Kepler. Galileo observed sunspots with the newly invented telescope in the beginning of the 17th century. Halley made observations on solar corona during the eclipse of 1715. However, the wide spread attention of the astronomers turned towards corona, after Bailey's report on Bailey's beads in around 1842. The main debate in the following years was whether the corona is really a part of the Sun or not (Zirker 1980).

In 1860s Kirchoff and Bunsen mapped the solar spectrum and identified a number of terrestrial elements in the Sun. Many coronal lines were known by the end of 19th century, but no identification with a terrestrial element was possible. A new element Coronium was postulated to account for them. Meanwhile, the spectra of gaseous nebulae were found to contain many emission lines which defied identification and a hypothetical element Nebulium was proposed as their possible source of emission. This riddle was ultimately solved by Bowen, who identified some of the strongest nebular lines as forbidden lines of singly and doubly ionized oxygen and singly ionized nitrogen. In 1935, he identified some puzzling lines in the spectrum of Nova Pictoris 1925 as forbidden lines emitted by iron atoms which were missing five or six outer electrons. During this time Adams and Joy at the Mt. Wilson observatory, identified five solar coronal lines in the spectra of Nova Ophiuchus. In 1939, Grotrian attributed the coronal red line to FeX. Edlén by 1942, had identified 19 of the 27 known coronal emission lines as forbidden transitions in highly ionized atoms such as Ca, Fe and Ni. The existence of a million degree corona was immediately established.

Some of the important developments in coronal science are listed below (Priest

1984).

1814: Fraunhofer discovered most of the first 547 lines in the solar spectrum.

1836: A systematic study of solar eclipse was begun.

1843: Schwabe proposed the existence of the 11 year sunspot cycle.

1851: Corona was photographed for the first time.

1858: Carrington discovered the latitude drift of sunspots during a solar cycle.

1868: Secchi detected emission line of a new line, which was given the name helium.

1875: Secchi discovered that the form of the corona changes during solar cycle.

1889: Hale invented spectroheliograph.

1908: Hale discovered solar magnetic fields in sunspots.

1930: Lyot invented coronagraph.

1939: Grotrian attributed the coronal red line to FeX emission.

1940: Edlén identified the coronal green line.

1942: Alfvén gave a theory for magnetic waves.

1948: Biermann and Schwarzchild proposed that the outer solar atmosphere is heated
by acoustic waves that propagate from the convection zone.

1958: Parker predicted the existence of solar wind.

Chapman (1957) suggested that corona extends to Earth's orbit and beyond, and is supported by hydrostatic balance. Parker (1960) showed that corona must expand into the interplanetary medium hydrodynamically and the resulting flow could reach a supersonic speed of several hundred kilometers per second. Parker's predictions were confirmed by the Mariner spacecraft measurements within a few years. A series of Orbiting Solar Observatories (OSO) were launched by NASA in the sixties. Coronal holes were detected from one such measurements and it was found that the high speed solar wind originates from them. Subsequently, in 1973 NASA launched Skylab, a manned solar observatory. OSO 8 was launched in 1975, which carried an ultraviolet spectrometer. Athay and White concluded from the above measurements that all the oscillatory energy from the solar photosphere dissipates in the lower chromosphere itself (Zirker 1980, Priest 1984).

1.2   Coronal Electron Density

One of the most well studied physical parameters associated with corona is the electron density. It can be measured by a variety of techniques such as coronal photometry, radio-source occultation measurements and spacecraft measurements. The coronal photometric technique is based upon the assumption that K-corona is entirely due to the Thomson scattering of photospheric radiation (Van de Hulst 1953). Typical densities are about 10^8 cm^{-3} in the inner corona and it may vary by one to two orders of magnitude in different coronal regions. Newkirk(1967) has summarized the electron density measurements.

Table 1.1: Properties of different kinds of coronal loops (Priest 1984)

Property	Inter-connecting	Quiet-region	Active-region	Post-flare	Simple-flare
length(1000km)	20–700	20–700	10–100	10–100	5–50
temperature(K)	2–3×10^6	1.8×10^6	10^4–2.5×10^6	10^4–4×10^6	$\leq4\times10^7$
density(cm^{-3})	7×10^8	0.2–1.0×10^9	0.5–5.0×10^9	10^{11}	$\leq\times10^{12}$

1.3   Coronal Structure

The different regions in the Sun as well as the basic properties are shown in Figure 1.1. The visible solar atmosphere is traditionally divided into three regions. The lowest is the photosphere which emits most of the solar radiation. Above the photosphere lies the rarer and more transparent chromosphere. Solar corona is the tenuous outer envelope of the Sun. High resolution pictures of solar corona show a highly inhomogeneous corona which changes very much with the phase of sunspot cycle. An important question in this regard is that are these atmospheric inhomogeneities merely an intrusion into an otherwise uniform media or are they the real building blocks of corona (Alfvén 1963). It is found that active as well as quiet regions are filled with loop-like structures of varying size; they may be classified as in Table 1.1 (Priest 1984). Under these circumstances, a plane parallel division of solar atmosphere into different regions, may not be always useful. A physically more significant definition of corona would be, simply, the ensemble of all features that radiate predominantly in the x-ray regime and thus consisting of plasmas with effective temperatures in excess of 10^6 K (Vaiana & Rosner 1978). The chemical composition of solar corona

CORONA

CHROMOSPHERE

PHOTOSPHERE

CONVECTION
ZONE

2.5 Mm

1 Ro

0.5 Mm

RADIATIVE
ZONE

0.86 Ro

$T = 1.5 \times 10^7$ |
$\rho = 1.6 \times 10^5$ |

0.25 Ro

Energy Generated   CORE

8×10^6

Radiative Diffusion

5×10^5

4300

Radiation

Convection

6600

10^6 T

Waves

8×10^{-3}

Solar Wind

10^{-11}

ρ
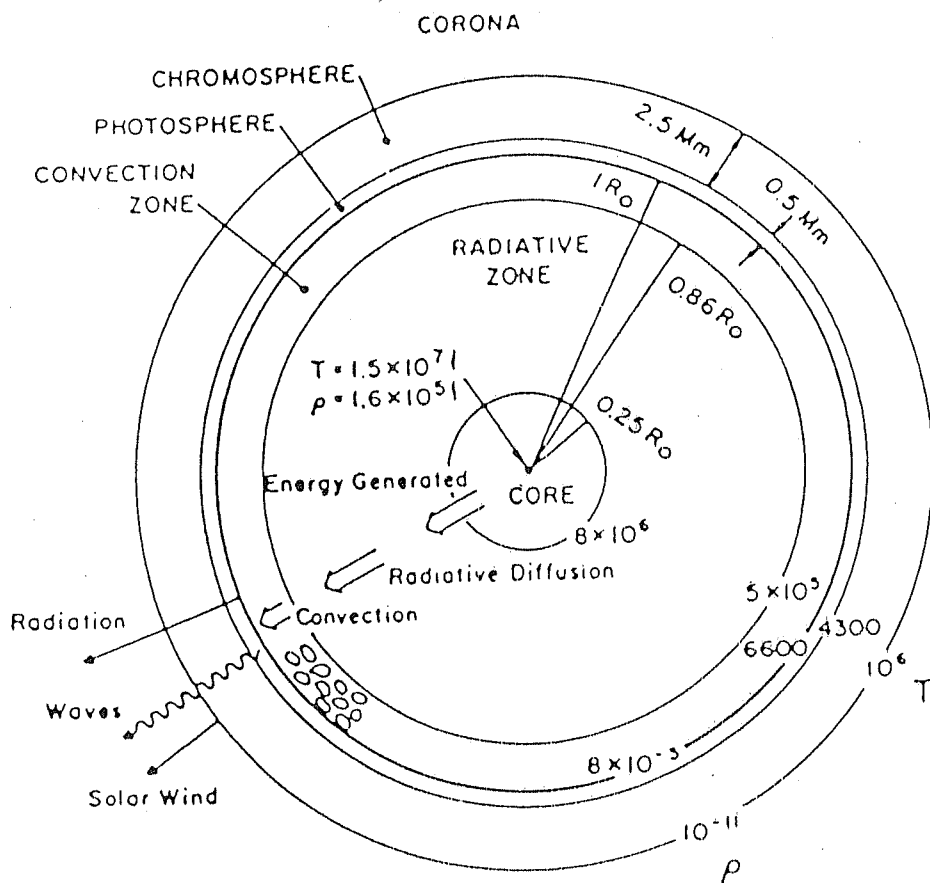
Fig. 1.1   The overall structure of the Sun (Priest 1984).

is almost similar to that of photosphere; 90 % is H, about 9.99 % He, and the rest is other elements such as C, O, Si, Mg, N, Ne, Fe etc. The abundance of Mg, Al, and Si in corona is larger by a factor of three than that of photosphere while it is larger by a factor of ten for Fe (Goldberg 1967). Because of the high temperature, all elements exist in ionized form in the corona. Presence of strong magnetic fields makes it in the realm of magnetohydrodynamics (MHD), where a complex interaction of plasma and magnetic field takes place. Throughout the corona the plasma beta—the ratio of material pressure to magnetic pressure—is less than one, and hence the magnetic field dominates the plasma. Various features we see in a coronal picture such as loops, streamers etc thus reveal the underlying magnetic field.

1.4   Coronal Temperature

The temperature in different regions of the Sun is mentioned in Figure 1.1. The temperature is about 6000 K in the photosphere and then it increases slowly to about 10^4 in the chromosphere. In the chromosphere-corona transition region, the temperature increases by two orders of magnitude and then attains a maximum value of about two million K, somewhere in the corona. Thereafter it falls steadily to about 10^5 K at 1 AU. Coronal temperature shows large variations in different coronal regions. In quiet coronal regions it is about 1.1–1.6 million K, in coronal holes it is 1 million K, and in active coronal regions it may go upto 2.5 million K or even more. The high temperature of the corona remains as one of the most intriguing problems of solar physics ever since its discovery in the early fourties.

There are basically four methods of determining the coronal temperature (Billings 1966)

i) Temperature by degree of ionization

ii) Temperature from electron density distribution

iii) Temperature from radio measurements

iv) Temperature from emission line profiles

For a non-equilibrium, non-uniform medium like corona the kinetic temperature from line width can be obtained by equating the momentum transferred per unit time to a surface of unit area normal to the line of sight $(N_i m_i \bar{v}_{x,i}^2)$ to the partial pressure of the species $(N_i k T)$. Thus

$$T = \frac{m_i \bar{v}_{x,i}^2}{k} = \frac{m_i c^2}{k} \left(\frac{\Delta \lambda}{\lambda} \right)^2 \tag{1.1}$$

where $\Delta \lambda$ is the Doppler shift measured from the mean position. $\bar{v}_{x,i}$ is the average thermal velocity of the species along the line of sight. N_i is the number density and m_i is the mass of the emitting species.

If the velocity distribution of coronal ions is given by Maxwell-Boltzmann distribution, the line intensity, then, is given by

$$I(\lambda) = I(\lambda_0) \exp \left[-\frac{mc^2}{2kT_D} \left(\frac{\lambda - \lambda_0}{\lambda_0} \right)^2 \right] \tag{1.2}$$

where λ_0 is the rest wavelength, T_D the line width Doppler temperature and m is the mass of the emitting ion.

Defining the full width at half maximum (FWHM, $\Delta \lambda_D$) as $2(\lambda - \lambda_0)$ when $I(\lambda) = \frac{I(\lambda_0)}{2}$

$$T_D = \frac{mc^2}{8k \log_e 2} \left(\frac{\Delta \lambda_D}{\lambda_0} \right)^2 \tag{1.3}$$

By measuring $\Delta\lambda_D$ of the line profile, one can readily calculate T_D. However there is some uncertainty in attributing the line width completely to temperature, since broadening may result due to the presence of microturbulence in the medium which may be expressed as

$$\frac{2kT_0}{M} = \frac{2kT_D}{M} + v_t{}^2 \tag{1.4}$$

where T_0 is the observed line width temperature and v_t is the nonthermal velocity characterizing microturbulence.

Microturbulence is generally present in coronal line profiles. The estimated nonthermal motion in corona typically ranges from 10–30 $km\,s^{-1}$ and is often comparable to the thermal widths itself. In addition to this, presence of discrete moving components such as coronal loops may also produce significant deviation of the line profile from Gaussian nature, especially in coronal active regions.

The use of emission line profiles is one of the oldest methods for the determination of coronal temperature. Bernard Lyot (Lyot 1937), using a high dispersion spectrograph, measured the width of the green coronal line to be 0.90 Å which later led to the discovery of a million degree corona. During the later years, the method has been widely used by many authors (Waldmeier 1945, Dollfus 1953, Pecker et al., 1954, Billings 1957, Zirin 1959, Billings 1966).

1.5   Coronal Velocity Fields

The expansion of coronal gas into interplanetary medium implies that corona is a steady-state dynamic medium rather than a static one. Calculations by Ness et al., (1963) indicate that the lower corona need to be replaced about once in a day (cf

Newkirk 1967). The inhomogeneous nature of corona with a multitude of loop-like structures was realized in recent years. Theoretical studies show that the likelihood of this loops being in a static equilibrium is very small.

Traditionally, velocity fields are studied by ground-based eclipse observations. Coronagraph observations are made on a day-to-day basis from different coronagraph stations. Rocket and spacecraft-borne observations are increasingly being used in uv and x-ray wavelengths. Techniques such as eclipse photography, multislit grating spectroscopy and Fabry-Pérot interferometry have been extensively used. In the past two decades, spacecraft measurements of Orbiting Solar Observatory (OSO), Skylab and NRL's High Resolution Telescope and Spectrometer (HRTS) have added a wealth of information in this field. Velocity Information is deduced from the intensity fluctuations of spectral lines presumably arising from the wave motions in the medium, the Doppler halfwidths of emission lines which give a measure of nonthermal mass motions and from the Doppler shifts in the emission line peaks which gives the gross motions existing in the medium (Billings 1966).

Bugoslavskaya (1949) using eclipse photographs, studied macroscopic mass motions and inferred velocities ranging from 0.6-47 $km\,s^{-1}$ in various coronal structures. Waldmeier (1947) and Dollfus (1957) found that velocities seldom exceed a few $km\,s^{-1}$, except over active regions; however, velocities of the order 150 $km\,s^{-1}$ were seen by them, associated with hot condensations in green line. The first successful Fabry-Pérot Interfermetric observation was made by Jarret and von Klüber (1955) at the total solar eclipse of June 30, 1954. Presence of transverse hydromagnetic waves in corona was inferred by Billings (1959) from an observed quasiperiodic variation of green line intensity. Lilliequist (1966) and Noxon (1966) noticed periodic fluctuations in the green line intensity. Delone and Makarova (1969) from their line profile studies

of red and green line, observed during the total solar eclipse of 30 May 1965, found significant Doppler velocities in the range 10–40 $km\,s^{-1}$. In some active regions velocities upto 70 $km\,s^{-1}$ were also seen. However, Liebenberg et al., (1975) found the Doppler velocities in the green line to be less than 5 $km\,s^{-1}$ from the same eclipse observations. The time sequence of green line profiles showed intensity and line width variations at two locations(Liebenberg et al., 1975). Delone and Makarova (1975) from their interferometric observation of coronal green line during the total solar eclipse of 11 September 1968 found evidence for the existence of about 85 % of moving elements in the corona. Out of the 913 line profiles from 1.02-1.39 $R_\odot$, about 10% showed radial velocities greater than 100 $km\,s^{-1}$. Hirschberg et al., (1971) reported a complex vortex structure associated with a streamer inwhich a relatively cool system revolved about a hot core; the observed velocities are of the order 6 $km\,s^{-1}$ in the green line.

On 11 September 1973, a prominence was observed which displayed velocities upto 50 $km\,s^{-1}$ both toward and away from the observer. This was interpreted as the downflowing material lifted into the corona during an earlier transient (Hildner & Livingstone 1975). Line profile analysis of a quiet prominence showed that most of the coronal material flowed from west to east with velocities upto 12 $km\,s^{-1}$ (Tsubaki 1975). Kim and Nikolsky (1975) reported an increase of halfwidth of the coronal green line with distance from the solar center, from 1.2-1.7 $R_\odot$. The increase would correspond to an increase of nonthermal velocity with a gradient of 1–2 $km\,s^{-1}$ per 0.1 $R_\odot$. No line of sight velocities greater than 10 $km\,s^{-1}$ were found. Line profile analysis of an active region in the coronal green line showed considerable variation in intensity with accompanying changes in temperature but the velocity field was found to be stable as far as the magnetic field configuration remained the same. A general flow superposed on a local velocity field from east to west was also inferred (Tsubaki

1983).

Rocket-borne spectrograph measurements on coronal ions such as SiX (303 Å), MgX (610 Å), MgIX (368 Å) showed evidence for outward flow of plasma with velocities $\sim$16 $km\,s^{-1}$. The line centers in the coronal hole regions were found to be systematically shifted to the shorter wavelength side of the line center (Kushman & Pense 1976). Mass motions in the chromosphere-corona transition region were observed at uv wavelengths in ions such as CIV and SiIV. Typical downflow velocities were found to be $\sim$20 $km\,s^{-1}$ (Athay et al., 1980, Brueckner 1980, Poletto 1981). The width of EUV spectral lines from the transition region showed evidence for nonthermal mass motions in the range 10–25 $km\,s^{-1}$ (Doschek et al.,1981). Mass motions with velocities upto 100 $km\,s^{-1}$ were also reported (Doschek & Feldman 1977). Line profile analysis of CIV 1548 Å in active and quiet transition regions showed a tendency for the line width to increase with increasing red shift (Athay et al., 1983a). Ulmschneider (1976) found that five minute oscillation is not a significant energy source for chromosphere and corona, from the analysis of EUV and radio emission spectra. The large scale flow observed in the transition region was found to be consistent with loop systems with downflow in both the legs. An important subset of loops showed flow velocity from one foot point to the other (Athay et al., 1983b). Mein et al., (1982) found that downflow velocities are well correlated in H_α and CIV observations of active regions. Observations carried out by SMM, UVSP simultaneous spectrogram and Dopplergram in CIV gave detailed information on the velocity and emission measure of individual loops. The results were compared with the theoretical profiles for loops with i) a steady-state model with a siphon flow, ii) a steady-state flow with downflows in both the legs which is maintained by continual mass addition at the loop summit and iii) a non-steady loop model with downflow where the initial plasma density decays with time. It is found that none of the above simple flows

12

could explain the observed features completely. Observation also revealed two classes of loops; hot loops ($T > 10^6$ K) having longer life times for which hydrostatic equilibrium apparently prevails and cool loops (T$< 10^6$ K) characterized by large scale flow (Kopp et al., 1985).

Many coronal transient events have been observed in recent years. Prominent among them are the Coronal Mass Ejection (CME) events. CME is the sudden expulsion of dense plasma clouds from the atmosphere of the Sun with an average speed of 400 km s^{-1}. Flares, eruptive prominence and non-equilibrium magnetic field configurations are some of the postulated origins of CME. CMEs generally appear as loops and loop-like clouds. Temperature of the CMEs were found to be that of corona (Wagner 1984). Observation of the uv solar spectrum from NRL's HRTS revealed many high energy events in quiet Sun. They were broadly divided into turbulent jets which is confined to smaller areas ($< 2''$) with velocities $\sim$250 km s^{-1} and jets with velocities $\sim$400 km s^{-1} .

Theoretical developments in the coronal science and breakthroughs in space-borne measurements of corona, resulted in a renewed interest in the ground based eclipse observation in eighties. FP interferometric observations in the green line during the total solar eclipse of February 1980 indicated large scale mass motions in the solar maximum corona. Line splitting was observed in active western limb (Chandrasekhar 1982, Desai et al., 1982). Harvey and Livingstone (1981) reported inflow velocities in the range 3–15 km s^{-1} in 30 % of their samples from their observation of the same eclipse with a multislit dispersion spectrograph. Singh et al., (1982) from their red line observations, obtained line of sight velocities between 14 km s^{-1} and -17 km s^{-1} with most of the locations having velocities $< \pm 5$ km s^{-1} . Delone et al., (1988) finds evidence of moving components in corona from their analysis of green

and red line profiles belonging to five total solar eclipses. Pasachoff and Landman (1984) reported high frequency oscillations (0.1–2 Hz) in the intensity of the green line. This is ascribed to the presence of Alfvén or fast MHD waves trapped in coronal loops. The radial velocities in the inner corona during total solar eclipse of 31 July 1981 were found to be 2–3 $km\,s^{-1}$ with extremes -6.6 and 12.6 $km\,s^{-1}$ (Rybansky et al., 1986). Fabry-Pérot observation of corona during the total solar eclipse of 11 June 1983 in Indonesia in the dual channel of green and red line by Chandrasekhar et al., (1991) resulted in, obtaining many good line profiles. They find signatures of discrete plasma motion in the line profiles.

1.6   Coronal Emission

1.6.1   Coronal Ionization

The average thermal energy in the corona is $3/2\ kT \sim 260$ eV at 2×10^6 K whereas the ionization energies of coronal elements vary from 5 to 10^3 eV. The ionization energies for HI and HeII are 13.6 and 54.5 eV respectively and they are almost completely ionized in the corona. Ionization and recombination balance for the corona is shown in the Figure 1.2. In Thermodynamic Equilibrium (TE), ionization by electron impact is balanced by three-body recombination and photoionization is balanced by photorecombination. In the corona, however, owing to low particle and radiation densities, ionization by electron impact is balanced by photorecombination. Dielectronic recombination, in which a recombining electron imparts its kinetic energy to excite a bound electron to an excited state while itself getting recombined to an excited level, is found to be more important at coronal temperatures (Jordan 1969). The degree of

14

Table 1.2: Catalogue of eclipse studies with Fabry-Pérot and Multislit observations (Delone et al., 1988)

Eclipse	Authors	Method	Spatial Resolution (arc sec)^2
21 Sept 1941	Kalinijak (1949)	FP	Unknown
30 July 1954	Jarret & Klüber (1955)	FP	Unknown
12 Oct 1958	Jarret & Klüber (1961)	FP	Unknown
30 May 1965	Delone & Makarova (1969)	FP	3×12
	Liebenberg et al., (1975)	FP	1380
12 Nov 1966	Liebenberg et al., (1975)	FP	Unknown
22 Sept 1968	Delone & Makarova (1975)	FP	3×12
7 Mar 1970	Delone & Makarova (1973)	FP	$c \times 3$
	Hirschberg et al., (1971)	FP	Unknown
	Marshall & Henderson (1973)	FP	$0.1 R_{\odot}$
	Livingstone et al., (1970)	MS	100
10 July 1972	Kim & Nikolsky (1975)	FP	190
	Delone & Makarova (1973)	FP	10
30 June 1973	Bessey & Liebenberg (1984)	FP	–
11 Feb 1980	Chandrasekhar et al., (1981)	FP	80
	Desai et al., (1982)	FP	80
	Livingstone & Harvey (1982)	MS	70
	Singh et al., (1982)	MS	220
	Singh (1984)	MS	220
	Singh (1985)	MS	220
	Bhatnagar et al., (1982)	MS	Unknown
31 July 1981	Ushakov et al., (1984)	FS	10
	Yaroslavisky et al., (1984)	FS	10
11 June 1983	Singh (1984)	MS	220
	Chandrasekhar et al., (1984)	FP	80
	Chandrasekhar et al., (1991)	FP	80

Ionization by
electron impact
$(\sim N_e N_{ion})$

TE

Three-body
recombination
$(N_e^2 N_{ion}^{+1})$

Coronal non-LTE

Photoionization
$(\sim I_\lambda N_{ion})$

TE

Photo recombination
$(\sim N_e N_{ion}^{+1})$
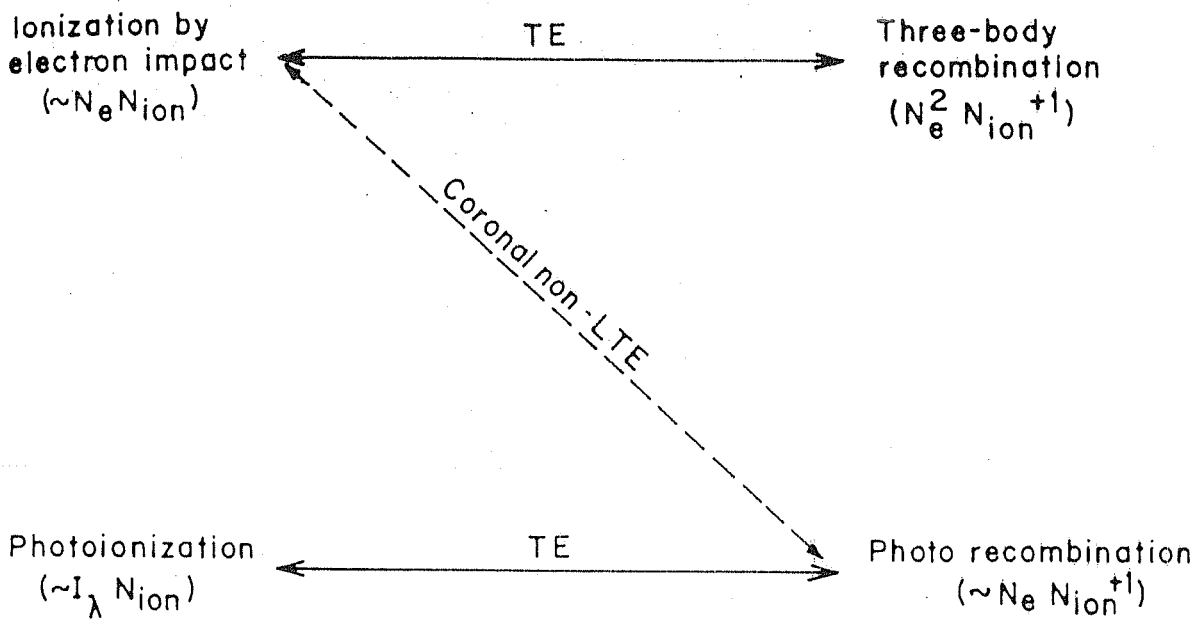
Fig. 1.2   Ionization and recombination balance in the corona (Gibson 1973).

State 2 ————————————————————————————

$N_1 R_{12}$
(radiation)

$N_e N_1 C_{12}$
(collision)

$N_2 A_{21}$
(radiation)

$N_e N_2 C_{21}$
(collision)

State 1 ————————————————————————————
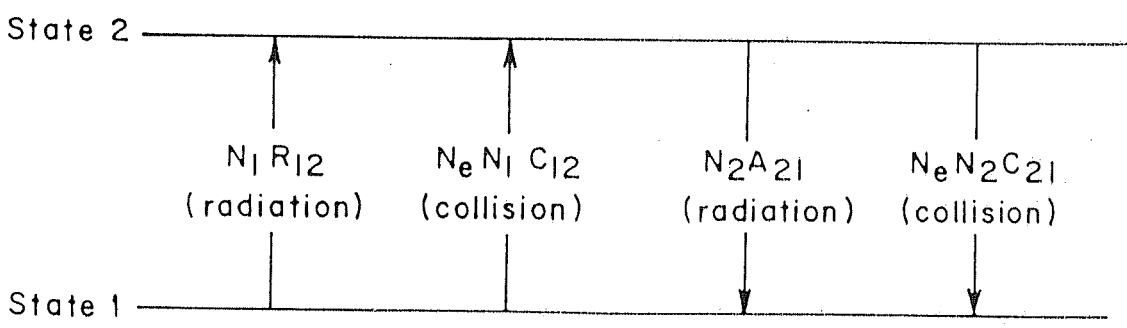
Fig. 1.3   Radiation   and   collisional   balance   between   two   energy levels in the corona (Gibson 1973).

ionization of an element is calculated by equating the ionization and recombination rates that relate successive stages of ionization.

$$n_e N_i C_{1\infty} = n_e N_{i+1} A_{\infty 1} \qquad (1.5)$$

$$\frac{N_{s+1}}{N_s} = \frac{C_{1\infty}}{A_{\infty 1}} \qquad (1.6)$$

where N_i is the number density of atoms in the i'th stage of ionization, $C_{1\infty}$ is the rate coefficient for transition from the ground level 1 to the excited level (∞) by electron impact, $A_{\infty 1}$ is the recombination which includes not only the straight transition from ionized to the ground level but also the cascading down through the possible levels of excitation. The overpopulation of ground states in coronal condition makes this contribution negligible.

1.6.2   Coronal Excitation

The emission from the corona arises under highly Non Local Thermodynamic Equilibrium (NLTE) conditions and hence the interpretation of the spectra is fairly complex. The Corona is composed of low density, high kinetic temperature particles immersed in the low temperature radiation field of the photosphere (Gibson 1973). To determine the strength of the emission line from an excited level, the rates of production and removal of a level are equated (Figure 1.3). R_{12} is the radiative excitation rate, $n_e C_{12}$ is the collisional transition rate, A_{21} spontaneous transition probability and $n_e C_{21}$ is the rate of downward collisional transition. In this balance, we have neglected the population of level 2 by transition from above. For conditions prevailing in corona, the radiation intensity is low enough such that $R_{12} \ll n_e C_{12}$ and the gas density is low enough so that $n_e C_{21} \ll A_{21}$. Hence

$$n_e N_1 C_{12} \simeq N_2 A_{21} \qquad (1.7)$$

17

Since the number density in N_1 is proportional to the total gas density which itself is proportional to n_e, the rate of spontaneous emission is proportional to n_e^2. Moving outward in the corona, a point is reached at which $n_e C_{12} \ll R_{12}$. Thus

$$N_1 R_{12} \simeq N_2 A_{21} \tag{1.8}$$

and the emission will vary as n_e/r^2 which is similar to the variation of K-corona.

The prominent optical and near infrared lines may be classified into three groups according to their relation to solar activity (Gibson 1973). This is shown in Table 1.3. The lines often used to represent three groups are the red line of FeX, green line of FeXIV and yellow line of CaXV. All the lines except FeXV 7059 Å , arise due to the forbidden transition between split terms in the ground state. The intensity of a coronal line is usually expressed in units of millionth of the intensity of the center of the photosphere disk in a 1Å bandwidth centered on the line.

$$1B_\odot = 3.8 \times 10^6 \, \text{erg} \, \text{cm}^{-2} \, \text{sr}^{-1} \, \text{sec}^{-1} \, \text{Å}^{-1} \tag{1.9}$$

The intensity of the green line can go upto 200 units while that of red line can be upto 60 units (Dollfus 1971).

1.6.3   Coronal Green Line

Young and Harkness independently discovered the coronal green line during the eclipse of 1869. The spectral identification came only much later—in 1942. The green coronal line is often, the strongest line in the visible spectrum and accordingly, the most observed. The behavior of the line is quite similar to the white light corona, probably because the ionization temperature of the line matches well with the average temperature of the corona (Koutchmy 1988). Characteristics of green line are given

Table 1.3: Classification of prominent visible and infrared lines according to their relation to solar activity (Gibson 1973)

Group	Characteristic	Wavelength, Å	Ion	Ionization Potential, eV
I	Prominent during solar minimum and in quiet regions	3583	V X	206
		3987	Fe XI	262
		6374(red line)	Fe X	235
		7892	Fe XI	262
II	Prominent during solar maximum and in active regions	3388	Fe XIII	330
		3643	Ni XIII	350
		4232	Ni XII	321
		5303(green line)	Fe XIV	355
		7060	Fe XV	390
		8024	Ni XV	430
		10747	Fe XIII	330
		10798	Fe XIII	330
III	Prominent in regions of very high excitation	3327	Ca XII	592
		3601	Ni XVI	455
		4086	Ca XIII	655
		4351	Co XV	412
		4412	A XIV	687
		5446	Ca XV	820
		5694(yellow line)	Ca XV	820
		6740	K XIV	717

below.

Rest wavelength	: 5302.86 Å
Ion	: FeXIV
Ionization Potential	: 355 eV
Temperature at which the ion density becomes maximum	: 1.8×10^6 K (Jordan 1969)
Excitation potential	: 2.34 eV
Transition	: 3p; $^2P_{3/2}$---$^2P_{1/2}$
Spontaneous transition probability	: $60\,sec^{-1}$

The activity of the northern hemisphere is found to be greater than that of southern hemisphere, in recent solar cycles. The asymmetry is very well seen in green line images as well as in x-ray and uv pictures (Gibson 1973). The N-S asymmetry is found to be negatively correlated with the solar activity cycle (Pathak 1972). In some years, however, a reverse of the above phenomena ie a more active southern hemisphere is, also seen. It is found that the maximum asymmetry occurs in the heliographic latitudes $\pm(10-20)°$. Significant W-E asymmetry is observed, sometimes. Physical mechanism of the N-S asymmetry may be due to the different starting time of the 11 year solar cycle in the two hemispheres. However, the physical mechanism of W-E asymmetry is not known (Petropoulos 1988). Some authors have reported the existence of a secondary maximum in solar activity cycle associated with the green line intensities, which were found to be correlated with the sunspot numbers (Gnevyshev

1967, Cuperman & Sternliab 1972, Pathak 1972).

Green line observations were widely used to derive the physical conditions in the corona. Coronal electron density distribution and emission measure can be deduced from such measurements. Presence of coronal holes and depletions were found from such measurements (Fisher & Musman 1975, Fisher 1978).

Excitation Mechanism of Green Line

There exists a minor controversy of the relative roles of collisional and radiative mechanisms in the excitation of the green line. Though the exact contribution can only be calculated from a detailed knowledge of electron density distribution and temperature variations throughout the corona, deductions may be made from the line and continuum intensity measurements. The relation between the intensity of coronal lines to that of continuum was studied for the first time by Grotrian (1933). Intensities of 11 coronal lines were measured upto 6′ from the solar limb and it was found that the line intensity is proportional to the continuum intensity. Waldmeier(1942) concluded that variation of the line intensity is much stronger than that of continuum and it depends upon the local structure of the corona. The line to continuum intensity was again studied by the same author during the eclipse of March 7, 1970 (Waldmeier 1975). It was found that for distances greater than 1.8 $R_\odot$, the ratio of line to continuum intensity becomes a constant which is the indication of dominant radiative excitation. Towards smaller distances, collisional excitation becomes progressively important and at a distance 1.3 $R_\odot$ from the solar centre both the contributions become equal. Excitation mechanism of the line was later studied by many authors (Singh 1985, Raju & Singh 1987, Raju et al., 1991). Raju and Singh (1987) found that excitation mechanism is mainly collisional in the inner regions ($\sim 1.3 R_\odot$) and

21

radiative mechanism become important afterwards. Zirin(1988) finds that excitation mechanism is mainly radiative unless the electron density is more than $10^9 \ cm^{-3}$. Raju et al., (1991) studied the excitation mechanism in different position angles and found that collisional mechanism is generally more important than radiative excitation upto about 1.4 $R_\odot$.

1.7 Coronal Magnetic Fields

In 1908, G.E.Hale discovered solar magnetic fields from the observation of Zeeman splitting in spectral lines in sunspots. The importance of the magnetic field was, however, realized only in the recent past. Magnetic fields affect the coronal plasma in three ways (Priest 1984).

i) It exerts a force $\vec{j} \times \vec{B}$ which is able to act inward and so contain the plasma with an enhanced pressure. This explains the existence of coronal bright points, and loops.

ii) It stores magnetic energy ($B^2/8\pi$) and hence provides a source of heating either by wave dissipation or through ohmic dissipation.

iii) It channels the heat flow along the field. The coefficient of thermal conductivity $k_\parallel$ along the field is larger than that perpendicular to the field ($k_\perp$), and hence the magnetic field force the heat to flow along the field. Thus the temperature and density are strongly affected by the field lines.

It seems that without a magnetic field, the Sun would possess a chromosphere possibly heated by sound waves, but very little corona. The presence of convection in a star

is only a necessary but not a sufficient condition, for the existence of a strong corona (Rosner et al., 1978, Roberts 1987).

Babcock and Babcock invented the magnetograph in 1952 which gives directly the magnetic field by measuring the polarization. This was an impetus to the coronal field measurements. Topologically two types of magnetic field regions are seen in the corona; open field regions such as coronal holes where field lines are predominantly open and closed magnetic field regions such as coronal loops where field lines are predominantly bipolar. Strength of the fields are $\sim$10 G in open field regions while it is $\sim$100 G in closed regions. Sources of coronal magnetic fields are the following.

i) In-situ measurements

ii) Zeeman splitting in active region prominence

iii) Extrapolation from photospheric magnetic field

iv) Radio burst measurements

In-situ measurements have not been made closer than 0.3 AU. Coronal magnetic fields are difficult to measure from the spectral lines because of the faintness of the lines. Nevertheless, attempts have been made to measure the Zeeman splitting of the green line. The results are not conclusive mainly because of the line of sight averaging of regions with opposite polarity (Dulk & Mclean 1978). However, solar prominence fields are measured from Zeeman line splitting. A method of extrapolating the coronal fields from the observed photospheric fields was developed in sixties (Schmidt 1964, Altschuler & Newkirk 1969). In this method the field is assumed to be current-free. The photospheric field is written as a polynomial and the coefficients of the terms of the polynomial are computed by statistical analysis. Once the coefficients are determined, the magnetic field anywhere above the photosphere

can be calculated. This method is currently the best source of information on coronal magnetic fields in the range 1.1–1.4 $R_\odot$, with the introduction of high resolution magnetographs and improved methods of computation (Adams & Pnuemann 1976).

1.7.1 Solar Dynamo

Solar magnetic fields are believed to be caused by a solar dynamo operating in the unobservable depths of the convection zone. The classical diffusion time of solar magnetic fields ($R_\odot^2/\eta$, where η is the magnetic diffusivity) is calculated to be 10^{10} years which is well correlated with the age of the Sun. However, in the presence of resistive instabilities and magnetic buoyancy, the magnetic diffusivity will be very high and it turns out that the magnetic flux will be destroyed within a time scale of 10 years. Hence a dynamo which constantly produces magnetic fields seems to be necessary for the maintenance of the field (Priest 1984).

The various steps in the working of a proposed solar dynamo are the following. A motion $\vec{v}$ across a magnetic field ($\vec{B}$), leads to an induced electric field ($\vec{v} \times \vec{B}$) which drives an electric current by Ohm's law; $\vec{j} = \sigma\,(\vec{E} + \vec{v} \times \vec{B})$ and gives the magnetic field from Ampere's law ($\vec{j} = \vec{\nabla} \times \vec{B}/\mu$). The magnetic field then creates an electric field through Faraday's law $\vec{\nabla} \times \vec{E} = -\frac{\partial \vec{B}}{\partial t}$ and also a Lorentz force ($\vec{j} \times \vec{B}$) which can oppose the force that drives the motion. The whole process involves the solution of the induction equation

$$\frac{\partial \vec{B}}{\partial t} = \vec{\nabla} \times (\vec{v} \times \vec{B}) + \eta \vec{\nabla}^2 \vec{B} \qquad (1.10)$$

and an equation of motion.

Cowling's theorem states that a steady axisymmetric field cannot be maintained. Parker pointed out that anticyclonic motion of rising blobs of plasma in the

24

convection zone produces departures from axisymmetry and may maintain the magnetic field (Parker 1955). Details of the dynamo theory are currently under active investigation.

1.8 Coronal Heating Mechanisms

Coronal heating mechanisms have been a topic of active research during the past fifty years, after the general acceptance of the existence of a million degree corona. Early theories were based on the dissipation of acoustic or weak shock waves generated by photospheric granulation (Bierman 1946,1948, Schwarzchild 1948, Schatzman 1949). However, the realization that the active region corona needs to be heated by one to two orders of magnitude more than quiet regions and because of the strong magnetic nature of the corona, it became apparent that the magnetic field must play an important role in coronal heating. The discovery of the solar wind, a phenomenon which is a direct consequence of the high temperature corona, also supported this view; the existence of solar wind implies an extended heating to far out from the Sun and it seemed unlikely that shock waves reach that far.

In general, one may distinguish two different types of atmospheric heating as applicable to the corona (Kuperus et al., 1981).

1. Heating by acoustic processes in the non-magnetic parts of the atmosphere such as the photosphere and the lower chromosphere where $\beta = 8\pi p/B^2 \geq 1$

2. Heating by electrodynamic processes in the magnetic regions where $\beta \ll 1$, either by MHD waves or by current heating.

Energy Requirements:

At each location in solar atmosphere, a thermal equilibrium in the form

$$C = H - R \qquad (1.11)$$

has been assumed (McWhirter et al., 1975). H is the heating term, $(-R)$ is the radiative loss and C is the conductive loss.

$$C = \vec{\nabla}.\vec{F_c} \qquad (1.12)$$

where $\vec{F_c}$ is the conductive flux given by

$$\vec{F_c} = -\kappa_0 \, T^{5/2} \, \vec{\nabla} T \qquad (1.13)$$

where κ_0 is the thermal conductivity.
Radiative loss may be given by

$$R = n_e \, N_H \, Q(T) \qquad (1.14)$$

$$Q(T) = \chi \, T^\alpha \, W \, m^{-3} \qquad (1.15)$$

Q(T) is given by McWhirter et al., (1975), α and χ are the radiative loss coefficients which are functions of temperature and is tabulated by Rosner et al., (1978). The energy loss in coronal holes include the loss due to the solar wind which amounts to $5 \times 10^5 \, erg \, cm^{-2} \, sec^{-1}$. The convection zone appears to be the energy source which maintains the corona through its turbulent granular motion (Roberts 1987).

The total heat content of the corona is $\sim$

temperature scale height$\times$ enthalpy density $(5 n_e k T)$

$$\sim 10^{11} erg \, cm^{-2}$$

26

Table 1.4: Energy Losses from Corona and chromosphere (Withbroe & Noyes 1977)

Energy loss $(erg\ cm^{-2} sec^{-1})$	Quiet Sun	Coronal hole	Active region
Corona	3×10^5	8×10^5	10^7
Chromosphere	4×10^6	4×10^6	2×10^7

The characteristic thermal time is $\sim 10^{11}\ erg\ cm^{-2}/10^7\ erg\ cm^{-2}\ s^{-1}$

This implies that if the heat source is shut off, the corona and the solar wind would collapse within a few hours (Parker 1986).

1.8.1 Acoustic Heating

The Turbulent convection zone produces low amplitude acoustic waves by its convective motions. The waves when they propagate through the stratified solar atmosphere, produce shocks and the resultant dissipation may, it is believed, heat the chromosphere and corona. In a stratified atmosphere where the density variation is given by

$$\rho \sim e^{-z/\Lambda} \qquad (1.16)$$

where z is the coronal height and Λ is the scale length. The damping time which is the distance the wave travels before shocking is given by

$$d = 2\Lambda \log \left(1 + \frac{\tau C_s^2}{2(\gamma + 1)\Lambda v_1} \right) \qquad (1.17)$$

where τ is the wave period, C_s is the sound velocity, and γ is the adiabatic index.

For $\gamma=5/3$, $C_s=6$ km s^{-1}, $\Lambda=130$ km, $v_1=0.6$ km s^{-1}, at the base of the chromosphere,

$$d \quad = 500 \text{ km for } \tau=10\text{s}$$

$$= 800 \text{ km for } \tau=30\text{s}$$

which implies that short period waves can heat only the low chromosphere. OSO 8 measurements show that 300 s waves have insufficient energy flux ($\sim 10^4$ $erg\ cm^{-2}\ s^{-1}$ in the chromosphere and it decreases with height) to heat upper chromosphere and corona (Athay & White 1978, Mein & Mein 1980).

1.8.2   Electrodynamic Heating

Generation of electrodynamic heating occurs when plasma is forced to flow across the field lines ie they arise from the $(\vec{v} \times \vec{B})$ terms in the Ohm's law. Electrons and ions move differently under the influence of the magnetic field create local charge separation and thus produce electric currents. The currents in turn modify the ambient magnetic field. Generation of electrodynamic energy is governed by the Poynting's theorem.

$$\vec{j}.\vec{E} = -\frac{c}{4\pi}\vec{\nabla}.(\vec{E} \times \vec{B}) - \frac{1}{8\pi}\frac{\partial B^2}{\partial t} \tag{1.18}$$

The first term on the right hand side gives the divergence of Pointing flux which represents the coupling between the region of electrodynamic energy generation (photospheric driver) and the external region (corona) while the second term gives the storage of magnetic energy.

The energy generated will be dissipated as

$$\vec{j}.\vec{E} = \eta_{\perp electric}\, j_\perp^2 + \eta_{\parallel electric}\, j_\parallel^2 + \eta_{mech}\, j_\perp^2 \qquad (1.19)$$

The first term on the right hand side represents electron joule heating by cross-field currents while the second term gives the dissipation of field aligned currents. The third term represents viscous and mechanical heating (Kuperus et al., 1981).

Electrodynamic heating may be of two types; by MHD waves and by current heating. The presence of small scales of the order 500m in the magnetic field is essential for both the processes (Roberts 1987, Van Ballegoigen 1988).

MHD Waves

Three distinct MHD wave modes possible in a magnetic field dominated atmosphere are Alfvén, fast and slow waves. The dominant damping mechanism for Alfvén waves is joule dissipation while for fast and slow modes, it is shock dissipation. Osterbrock (1961) proposed that in regions where the magnetic field is less than 100G, waves generated in the turbulent convection zone will be converted mostly into fast modes and to a lesser extent slow and Alfvén modes. Fast mode waves propagate into the corona where they form shocks and dissipate their energy.

Alfvén waves possess an energy flux $2\rho_0 < v^2 > v_A$ where $< v^2 >$ represents the mean square velocity fluctuations and v_A the Alfvénic group velocity.

$$v_A = \frac{B_0}{\sqrt{4\pi\rho_0}} \qquad (1.20)$$

$$= \frac{10^2}{\sqrt{4\pi \times 1.67 \times 10^{-14}}}$$

$$= 2 \times 10^3 \ km\, s^{-1}$$

29

where

$$\rho_0 \approx n_e m_p \tag{1.21}$$

$$= 10^{10} \times 1.67 \times 10^{-24}$$

and hence the energy flux in active regions is $\sim 4 \times 10^7 \, erg \, cm^{-2} \, s^{-1}$. In coronal holes with

$$n_e \sim 10^8 \, cm^{-3}, B = 10 \, G,$$

$$\rho_0 = 1.67 \times 10^{-16} \, g \, cm^{-3}$$

$$v_A = 2 \times 10^3 \, km \, s^{-1}$$

$$energyflux \sim 10^6 \, erg \, cm^{-2} \, s^{-1}$$

Hence Alfvén waves can provide enough energy for the heating.

The damping length of Alfvén waves is given by

$$L_{damp} = \frac{v_A^3 \tau^2}{2\pi^2 \nu} \tag{1.22}$$

where τ is the time scale of photospheric motions$= 10^2 - 10^3 s$
and ν is the kinematic viscosity $\sim 2 \times 10^{15} \, cm^2 \, s^{-1}$

$$L_{damp} = 30 R_\odot$$

which implies that Alfvén waves are difficult to dissipate under coronal conditions.

However, in a nonuniform plasma, scale lengths$\sim 10^3 - 10^4$ km
and the damping length is given by

$$L_{damp}^{nonuniform} = \left(3a^2 L_{damp}\right)^{1/3} \tag{1.23}$$

30

$$= 4 \times 10^4 \, \text{km in coronal holes}$$

$$= 9.4 \times 10^5 \, \text{km in active region}$$

This implies that unless the scale of variation of magnetic field is below 10^3 km, Alfvén waves cannot heat coronal loops though they may heat the coronal holes (Roberts 1987).

Heating by Currents

There are two important mechanisms which may give rise to dissipation of currents in the corona.

1. Joule dissipation which involves no change in magnetic field structure.

2. Magnetic reconnection which involves topological changes in field structure alongwith Joule dissipation and strong convective flux.

Coronal heating by anomalous Joule dissipation as a possible heat source was studied by many authors (Tucker 1973, Rosner et al., 1978, Hinata 1979, 1980). Heating by reconnection was proposed by Levine (1974) in which a large number of $j_\perp$ driven neutral sheets are assumed to exist in the corona; the Joule heating and the particle acceleration, caused by the reconnection processes would then heat the corona. Ionson et al., (1978) put forward a unified approach which incorporates both wave heating as well as current heating. Solar plasma structures are viewed as 'transmission lines' characterized by impedances, Q-values, L/R, RC and LC circuits. The approach has been found successful, in providing the required amount of heating.

31

Parker (1983,1987,1990) has argued that active regions necessarily build up stresses in the magnetic field, as a response to the coronal loop foot point motions in the turbulent zone. These stressed coronal fields undergo reconnection resulting in heating the corona. Parker's estimate of heating is in the required range for active regions.

It appears that different mechanisms are responsible for heating. In active regions the reconnection of stressed fields may account for their observed x-ray intensity whereas in coronal holes, Alfvén waves may provide the required heating. The mechanism of heating of the upper solar atmosphere, however, remains as an open question. It is expected that detailed observational knowledge of the velocity field spectrum and the coronal magnetic field, may resolve the problem in the near future (Kuperus et al., 1981).

1.9   Coronal Modelling

Modelling of the solar atmosphere is done in either of two ways; through the emission measure analysis or through the energy balance modelling (Vaiana & Rosner 1978). The first treatment calculates the differential emission measure $Q(T) = n_e^2 (dT/ds)^{-1}$ along the instrument line of sight and uses this result to deduce the physical parameters characterizing the atmosphere. The second method involves the solution of a local energy balance equation, momentum equation, continuity equation and an equation of state with appropriate boundary conditions. Integration over the model atmosphere yield radiative fluxes which are then compared with the observed values. Parameters are varied to obtain a 'best fit' (Kopp & Orrall 1970, Withbroe and Noyes 1977). It is suggested that the two approaches are complimentary, providing answers

to different questions about the atmosphere (Vaiana & Rosner 1978).

Observations over the past 20 years have lead to a conjecture that loops, being the flux tubes connecting regions of opposite polarity, are the primary units of corona. This has resulted in modelling individual loops, where, they are regarded as plasma volumes relatively isolated by the magnetic field. Each loop is characterized by two coordinates, namely, the displacement along the length of the loop (s) and the radial displacement from the loop axis (r). The equation of motion of the plasma is solved subjected to the boundary conditions imposed at the loop foot points $s = s_0$ and at the loop surface $r = r_0$ with additional constraints of magnetic field (Kopp & Pnueman 1976).

Rosner et al., (1978) obtained some simple scaling laws by considering a closed coronal loop in a hydrostatic equilibrium.

$$T \sim 1.4 \times 10^3 \, (pL)^{1/3} \tag{1.24}$$

$$E_H \sim 10^5 \, p^{7/6} \, L^{-5/6} \tag{1.25}$$

where p is the pressure, L is the length of the loop and E_H is the mechanical heating. The scaling laws are found to agree well with the observations. Also it is suggested that the heating mechanism cannot solely depend upon the local plasma conditions, but must also respond to the loop geometry which is defined by the magnetic field. Thus the model strongly argues for a magnetic field related heating mechanism. Coronal loops with mass flows were modelled in recent years and it has been found that loops which are not in hydrostatic equilibrium may also exist, but are likely to be in a steady-state (Cargill & Priest 1980, Noci 1981 Boris & Mariska 1982). Comparison of the results with the observations have shown that simple flows like a steady siphon flow may not explain all the features and the flow appears to be more complex (Kopp

33

et al., 1985).

1.10 Solar Cycle

The fact that the solar corona changes its shape between the times of sunspot mini-
mum and maximum have been known since 1875. The phase of the solar activity is
denoted by the Wolf number which is given by

$$R = K(10g + f) \qquad (1.26)$$

where K is an observer correction factor (~ 0.6), g is the number of sunspot groups
and f is the number of sunspots counted. Sunspot number for the recent solar cycles
are shown in the Figure 1.4 (Loucif & Koutchmy 1989). In addition to the 11 year
cycle, a superposed 80 year period is also reported. The rise period of the 11 year
cycle is generally found to be less than the decline period. Sunspots erupt at latitudes
about $\pm 40^{o}$ in the beginning of the cycle and gradually drifts to about $\pm 5^{o}$ towards the
beginning of the next cycle which is well depicted in Maunder's butterfly diagrams.
One other important phenomenon associated with the solar cycle is change of polarity
of the global magnetic field at the beginning of every cycle.

Since the solar cycle essentially reflects the behavior of the solar magnetic
field, and the existence of corona itself is a manifestation of the same field, most of
the coronal phenomena are intimately related to the phase of the solar cycle. This
is evident in the behavior of coronal shape, electron density distribution, green line
intensity, x-ray emission, solar wind, N-S asymmetry and coronal rotation rate. It
appears that coronal kinetic temperature also changes with the cycle, but currently
such correlation studies are rarely available. The departure from spherical symmetry

Dates of the Observed Solar Total Eclipses
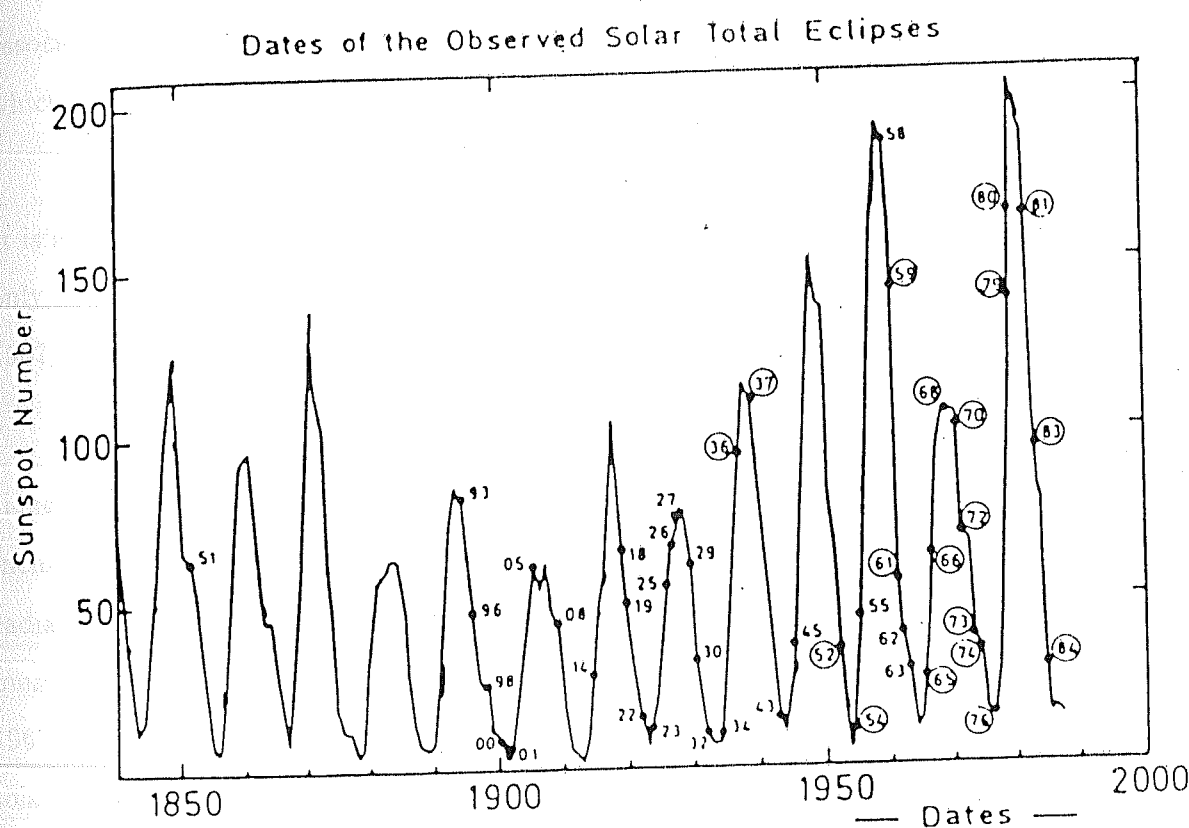
Fig. 1.4 Sunspot number against the year (Loucif & Koutchmy 1989).

associated with the cycle is well illustrated in the definition of the flattening index which is given by

$$\epsilon = \frac{R_{eq}}{R_{pol}} - 1, \text{ for coronal isophotes.} \qquad (1.27)$$

It is found that the difference between sunspot minimum and maximum is in degree only, as in both phases coronal isophotes do not show spherically symmetry (Newkirk 1967). For recent eclipses, values are given by Loucif and Koutchmy (1989).

Some of the other coronal phenomena related with the sunspot cycle are mentioned in the following. At sunspot minimum, coronal streamers are found to be inclined to the radial direction whereas at sunspot maximum they are more or less radial (Waldmeier 1971). Electron densities throughout the corona at sunspot maximum are about twice that of corresponding densities at sunspot minimum (Newkirk 1967). The total intensity of the green line is well correlated with the phase of the solar cycle. At the sunspot maximum total intensity of the green line is about eight times more than that of minimum periods (Waldmeier 1971). The existence of a secondary maximum in the sunspot number was noted by many authors (Gnevyshev 1967, Cuperman & Sternliab 1972, Pathak 1972). X-ray emission is found to be a better indicator of solar activity than longer wavelength electromagnetic waves (Goldberg 1967). The N-S asymmetry seen in the green line intensity and in the number of sunspots, showed a negative correlation with the phase of the solar activity (Pathak 1972, Moussas et al., 1983, Loucif & Koutchmy 1989, Petropoulos 1988). However, Waldmeier found that N-S asymmetry is correlated with a longer cycle of period 80 years (Waldmeier 1971). Antonucci and Svalguard (1974) found that the rotation of coronal features observed in green line with lifetimes of at least one solar rotation depends on solar cycle, outside the equatorial zone. Equatorial rotation rate is nearly constant during the whole period and coincides with the rotation periods of sunspots

(Antonucci & Dodero 1977).

1.11 Importance of Coronal Studies

The Importance of coronal studies are many-fold. First it gives an understanding of the physics of the Sun itself. Many of the solar phenomena are remaining to be understood in detail; existence of a hot corona, solar variability and energy balance in the atmosphere are just a few amongst them. It is now apparent that all stars in the main sequence emit x-rays, primarily thermal bremsstrahlung which comes from an extended atmosphere with a density of about 10^9 atoms/cm^3 and a temperature, in excess of 10^6 K. One of the basic problems in x-ray astronomy is the question- why stars universally possess a corona which is about 10^2 times hotter than its surface? (Parker 1990).

Since for stars other than Sun, only the integrated spectrum can be obtained with the currently available technology, the only alternative, at least for the time being, is the coronal observations. The existence of stellar chromospheres was established for stars like Capella and Procyon from the observation of emission lines like H and K lines of $Ca\,II$ and 10830 Å metastable line of He, which are typical of solar atmosphere also (Zirin 1971). The physical proximity of solar corona provides an astrophysical laboratory for atomic and plasma physics with temperature and density regimes unattained in terrestrial laboratories (Vaiana & Rosner 1978). Study of hot plasma in strong magnetic fields such as the corona also give an insight to distant astrophysical objects like pulsars, quasars and active galactic nuclei. One other possible field which is to be benefitted from such studies is the nuclear fusion

which appears to be a potential terrestrial energy source, as, the most promising approach to fusion involve the confinement of hot plasma by magnetic fields (Wolfson 1983). Since the corona expands as the solar wind which is continually being swept out into interplanetary space, it influences the state of the earth's van Allen belts, magnetosphere, ionosphere and other atmospheric phenomenon.

1.12 Relevance and Importance of the present study

As it was earlier pointed out , the study of the velocity field spectrum is of utmost importance for the basic understanding of the corona. Though the velocity field in the chromosphere-corona transition region is well studied through spacecraft-borne measurements in the last two decades, the velocity field in inner corona remains to be understood in detail. Emission lines show evidence for nonthermal motions in the transition region (10–25 $km\,s^{-1}$) as well as in the corona (10–30 $km\,s^{-1}$). The presence of mass motions in corona is not well established except for the transient events such as coronal mass ejection events and a few observations associated with active regions. The correlation of the occurrence of velocity fields in the corona and the phase of the solar activity cycle, if any, is also worth looking for. Although the temperature distribution of the corona is well studied, there are not many attempts to relate temperature to the various magnetic field structures. By studying the temperature structure in various position angles in detail, it is possible to relate the temperature and the magnetic field structure.

It is well known that the green line intensity is a good indicator of solar

activity. Intensity distribution in various coronal regions, with respect to the phase of solar activity may reveal more details about the physical conditions in the corona. Also line profile studies may provide very valuable information on mass motions and turbulence. X-ray and EUV images of the corona reveal the ubiquitous nature of loops in quiet as well as in active regions. Coronal pictures in visible spectrum also show evidence of loop structures (Smartt 1987). It is expected that line profiles should also reveal the presence of loops and signatures of loop flows which are invariably seen in the transition-zone line profiles. Theoretical modelling of line profiles with known solar conditions and comparisons with the observed profiles may give deeper insight to coronal physics.

The excitation conditions of forbidden lines are not known in detail, especially regarding the relative roles of various excitation factors. Knowledge of the excitation mechanism is essential from the point of view of coronal modelling, since the particular excitation mechanism decides the functional form of the relation by which the physical quantities are related with the observed parameters. It is possible to get a good understanding of the excitation conditions from comparing the ratios of monochromatic intensity to white light intensity, with theoretically generated intensity ratios. From such studies, it is also possible to deduce the temperature variation in corona.

The aim and scope of the present study are the following.

1 To study the velocity field and temperature structure in solar corona, by analysing Fabry-Pérot interferograms of the corona which were obtained during the total solar eclipses of 1980 and 1983. Since the year 1980 lies at the solar maximum while 1983 is at a declining period, an intercomparison of various features of

the two, are of interest from the point of view of the role of the solar activity cycle.

2 To study the emission line profiles from different regions of corona in detail, so as to get information on mass motions, microturbulence and line intensity variations in the medium. In addition to this, to calculate the line shapes theoretically taking into account of the various factors such as thermal broadening, discrete plasma flows, microturbulence etc. and to see the agreement with the observed profiles.

3 To study the excitation mechanism of the coronal green line and to study the variation of the line to continuum ratio in various coronal regions. The line to continuum ratio, in turn, can provide an independent measure of temperature.

Chapter 2

Data Reduction Techniques

This chapter deals with the observations and data reduction techniques. Basic theory of the Fabry-Pérot interferometer is discussed in the beginning. A brief note on the instrumentation and observation is given, for which the details can be seen in Chandrasekhar (1982) and Chandrasekhar et al., (1984). Finally the digitization procedure and the various steps involved in the data reduction are discussed in some detail.

2.1   Fabry-Pérot Interferometer

Fabry-Pérot (FP) Interferometers have been widely used in astronomy especially since the development of high reflectivity dielectric coatings and the introduction of optically contacted etalons. High resolution and superior light gathering power combined with the ease of operation make it an ideal instrument for observing extended astrophysical objects such as the solar corona, emission nebulae, planetary nebulae

41

etc.

The advantage of using an FP is obvious from Jaquinot's studies who in the fifties made an investigation of different spectrometers and found that for every class of spectrometers, the luminosity is inversely proportional to its resolving power (Jaquinot 1954,1960).

$$\text{ie} \qquad \qquad L \times R = \text{constant} \qquad \qquad (2.1)$$

where the luminosity or the etendue of the spectrometer

$$L = \epsilon A\Omega, \qquad \qquad (2.2)$$

where ϵ is the transmission factor, A the effective area of the spectrometer and Ω is the solid angle subtended by the slit or the entrance aperture at the collimator.

$$(L \times R)_{\text{FP}} \simeq 30 \text{ to } 100 \ (L \times R)_{\text{grating}} \simeq 300 \text{ to } 1500 \ (L \times R)_{\text{prism}} \qquad (2.3)$$

Above relation holds only when the source fills the acceptance angle of the spectrometer. The large gain in the $(L \times R)$ for the FP is due to its large acceptance angle for a given resolving power. The advantage is known as Jaquinot advantage.

The Fabry-Pérot interferometer essentially consists of two optical plates (etalons) held parallel to each other at a fixed distance t. The inner surface of the plates are mirrored with a reflectivity slightly less than unity. The transmission of light through the plates is governed by Airy's function given by

$$A(\lambda) = I_0(\lambda) \left(\frac{T}{1-R}\right)^2 \left[1 + \frac{4R}{(1-R)^2} \sin^2 \left(\frac{2\pi\mu t \cos\theta}{\lambda}\right)\right]^{-1} \qquad (2.4)$$

where T is the transmission coefficient, R is the reflectivity of the mirrors, θ is the angle if incidence, μ is the refractive index of the medium between the plates in the etalon (Thorne 1974, Meaburn 1976).

42

The peak of transmission occurs when

$$2\mu t \cos\theta = n\lambda \tag{2.5}$$

where n is the order number.

Some of the important terms which characterize an FP are explained below.

- Free Spectral Range (fsr) is the spacing between the adjacent transmission peaks.

$$\Delta\lambda = \frac{\lambda^2}{2\mu t} \tag{2.6}$$

- Full Width at Half Maximum (FWHM or half width) of the Airy Profile, also called the resolution limit

$$\delta\lambda = \frac{\Delta\lambda}{N_R} \tag{2.7}$$

- Reflective Finesse

$$N_R = \frac{\pi\sqrt{R}}{1 - R} \tag{2.8}$$

- Peak Transmission of the Airy Profile

$$A_{max} = \frac{T^2}{(1 - R)^2} \tag{2.9}$$

- Reflective Contrast of the FP Fringe

$$C = \frac{I_{max}}{I_{min}} = \left(\frac{1 + R}{1 - R}\right)^2 \tag{2.10}$$

where I_{max} and I_{min} refer to the maximum and minimum intensity of the fringe.

In actual practice there may be various broadening factors in addition to the Airy function, which could reduce the contrast of the fringe (Hernandez 1966, Atherton 1981, Desai 1984). The Important factors are listed below.

43

i Microscopic flatness imperfections on the plate: If the distribution of the defects is assumed to be Gaussian, and the rms surface defect is given by λ/m_G, then the broadening function will have a width $\Delta\lambda/(m_G/4.7)$ (Chabbal 1953). Hence the defect finesse $N_{DG} = m_G/4.7$

ii Spherical plate defect: If the maximum departure in plate separation due to the spherical plate defect is given by λ/m_s, then, the broadening function due to this effect is a rectangular function of width $\Delta\lambda/(m_S/2)$ (Chabbal 1953). Corresponding defect finesse is the given by $N_{DS} = m_S/2$.

iii Non-parallelism of the plates:

If the maximum departure in plate separation due to non-parallelism of the plates is λ/m_P, then the broadening function due to this defect has a width $\Delta\lambda/(m_P/\sqrt{3})$, so that the defect finesse is given by $N_{DP} = m_P/\sqrt{3}$

iv Effect of finite aperture:

The aperture used to record the spectrum causes an extra broadening which is a rectangular function of width $\lambda\Omega/2\pi$ where Ω is the solid angle subtended by the aperture (Jaquinot 1960). The aperture finesse is then, given by

$$N_A = \frac{\Delta\lambda}{\lambda\Omega/2\pi} = \frac{2\pi}{n\Omega} \tag{2.11}$$

All the above functions if approximated by Gaussians, give the effective finesse of the interferometer

$$\frac{1}{N^2} = \frac{1}{N_R^2} + \frac{1}{N_D^2} + \frac{1}{N_A^2} \tag{2.12}$$

Whereas the above consideration of Jaquinot advantage apply only when Fabry-Pérot interferometer is used as a scanning spectrometer, it is primarily the imaging aspect which is more important when FP is used as an imaging spectrometer.

2.2 Observations

The solar coronal studies described in this thesis are based upon three sets of data obtained during the eclipses of 1980 & 83 and made available to the author for analysis. The observations are

   i FP observations of corona during 1980 total solar eclipse in the emission line FeXIV 5303 Å at Gadag, India.

   ii Coronal photographs in the emission line FeXIV 5303 Å and in the white light, obtained during 1980 total solar eclipse at Gadag, India.

   iii FP observations of corona during the 1983 total solar eclipse at Tanjung Kodok, Java, Indonesia in the emission lines FeXIV 5303 Å and FeX 6374 Å .

Details of each observation and the instruments used are described below.

i) A schematic diagram of the observational set up used in the FP observations is shown in Figure 2.1. Coronal light deflected by a coelostat (M) is passed through a 150 mm diameter (f/15) objective lens (O) and an interference filter (F). The beam is then collimated by lens (L_1) of focal length 80 mm (f/1.2), passed through the FP etalon (E) and then imaged on the 35 mm Nikon camera lens (L_2) of focal length 55 mm (f/1.2). The image scale on the film is as follows.

Solar disk (32′.4): 14.72 mm

Lunar disk (33′.2): 15.15 mm

Four exposures were taken with durations 4,10,30 and 90 sec. The important instrumental parameters used in the analysis are listed below.

   Etalon parameters:
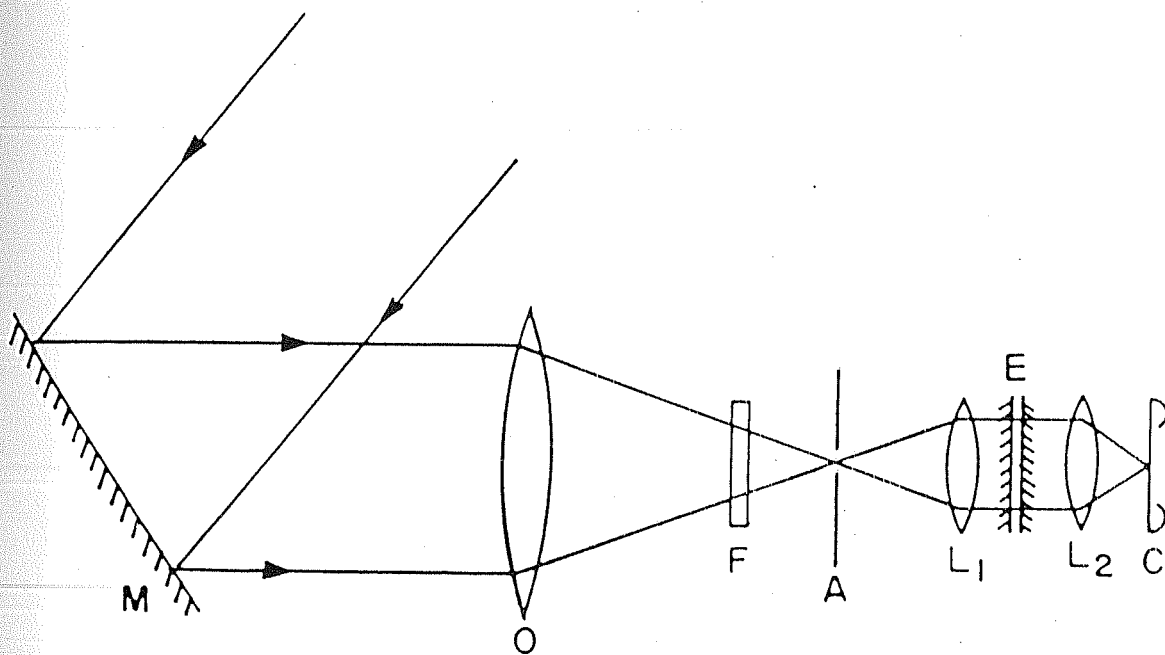
Fig. 2.1 A schematic diagram of the instrumental set up used
in 1980 observations; description is given in the text.

Type   : Air spaced optically contacted etalon

Effective plate diameter   : 40 mm

Plate flatness   : $\lambda/100$

Quoted air spacing   : 300 μm

Reflectivity at 5303 Å   : 87±1 %

Free spectral range (at 5303 Å)   : 4.65 Å

Net finesse   : 16.6

Instrumental resolution   : 0.28 Å

Filter parameters:

Type   : Interference filter

FWHM   : 7±1 Å

Peak transmission   : 25 %

Peak wavelength   : 5304.8 Å at the operating

                                               temperature 35° C

Equivalent width of the filter   : 4.50 Å

Film:

type   : Kodak TriX panachromatic film (400 ASA)

Grain size : 20 μm

ii) The corona was photographed during totality in the green emission line using a 10 Å band width filter and an 8 inch f/10 Celestron telescope. The film used was Kodak TriX 35 mm with a grain size of 20 μm. Exposure times used were 5,15 and 45 s.

A series of white light photographs were obtained during the totality with a 3.5 inch f/16 Questar telescope. They were recorded on a pre-calibrated Kodak PlusX (125 ASA) 35 mm film. A polaroid was inserted in the ray path, which was oriented successively at relative angles 0°, 45°, 90° and 135°. At each polaroid position, three pictures with exposure times 1/4, 1 and 3 s were taken.

iii) The experimental set up used for the 1983 observations was similar to the one which is used for the 1980 observations, except that a dual channel was introduced to record the interferogram in two emission lines viz. red and green coronal lines. The incoming beam was separated into two channels (the reflective and the transmission modes) by a multilayer dielectric beam splitter, kept at an angle 45° to the optic axis. The green line was recorded in the transmission mode and the red line was recorded in the reflective mode. The two beams then entered two separate optically contacted interferometers, operating in off-axis mode. Interference fringes thus produced, were recorded on a fine grain film. Details of the green channel are given below.

Etalon	: Optically contacted etalon
Working aperture	: 40 mm
Quoted spacing	: 300 μm
Reflectivity	: 87 %
Finesse	: 14.2
Instrumental width	: 0.33 Å
Free spectral range	: 4.69 Å
Filter used	: 5 cm, circular, dielectric interference filter
Peak wavelength of the filter	: 5303.20±0.77 Å
Band width of the filter	: 6.7 Å
Peak transmission	: 46.3 %
Film used	: Kodak 2415

2.3   Data Reduction

Many photographs and interferograms were obtained from the above-mentioned observations. However, the present thesis is concerned only with the following frames.

1. 30 s exposure interferogram of the 1980 eclipse observations.

2. 10 s exposure interferogram of the 1980 eclipse observations.

3. 4 s exposure interferogram of the 1980 eclipse observations.

4. 15 s exposure filter photograph of the 1980

5. White light photograph with no polarizer

6. White light photograph with polarizer.

7. 3 m 30 s interferogram of the 1983 eclipse.

The two interferograms obtained from the 1980 observation are shown in Figures 2.2 and 2.3. The first step in the data reduction was the digitization of the selected frames. This was done at Indian Institute of Astrophysics, Banglore, India using the Perkin-Elmer Photo Digitizing System (PDS).

2.3.1 Photo Digitizing System

Photo digitizing is the extraction of information into computer-compatible format from spatially-distributed data such as photographs (PDS manual, Perkin-Elmer). The working principle of PDS is as follows. A beam of light is passed through a pre-defined aperture (picture element or pixel) in the sample and allowed to fall on the face of a photomultiplier tube (PMT). The intensity of the light falling upon the PMT at any instant is inversely proportional to the transmission in the sampling aperture of the specimen. The analogue output of the PMT is periodically sampled, digitized and stored on a magnetic tape for subsequent manipulation in a computer.

The specimen was divided into two-dimensional array of pixels of the required size. During the scan, each pixel was assigned a numerical value which is proportional to its photographic density. The pixel size chosen for digitization for a particular frame depended on two criteria, i) the grain size in the film ii) the resolution required for
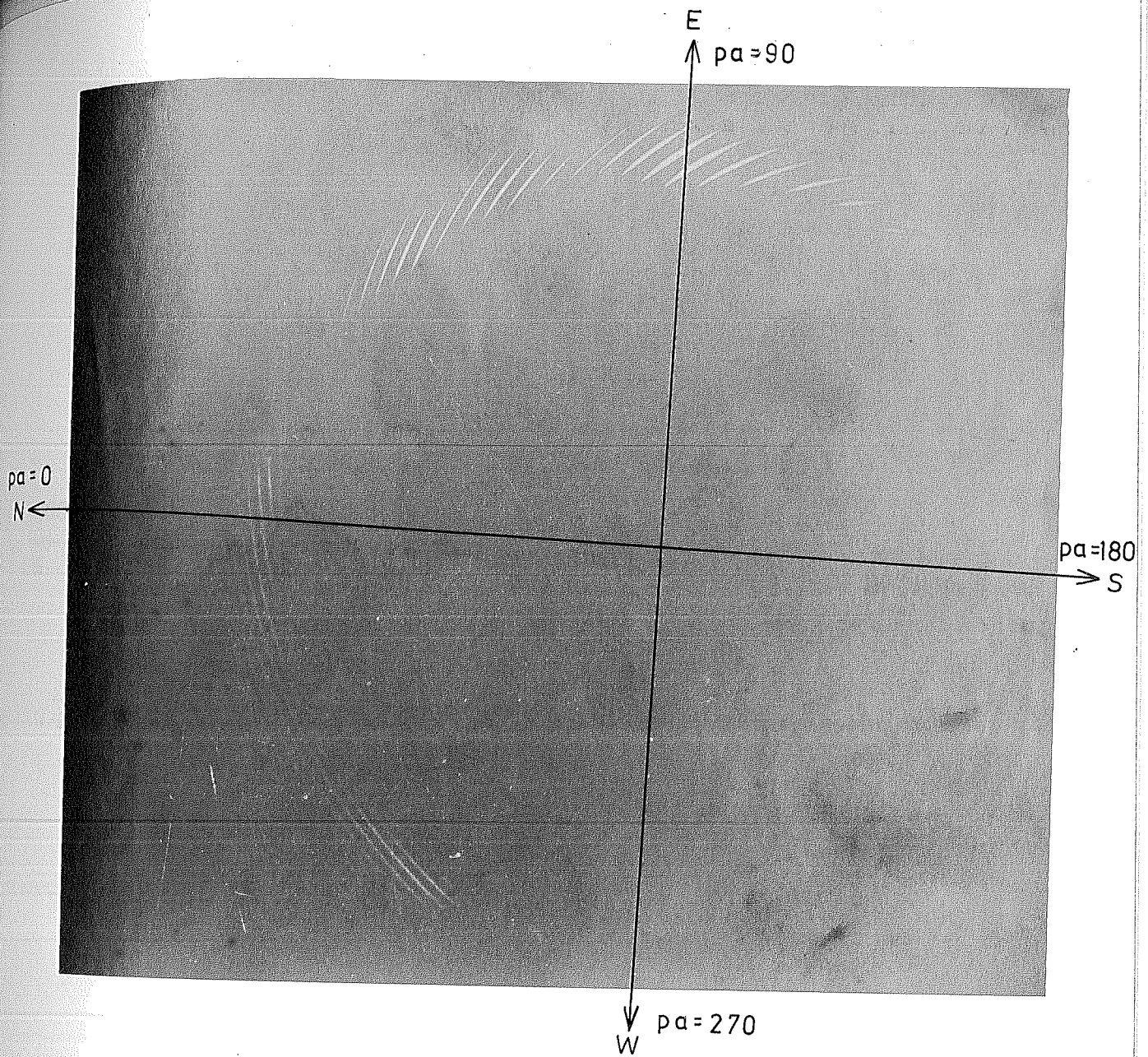
Fig. 2.2   10   sec.   exposure   interferogram   of   the   solar   corona
obtained   from   1980   observations   (Chandrasekhar   1982).
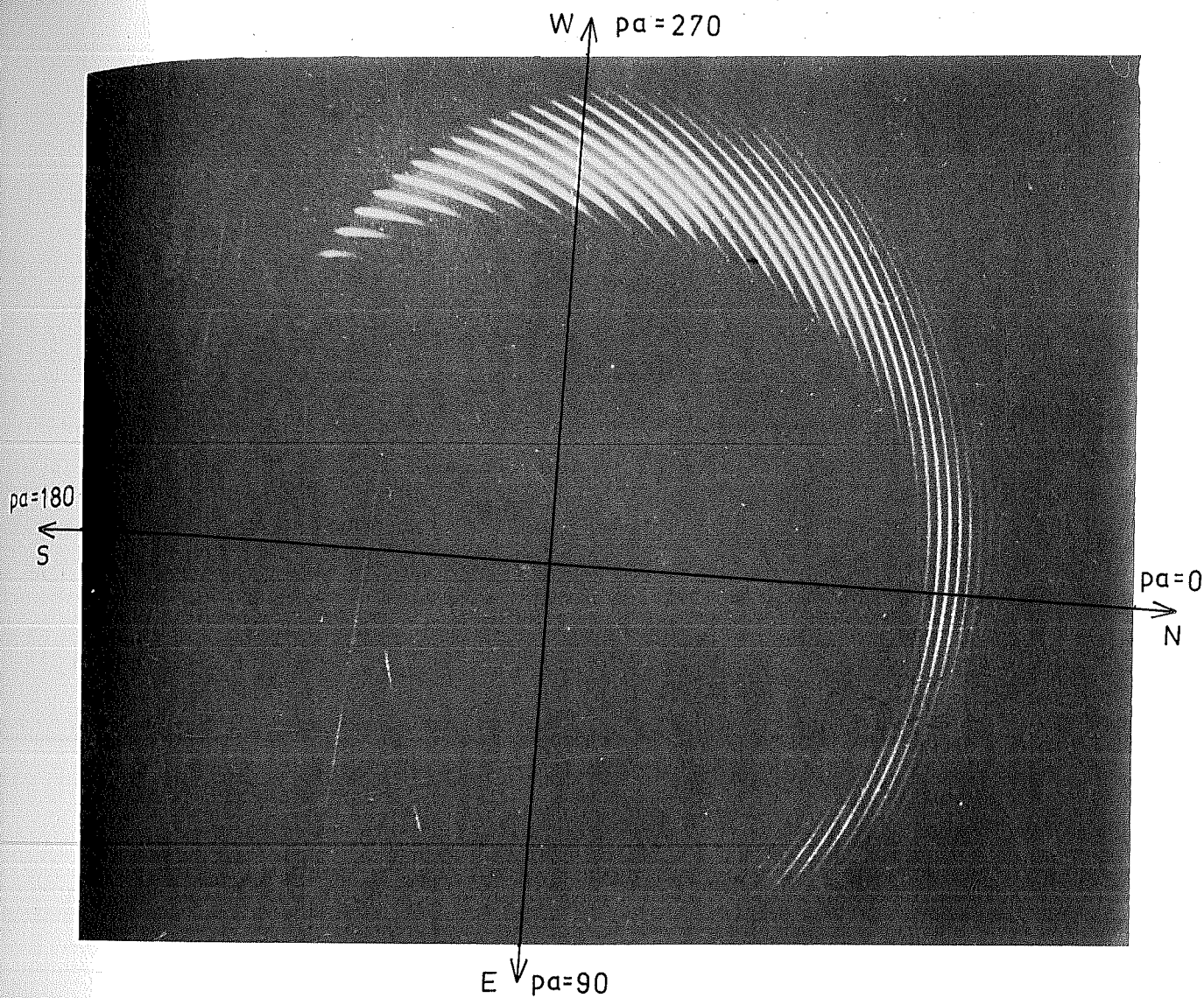
Fig. 2.3   30   sec.   exposure   interferogram   of   the   solar   corona
obtained from 1980 observations   (Chandrasekhar 1982).

a particular study. Thus for the 1980 interferogram, for which the grain size was 20 μm, the selected pixel size was $10\mu m \times 10\mu m$. For the 1980 coronal photographs, which were of the same film grain size, the pixel size chosen was $20\mu m \times 20\mu m$. The interferogram of the 1983 observation in which a fine grain size was used, pixel size used was $5\mu m \times 5\mu m$.

2.3.2 Analysis

The photographic density recorded at the pixels is related to the transmission according to $D = -\log T$. The first step in the analysis is to convert the photographic density into relative intensity in the film . A photographic characteristic curve, which is a plot of D versus logE was used for this purpose. A step-wedge was imprinted on the same film for which the $\log E$ values are known for the different steps, and developed alongwith the actual exposures. The density at each step was then measured and was plotted against logE. Relative intensity at any point in the film can be now easily calculated, by interpolation. The relative intensity against the distance from a reference point was found out by picking out the values of the corresponding pixels, after appropriate averaging.

A series of computer programs were developed which sequentially do the following.

i) Determination of the Reference Point for Scanning

The center of the fringe system and the solar center do not coincide in interferograms, because of the off-axis mode of operation of the interferometer. This mode of

53

operation was pre-decided, to gain a variable spatial resolution in different coronal regions. The reference point is the point from where every scanning should originate. Fabry-Pérot fringes are circularly symmetric, so the reference point for interferogram is the fringe center. Possible fringe maxima positions were located for this purpose, by scanning the PDS data record by record and taking only those points which satisfy the two criteria; i) the pixel density in question should be above than that of about 15 pixels, the exact number being dependent upon the inter-fringe separation, on either sides. ii) the selected pixel locations must have a density, more than a threshold value. Density points thus selected were plotted and compared with the actual interferogram and the noise points were removed. The coordinates of fringe maxima were then subjected to a least square circle fitting program, which could give an accuracy upto ±3 pixels in the calibration fringes. For actual interferograms, there may be genuine shifts in the fringe maxima position from the circular shape due to actual Doppler velocities present in the medium, so only a most probable centre can be defined.

For the coronal photographs, the obvious reference point is the solar centre. This was obtained again by a least square circle fit into the coordinates of the lunar limb which eclipsed the Sun. The digitized solar coronal image was displayed for this purpose, on an image processing system and the coordinates of the lunar limb which is seen as very sharp boundary, were noted down.

ii) Matching the Frames

The four second exposure interferogram clearly recorded the third contact position. The actual negatives of the interferograms were magnified upto 18 times in a slide projector and the individual fringes were matched to get the third contact position

54

in each of them. A one to one correspondence was thus obtained. Knowing the coordinates of the third contact point, all the frames were transferred into solar coordinates. For coronal photographs, matching was done by displaying the digitized images on an image processing system, and then identifying the individual streamer structures, which were seen very clearly. Both the techniques could give a matching better than one degree accuracy.

iii) Obtaining the Intensity Profiles

Once the reference point for scanning is established, the intensity profile in a particular direction may be obtained by picking out the values of intensity of all the pixels lying in that particular direction. A computer software was developed for this purpose. Given the coordinates of the reference point, angle and the scanning interval, the program calculates the coordinates of the pixels defining a particular direction and then picks out the density values from them. Averaging the densities in the nearby pixels was found to be necessary, to reduce the noise. Averaging in the four nearest pixels suffice for some frames. However in the coronal interferograms, a more detailed averaging process involving the nine nearest pixels was accepted. The pixels were denoted as (1,1), (1,2), (1,3), (2,1), (2,2), (2,3), (3,1), (3,2) and (3,3). To find out the density value at a point which is situated in the pixel (2,2), the density values d_{11}, d_{12}, d_{21}, d_{22}, were averaged and set equal to D_1. d_{12}, d_{13}, d_{22}, d_{23} are averaged to find D_2. Similarly D_3, and D_4 were found out. Now, a two-dimensional linear interpolation was used to obtain the density at x (Press et al., 1986). From the density value thus obtained, the relative intensity can be interpolated from the photographic characteristic curve. The procedure was then repeated throughout to get the intensity profile as a function of distance from the reference point. The intensity profiles in a

typical scan direction are shown in Figure 2.4.

iv) **Wavelength Conversion**

Wavelength conversion of the x-axis, in the case of interferogram fringes, easily follows from the constructive interference condition in FP etalon.

$$2\mu t \cos \theta \; = \; n\lambda$$

Differentiating,

$$-2\mu t \sin \theta \, \Delta\theta \; = \; n\,\Delta\lambda$$

$$-tan\theta \, \Delta\theta \; = \; \frac{\Delta\lambda}{\lambda}$$

We have, for small θ, $\tan \theta \approx \theta \approx \frac{R}{F}$
and hence,

$$\Delta\lambda = -\frac{\lambda R}{F^2} \Delta R \tag{2.13}$$

The minus sign indicates that R and λ are in opposite sense. Alternately, if the value of F is not known exactly, then one may use

$$2\mu t \cos \theta \; = \; n\lambda$$

$$2\mu t \left(1 - \frac{\theta^2}{2}\right) \; = \; n\lambda$$

$$R^2 \; = \; 2F^2 - \frac{F^2}{\mu t}n\lambda \tag{2.14}$$

For two adjacent fringes, the difference

$$R_{i+1}^2 - R_i^2 = \frac{F^2\lambda}{\mu t} \tag{2.15}$$
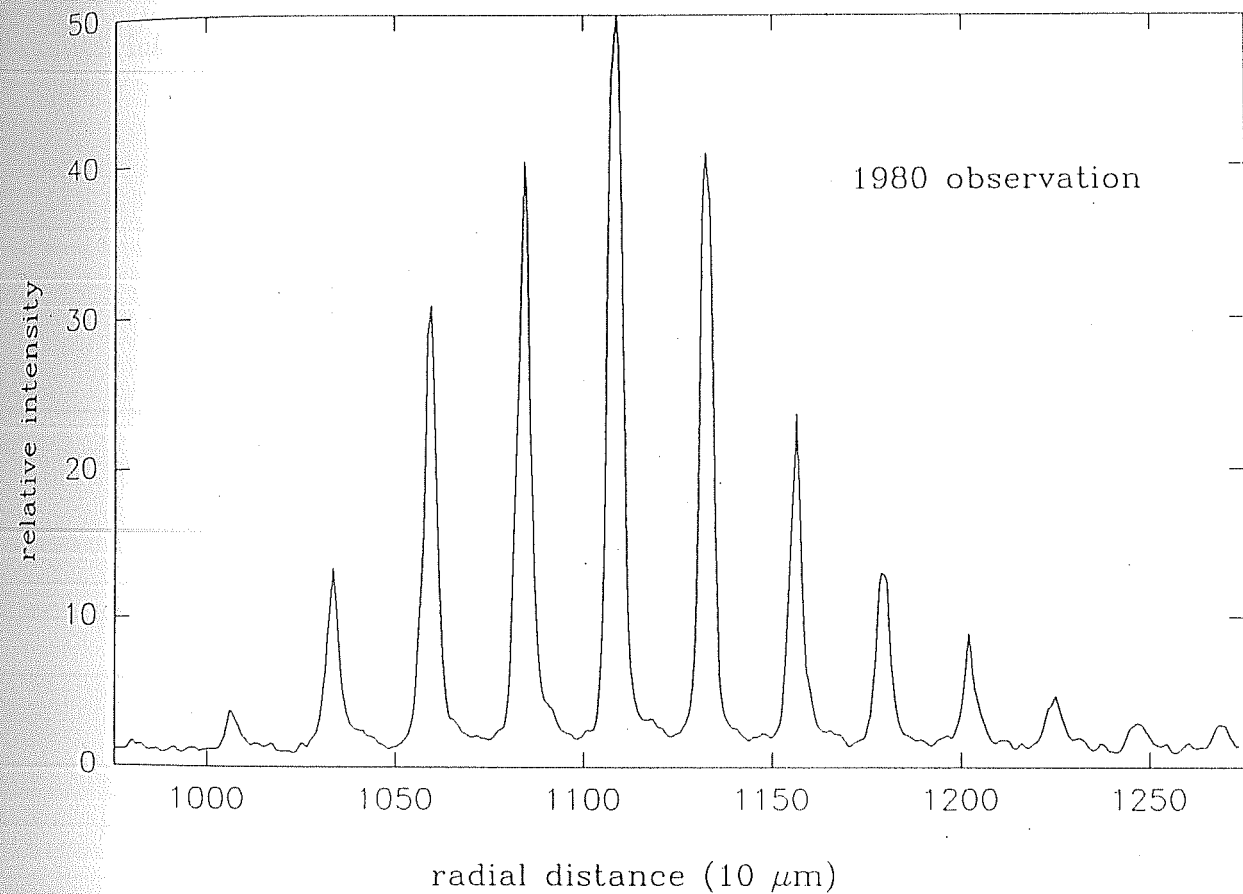
Fig. 2.4   Intensity profiles in a typical scan direction from the 1980 interferogram; relative intensity in arbitrary units plotted against radial distance from the fringe centre in the interferogram.

is a constant for a given λ. Now equating this to the fsr, one may find out the wavelength interval corresponding to the displacement of the point in R from the known fringe peak.

The intensity profiles obtained were further examined for detailed kinematical informations. The various methods used are described in the following chapters.

Chapter 3

Wing Intensity in Fabry-Pérot fringes

One of the outstanding differences that is markedly seen, when the 1980 and 1983 eclipse interferograms are compared, is that fringes in the 1980 eclipse interferograms show much lower contrast. The observed contrast showed large variations in radial and azimuthal directions. In this chapter the probable mechanism which cause the reduction of contrast are discussed. The reduction of contrast essentially implies the presence of rather large intensity in the wing region of the FP line profiles. Appropriate corrections were performed for various contrast reducing factors which are inherent in the FP etalon system. In addition to this, the presence of continuum radiation in nearby wavelengths may contribute to the wing intensity. This factor is computed in detail for the given FP, for the actual values of line and continuum intensities in the corona, which were independently measured. Here, the line intensity refers to the integrated intensity across the line while the continuum intensity refers

to the white light intensity measured per angstrom. Calculations were performed to remove the continuum intensity which may be present at the wings. Wing intensity refers to the additional intensity which is still present in the fringe minima position after the above corrections. It is found that the wing intensities show a marked correlation with the coronal position angles. The results and a probable interpretation are given in the final sections.

3.1   Factors which affect the Wing Intensity

There can be five factors which may broaden an FP fringe and consequently raise the wing intensity. They are

- Instrumental broadening

- Broadening due to the finite width and intensity of the observed profile

- Presence of continuum radiation in the nearby wavelengths

- Presence of large scale turbulence in the medium

- Presence of fast moving discrete components along the line of sight

In the following section the various instrumental broadening factors are briefly explained, and the appropriate contributions as applied to the observed profiles are mentioned.

The various instrumental broadening factors are explained in chapter II. Closely following the lines of Chabbal (1953), we calculate the expected contrast in a given

fringe taking an instrumental function of width 0.28 Å as obtained from the calibration fringes and a source function having a width approximately equal to the observed Doppler width. The expected contrast is then compared with the observed contrast in the line profile and the difference is taken as the wing intensity.

The observed contrast in the FP fringe is calculated as follows. Relative intensity values at the fringe minima positions ie at the two edges of the fringe profile are read out from the PDS data. A straight line is fitted to them and the fitted value at the center is taken as the average fringe minimum intensity. Observed contrast is then obtained by dividing the fringe peak intensity by the fringe minimum intensity. Relative intensities at the FP wings are small compared to the fringe peak intensities, and hence the error in their measurement is rather high, being about 10%.

The contrast in an ideal etalon is approximately $\frac{4N_R^2}{\pi^2}$. However in practice there may be many contrast reducing factors. They may be conveniently treated in terms of transmission factors associated with the etalon. The expected contrast for a fringe may be written as (Chabbal 1953)

$$C_{\mathrm{exp}} = \frac{\tau}{\tau_A} \frac{4N_R^2}{\pi^2} \qquad (3.1)$$

where N_R is the reflective finesse, N_R=22.5, for the given FP with reflectivity R=0.87. τ is the actual transmission in the FP, which is given by

$$\tau = \tau_A \times \tau_B \times \tau_E \times \tau_F \qquad (3.2)$$

Where,

τ_A is the transmission factor due to the absorption losses in the reflective layers of the etalon. For the dielectric reflective coatings, absorption is negligible and hence τ_A is approximately one.

τ_B is the transmission factor due to the source not being monochromatic and is given

by Chabbal(1953). Presence of microturbulence in the corona may also contribute to the line broadening, the distribution of which is taken as a Gaussian, and was treated together with the thermal broadening.

τ_E arises due to etalon defects. Plots of τ_E as a function of Airy width are given by Chabbal (1953).

τ_F arises due to the scanning function. For the typical grain size of 10μm, the solid angle subtended by the grain at the imaging lens is very small and correspondingly the broadening due to the scanning function is negligible. Hence τ_F is approximately one.

For the given FP interferometer, fsr=4.65 Å , and for the coronal green e-mission line of width 0.75 Å which accounts for a two million degree corona, and an assumed microturbulent velocity of 7 $km\,s^{-1}$, we find τ_A=1, τ_B=0.40, τ_E=0.90, τ_F=1, the expected contrast is about 60. For the observed width of coronal line profiles 0.60–1.0 Å , the expected contrast is in the range 70–54.

The actual wing intensity may be written as

$$I_w = I_m \left(\frac{1}{C_{obs}} - \frac{1}{C_{exp}} \right) \tag{3.3}$$

where C_{obs} is the observed contrast in the fringe, I_m is the fringe peak intensity. A computer program was written to do the above calculations sequentially. Various steps involved in the calculation may be summarized as following.

- Determination of the width of the line profile

- Interpolation to find τ_B from Chabbal (1953)'s curves

- Calculation of τ using τ_E from instrumental profile and τ_A and τ_F

62

- Determination of the observed contrast

- Calculation of the wing intensity

3.1.1   Effect of Continuum Radiation in nearby Wavelengths

If the continuum radiation in nearby wavelengths is appreciable in comparison with the line intensity, the observed wing intensity may be affected by the continuum radiation. For an ideal etalon and Lorenzian line profile, Hernandez (1966) gives the fraction of the continuum transmitted as

$$f = \frac{1}{2\pi A(0)} = \frac{1-R}{1+R} \tag{3.4}$$

where $A(0)$ is the minimum intensity of the Airy profile. However, with a line profile which is substantially broadened thermally, and for an actual etalon whose instrument function is broader than the Airy profile, the continuum contribution may be different. To see this effect, a simple coronal line profile with a finite contribution from the continuum radiation, as recorded by the instrument was modelled. A Gaussian line profile with halfwidth 0.75 Å with possible values of continuum was assumed as the source function. Line to continuum intensity ratio was found to be in the range 100–1 in the coronal heights 1.10–1.30 $R_\odot$ (see chapter v).

The recorded line profile should be obtained by the Fourier convolution of the source function with the instrumental function. The instrumental profile is obtained by scanning the calibration interferogram, which was obtained with a laboratory source, mercury green line at 5461 Å . An Airy function with halfwidth 0.23 Å convolved with a Gaussian function of equal halfwidth, which account for the additional

63

broadening factors, was found to describe the instrumental profile reasonably well. The instrumental profile and the convolved function are shown in Figure 3.1.

In the next stage, we have taken a Gaussian source function with a certain value of the line to continuum intensity ratio and computed its transmission through the interference filter. The transmitted intensity was then convolved with the instrumental function by Fourier transform methods. A computer program was written and used for this purpose. The Fourier convolution of the source function $S(\lambda)$ and the instrument function $I(\lambda)$ may be given as

$$O(\lambda_k) = S * I\,(\lambda_k) = \int_{-\infty}^{+\infty} S(\lambda_k - \lambda_i)\,I(\lambda_i)d\lambda \qquad (3.5)$$

The above formula may be given in the discrete form as (Press et al., 1988)

$$O(\lambda_k) = S * I\,(\lambda_k) = \sum_{\lambda_i=\lambda_1}^{\lambda_2} S(\lambda_k - \lambda_i)\,I(\lambda_i) \qquad (3.6)$$

where $(\lambda_2 - \lambda_1)$ is the filter pass band.

The line to continuum intensity ratio is varied through its possible values and the calculations were performed. In Figure 3.2a, we have plotted, the source function with a typical line to continuum intensity ratio of 10, filter transmission profile and the transmitted source function. The instrument function and the convolved line profile are shown in Figure 3.2b and table 3.1 gives the details of calculation. It may be seen that, unless the ratio of line to continuum intensity is less than 10, continuum contribution has no effect on the fringe contrast. It is evident from the table that as $I_c \rightarrow 0$, ie when I_l/I_c is large, the expected contrast C_{exp} almost become equal to the value obtained from Chabbal (1953).

Table 3.1: Contribution of the continuum intensity to the fringe contrast: The first column of the table gives the value of the ratio of line to continuum intensity, the second and third give the computed fringe maxima intensity and fringe minima intensity for a normalized source function. The next two columns give the percentage of the ratio of wing intensity to peak intensity and the contrast arising due to continuum contribution.

I_l/I_c	I_m	I_w	I_w/I_m %	C_{exp}
1	0.794	0.0727	9.15	10.93
2.5	0.782	0.0358	4.57	21.87
5	0.778	0.022	2.83	35.36
7.5	0.776	0.0183	2.35	42.52
10	0.775	0.0154	1.98	50.46
15	0.774	0.0129	1.66	60.11
20	0.774	0.0123	1.59	62.67
50	0.773	0.0097	1.25	80.10
100	0.773	0.0091	1.18	84.71
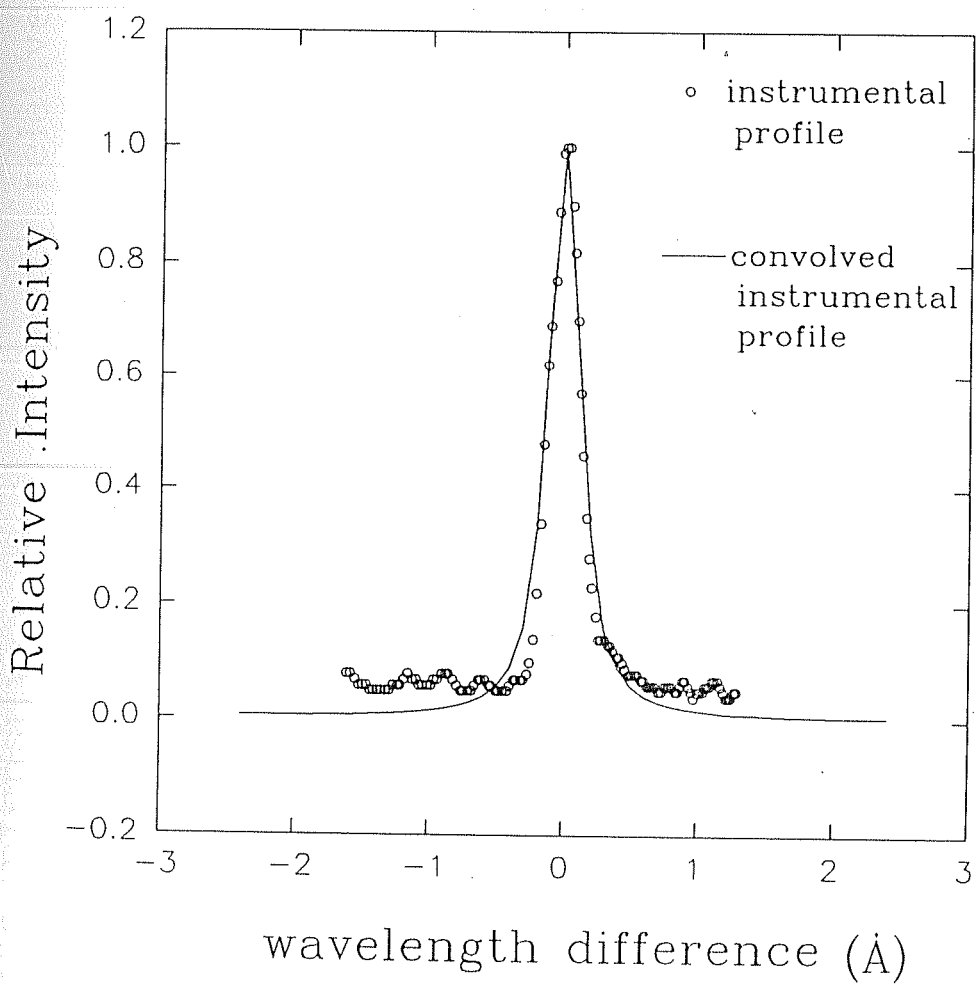
Fig. 3.1　Instrumental profile; relative intensity in arbitrary units against wavelength difference from the maximum.
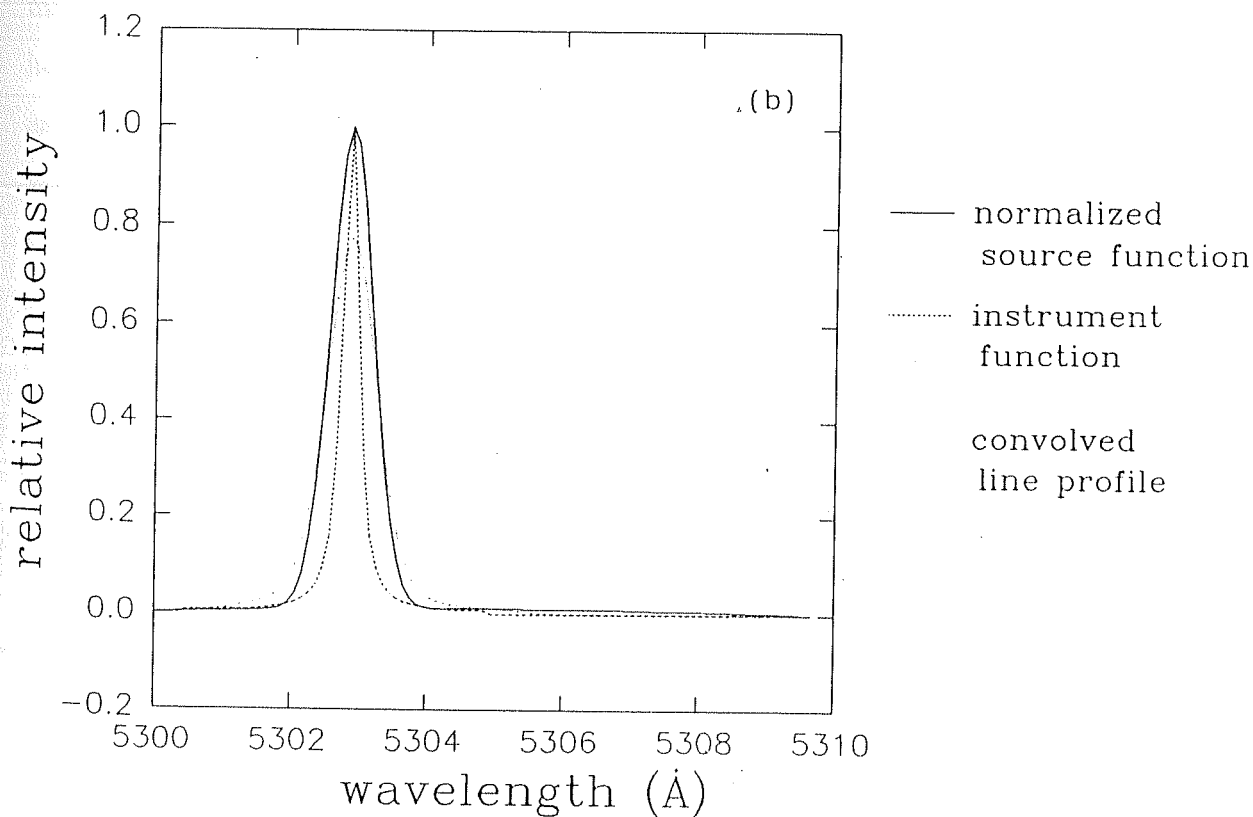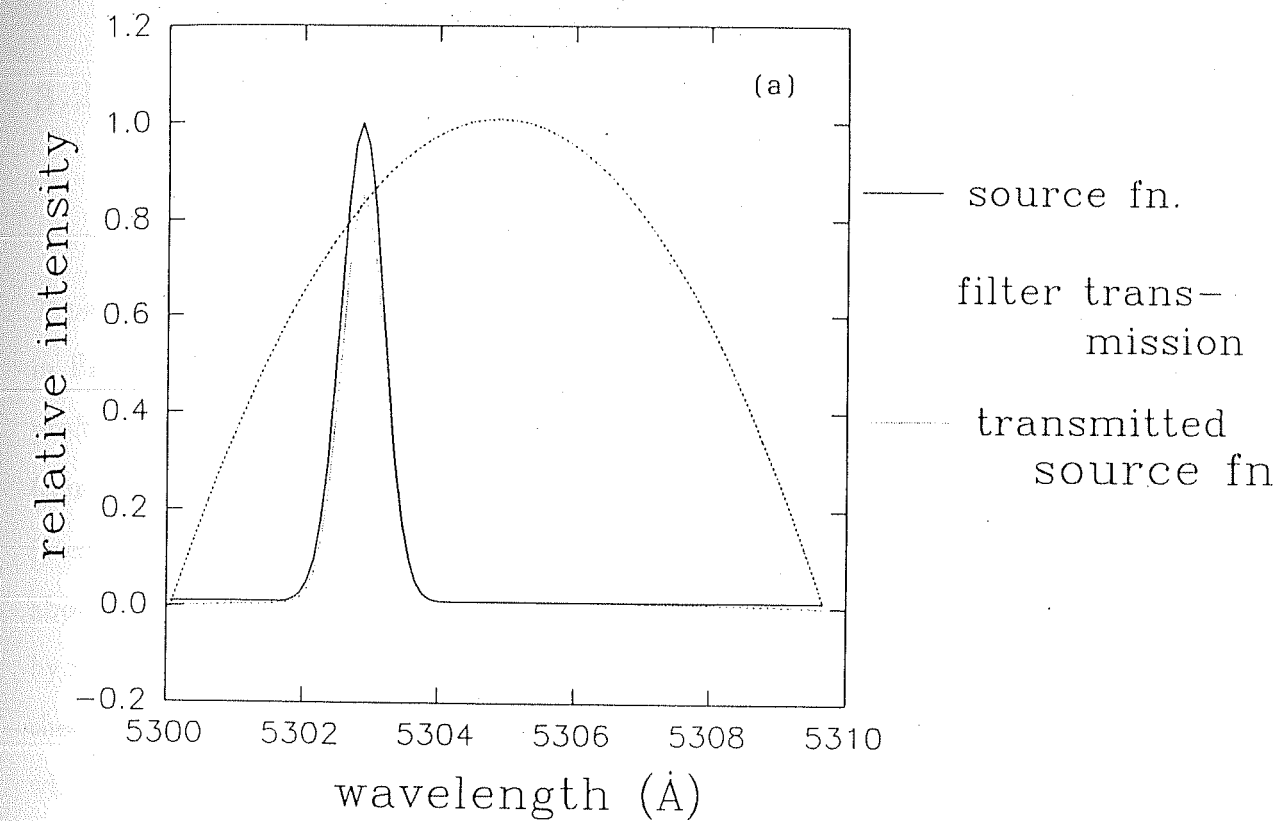
Fig. 3.2   Details of the convolution program; relative intensity
in arbitrary units is plotted against wavelength for the
mentioned curves.

3.2 Presence of Discrete Components in the Corona

Typical intensity profiles derived from the 1980 and 1983 observations are shown in Figure 3.3. It may be noted that wing intensities are large in the 1980 fringe profiles while they are very low in the 1983 profiles. About 500 line profiles derived from FP interferograms belonging to the 1980 corona were examined to see the wing intensities. Many of the line profiles showed an elevated wing intensity. From the above section, it is clear that the observed reduction of contrast cannot be explained by the contribution of continuum intensity to the wings. Wing intensities must be then dominated by large scale turbulence or by Doppler shifted green line components which arise due to the discrete moving components in the line of sight. Large scale turbulence with a most probable velocity of $\sim$150 km s^{-1} , if present in the corona, may explain such an effect. However, the presence of such large scale turbulence have not been reported in the corona. Moreover, line profiles often show a distinct asymmetry which is not normally expected for the distribution of turbulent eddy velocities. The expected distribution of large scale turbulent velocities is a Gaussian, and hence may contribute to the emission line broadening. However, an asymmetry of the line profile may not result from such a case. On the other hand, large scale flow observed in coronal loops seems to be a good candidate in explaining the wing intensity. Also, it is to be noted that many of the line profiles show signatures of moving components (see chapter 4). The presence of discrete components such as coronal loops are seen in large number in the coronal pictures (Vaiana & Rosner 1978, Priest 1984). Coronal loop flows are reported by many authors (Athay et al., 1983b, Kopp et al., 1985).
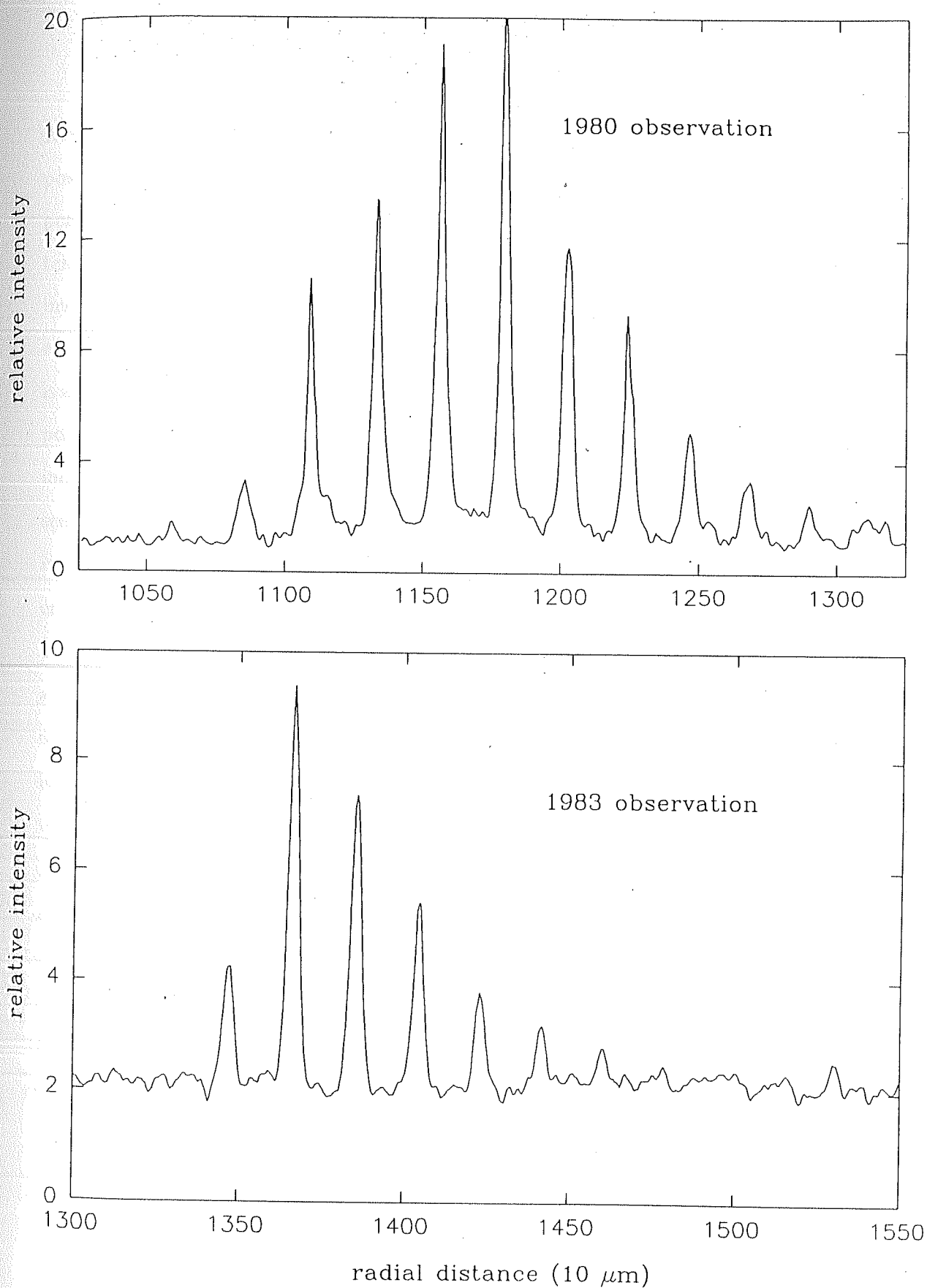
Fig. 3.3 Typical intensity profiles in the 1980 & 1983 interfero-
grams; relative intensity in arbitrary units plotted against
radial distance from the fringe centre in the interfero-
gram. Line profiles in the 1980 interferogram show excess
intensity at the wing region, as compared to that of
1983 interferogram.

It was found that wing intensities have a pronounced correlation with the coronal position angles. This is illustrated in Figure 3.4a–l, where we have plotted the fringe peak intensities against coronal radial distance in the upper half, and the wing intensities against coronal radial distance in the lower half. Observed values in a 2.5° interval on either side of the particular position angle are included in every plot. This explains the large scatter in the diagram. A least square third degree polynomial fit is also given alongwith, to see the trend. The position angles 350, 10 and 20 represent polar coronal hole region. The existence of wing intensity at these position angles indicates the presence of discrete components in the coronal hole region. It may be seen that at these position angles, the wing intensities roughly follow the fringe peak intensities. The variation of fringe peak intensities in coronal heights can be taken as the variation of green line intensity. The line intensity reflects the excitation conditions under which the particular emission line originates. In other words, it is a representative of the physical conditions existing in the medium such as electron density, temperature and chemical abundance. Since we are dealing with the same ion, chemical abundance need not be taken into account. The coronal green line intensity is found to be a strong function of temperature and electron density (Jordan 1969, Raju & Singh 1987, Raju et al., 1991). Thus, the covariation of wing intensity and line intensity implies similar excitation conditions existing in the regions from which they arise. Since the wings represent discrete components and the line peaks represent the ambient medium (see chapter 4), this indicates the similar physical conditions prevailing in them. A large number of coronal loops dissipating into the ambient medium may explain such an effect.

In the remaining position angles, however, line intensity and wing intensity do not show covariation. This must, then imply the dissimilar physical conditions prevailing in the discrete components and in the ambient medium. In the case where

70
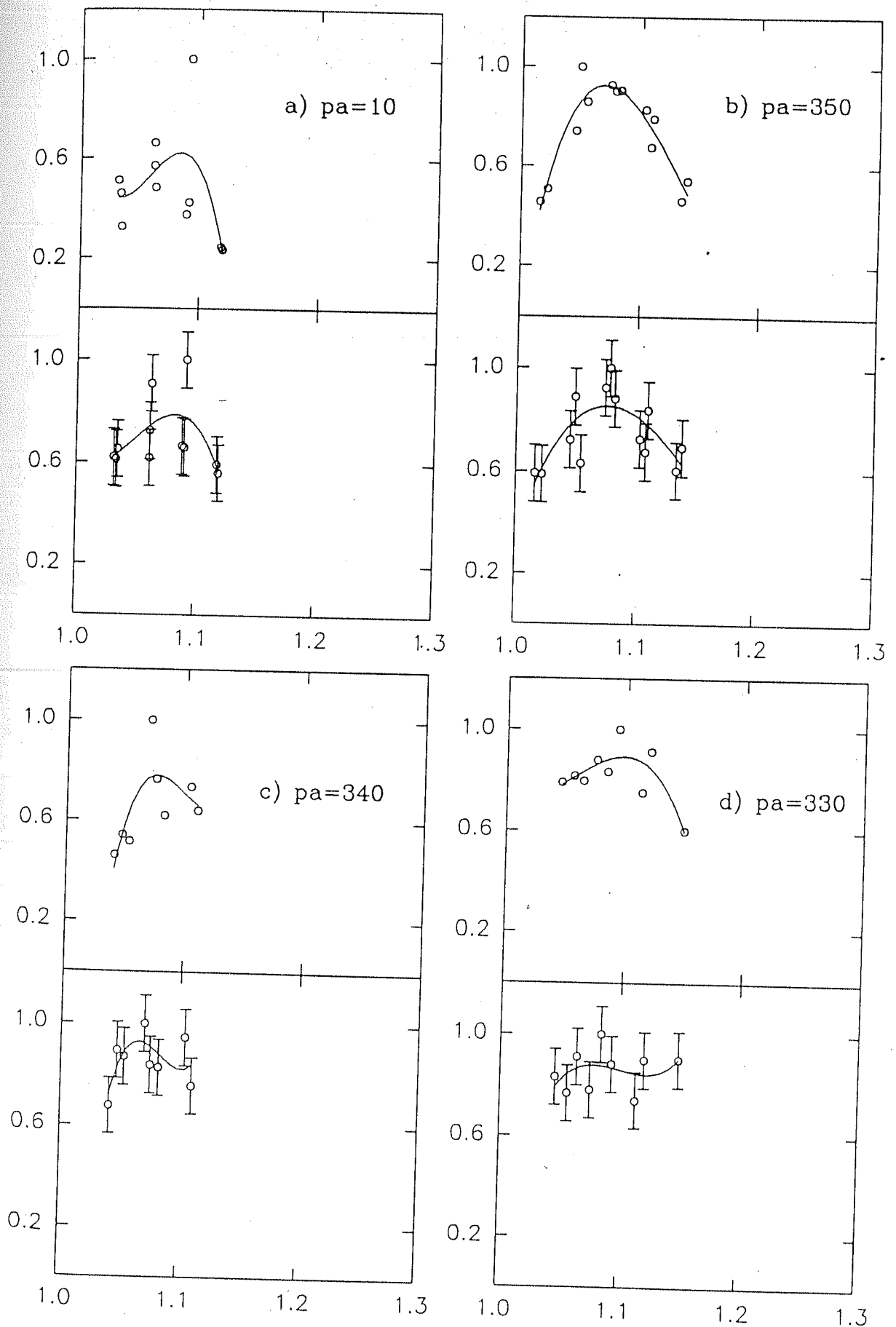
Fig. 3.4   Relative intensity in arbitrary units is plotted against
coronal radial distance in units of $R_{\odot}$; the upper half
of each graph represents the fringe peak intensity and
the lower half represents excess intensity in the wings;
respective position angles are mentioned.

e) pa=320

f) pa=310

g) pa=290

h) pa=290

Fig. 3.4 continued

i) pa=280

j) pa=270

l) pa=260

l) pa=250

Fig. 3.4 continued

73
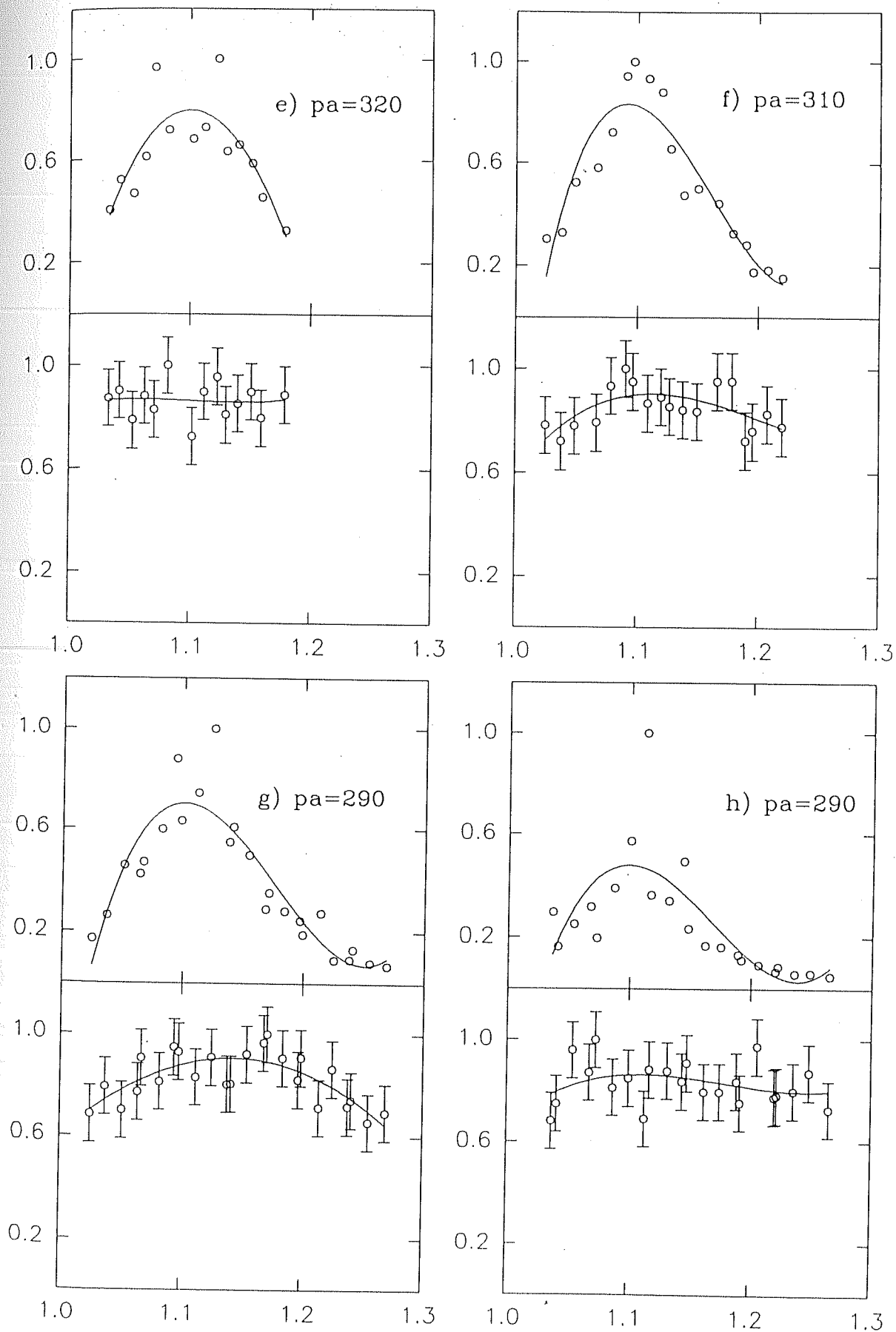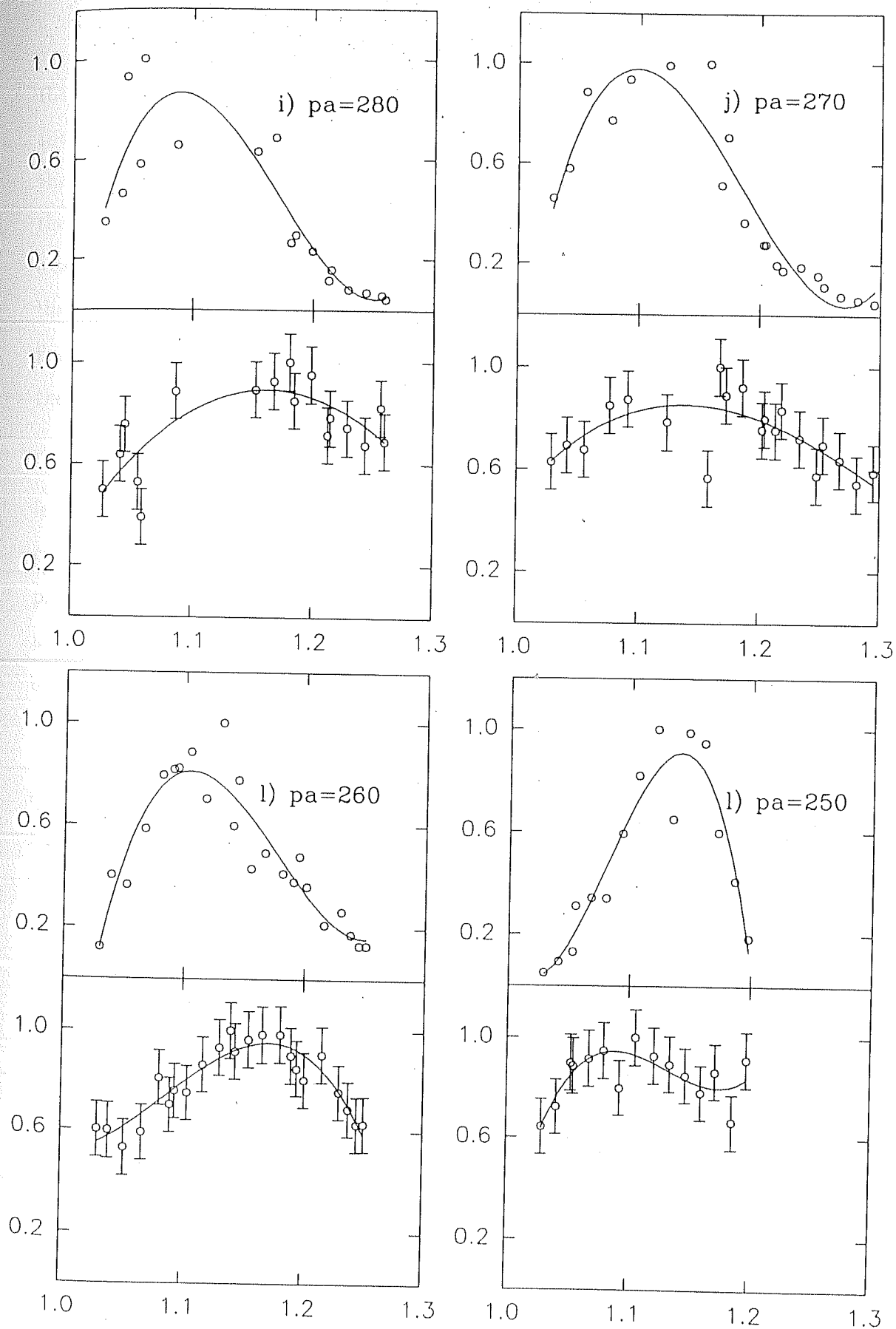
the kinetic temperature in the ambient medium and in the coronal loops are different, the line intensity and the wing intensity may show dissimilar intensity variations along the coronal heights. It is well known that the presence of strong magnetic fields in the coronal active regions have a 'blanketing effect' on the flux tubes ie it allow the existence of thermally isolated coronal loops (Priest 1984). It is interesting to note that the covariation of wing intensity and line intensity breaks down in the strong field regions such as in streamers and active regions where the possibility of finding thermally isolated loop structures exists.

It may also be seen from Figure 3.4 that the variation of wing intensities is strikingly different in different position angles while line intensities show more correlation amongst them. One possible inference is that the similar variation of the physical conditions with coronal heights existing in the ambient medium. In coronal loops, the observation imply that the variation of kinetic temperature and electron density is quiet different throughout the corona.

No appreciable wing intensities are seen in the 1983 interferogram fringes. Line intensity itself is very weak in 1983 corona and the emission recorded was restricted to only a few pockets. Even in regions where fairly strong emission was recorded, the contrast remained high. It is inferred that fast moving discrete components are either absent or weak in the 1983 corona in comparison with the 1980 corona. The above discussion, though only qualitative in nature, emphasizes two points, namely the ubiquitous nature of coronal loops and the importance of magnetic field in solar corona.

Chapter 4

Velocity fields in the Solar Corona

Theoretical developments on corona showed a marked improvement in the past three decades with various proposed mechanisms explaining the diversified coronal phenomena. With the advent of space observations, a good data base is now available on the chromosphere-corona transition region. This is also true about the outer solar atmosphere through the solar wind observations. However, there are only a few attempts on the observational aspects of the inner solar corona. One of the inherent difficulties in this regard is due to the faintness of the visible coronal emission lines. This being the background, our group at the Physical Research Laboratory conducted two successive eclipse expeditions in 1980 and 1983 which resulted in obtaining a wealth of information on the coronal kinematics and photometry. The two expeditions covered two phases of solar activity, one at a solar maximum epoch and the other at a declining epoch, hence provided a good opportunity to compare the kinematical aspects of corona at the two phases. The earlier analysis emphasized on the temperature distribution in the solar maximum corona (Chandrasekhar 1982,

Desai & Chandrasekhar 1983). Large dispersion velocities with variations in position angles were also reported by them (Desai et al., 1982). In the present study, more emphasis is given on the kinematical aspects of corona, particularly the velocity of mass motions. The azimuthal variations of the velocity fields were stressed in the analysis as they arise from the magnetic field structure in the corona. The coronal changes associated with the solar cycle variations were studied which may contribute to the understanding of magnetic field's control of coronal properties.

This chapter deals with the velocity fields in the solar corona. Velocity fields are derived from the emission line profiles of the green coronal line at 5303 Å . The observations and data reduction techniques are described in ChapterII. The individual line profiles carry three kinds of informations on the velocity of the observed medium; i) the Doppler shift of the line peak gives the gross motions of the medium, ii) the halfwidth of the line gives the turbulent motions in the medium in addition to the thermal motions and iii) the structures in the profile tell about the discrete motions along the line of sight (Billings 1966). Section 4.1 describes the gross average motions in the solar corona, from the behaviour of the square of the fringe radius with the fringe number or 'R^2 versus i' analysis of the Fabry-Pérot fringes. Most of the line profiles of 1980 eclipse interferograms have signatures of multicomponents. When the profiles show clear signatures of multicomponents, a multi-Gaussian least square fit has been carried out to get the details of the individual components. The details of this method with illustrative examples are given in section 4.2. In section 4.3, a simple model of the coronal green line has been developed. The effects of mass motions in the corona, presumably arising from the plasma motions inside the flux tubes, were calculated theoretically, taking into account the various flux tube characteristics. The results from the earlier sections and their possible implication to coronal physics are discussed in the final section. The results for the 1983 observations are mentioned in

each sections, along with the 1980 results.

4.1   Line Profile Studies-Gross Behavior

About 750 line profiles from about 120 scans of both 1980 and 1983 observations could be obtained for the detailed study. Typical examples of intensity profiles in a single scan are shown in Figure 3.3 of chapterIII. The scan directions are not radially outwards from the solar centre, but from the fringe center which is slightly displaced with respect to the solar centre. The position angle coverage of the fringes considered for the present analysis is about 230° which includes the east and west active regions for the 1980 observations, while that of 1983 observation is only about 30°, near the west. A close examination of the line profiles reveals many interesting features. The line profiles have, in general, multi-Gaussian shapes. One striking difference between the line profiles of the two epochs is the presence of strong multicomponents in the 1980 profiles. The line profiles from the quiet and polar region generally show signatures of two or three components, one main component and one or two weak components which are well above the background. In some cases, it was possible to trace the same velocity component in the nearby fringes. The active region profiles show presence of three or more components; strength of these components being such that often, it is not possible to decide which is the main component. Fringe splitting is seen in some of the cases (Chandrasekhar 1982). The occurrence of fringe splitting is always associated with either the east or the west active regions. Line profiles belonging to the quiet and polar regions do not show any morphological difference except that the subsidiary components in the quiet region are sometimes stronger than that of the polar regions. The 1983 line profiles were found to broader, with

77

weak signatures of multicomponents.

The average motion in a direction can be studied from an examination of the radii of the individual fringes in that direction. This follows from the interference condition in the FP etalon.

$$2\mu t \cos\theta = n\lambda \tag{4.1}$$

where n is the order number. For small θ, one may write,

$$R^2 = 2F^2 - \frac{F^2\lambda}{\mu t}n \tag{4.2}$$

For any two adjacent fringes, the difference

$$R_{i+1}^2 - R_i^2 = \frac{F^2\lambda}{\mu t} \tag{4.3}$$

will be a constant. The deviation from the constancy indicates the presence of Doppler velocity at either one or both of the points. For a system of fringes for which θ remains small,

$$R_i^2 = c + \frac{F^2\lambda}{\mu t}i \tag{4.4}$$

where c is a constant and i is the fringe number. Hence a plot of R_i^2 versus i will be a straight line with $\dfrac{F^2\lambda}{\mu t}$, being the slope.

The Doppler velocities associated the fringe peaks can be obtained by comparing the coronal interferogram with the calibration frame. The value of the slope corresponding to the unshifted line as well as the error involved in the measurement can be calculated from the 'R^2 versus i analysis' of the calibration fringes. Since the calibration interferogram was taken in the mercury green line at 5461 Å , the value of the slope thus derived has to be corrected for the observed wavelength. The slope corresponding to the unshifted line was then compared with the slopes derived from the individual scans of the interferogram. Each scan consisted of about seven fringes

78

on an average. Fringe peaks were identified on each scan and their squares were then fitted with a straight line against the fringe number. R^2 versus i plots for typical directions in the calibration as well as in the interferograms are shown in Figure 4.1. The slope derived from the calibration fringes is found to be $53 \times 10^5 \mu m^2$ with a standard deviation of $1 \times 10^5 \mu m^2$. The error in measurement in terms of velocity is found to be ± 2 km s^{-1}, as found from the standard deviation in the fit. The value of the slope and deviation measured from the 1983 calibration interferogram also had same values. It was found that the mean velocity associated with the 1980 interferogram fringe peaks is about -5 km s^{-1}, with a large standard deviation, about ± 5 km s^{-1}. The corresponding values for the 1983 interferogram were 0 km s^{-1} and ± 2.9 km s^{-1}

There are two additional sources of uncertainty in dealing with the coronal interferograms as compared to the calibration interferograms. The first one is associated with the error involved in the fringe centre determination which may lead to an error in the position of fringe radii. The second source of error is due to the inherent broadness of the coronal emission line profiles. In the case of actual interferogram, fringe centre could not be exactly determined, due to the presence of Doppler shifts in the fringes which may displace it from the actual circular shape. The error has been minimized in the present analysis, by considering the fringe maxima coordinates uniformly from all over the interferogram. The fact that the two separate interferograms of 1980 observation viz. the 30 sec exposure frame and the 10 sec exposure frame, gave the same values of slope and standard deviation within the error limits, testifies the above conclusion. The broadness of the coronal line profiles which may allow a random displacement of the fringe maximum point, was minimized through the pixel averaging during the data reduction. The error associated with the random displacement of the fringe maximum point can also be reduced by dealing with the
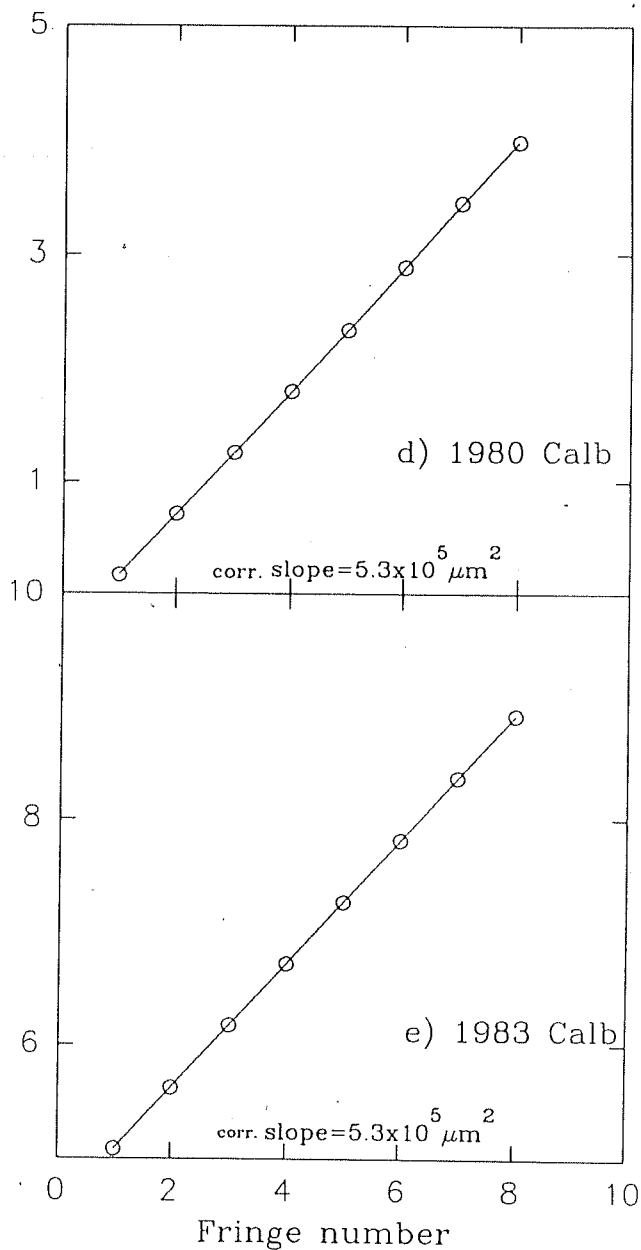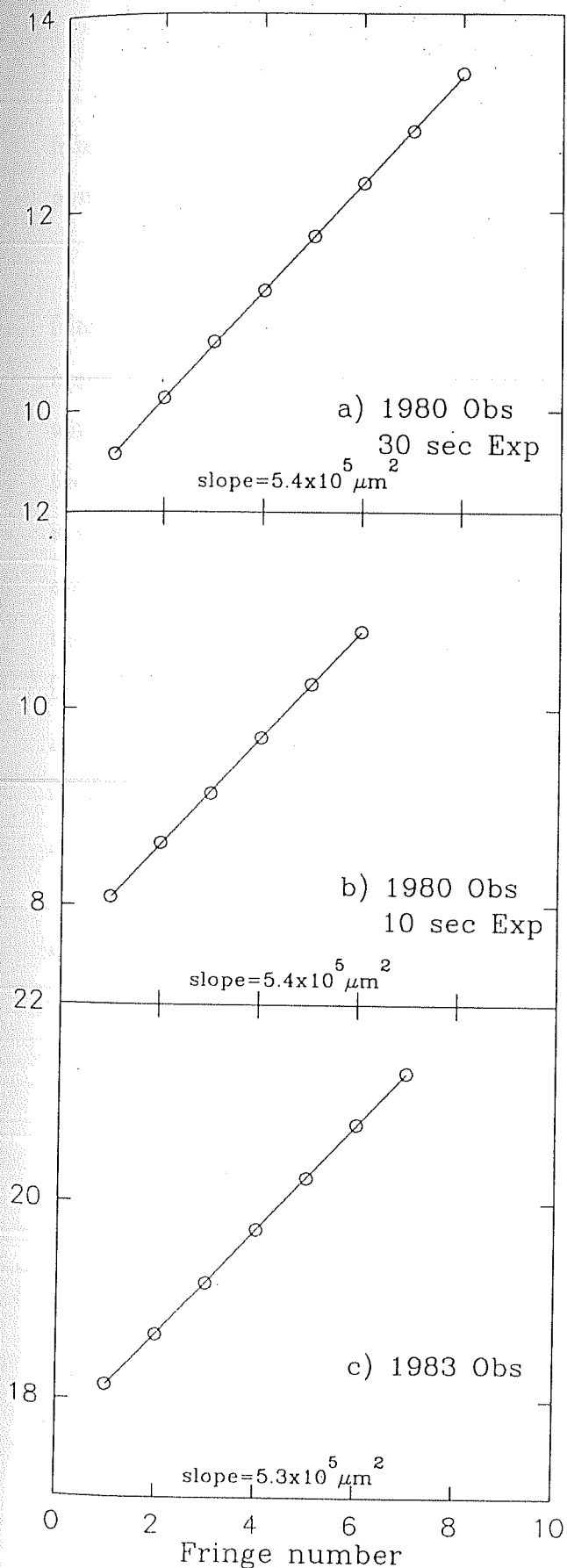
Fig. 4.1   Fringe radii versus fringe number for the interferogram fringes; circles denote the observed points; solid line represents a straight line fit; slope of the straight line fit is mentioned in each plot.

fringe centroids rather than with fringe peaks, since the centroids involve all the data points in the fringe, thus reducing the uncertainty of the fringe peak position.

One immediate conclusion from the above analysis was that for the 1980 fringes, the main component is on an average shifted by about -5 km s^{-1} ; this imply that the subsidiary components have larger velocities associated with them with respect to the main component. The main component should represent mostly the ambient corona and since it was found that it is the least shifted component, it may be concluded that the ambient coronal medium would have velocities on an average -5 km s^{-1} in the solar maximum corona of 1980. This result agrees well with the earlier observations of velocities in the inner corona reporting values less than 10 km s^{-1} (Newkirk 1967). It was also found that most of the subsidiary components are blue shifted with a considerable range of velocities. The large standard deviation found in the R^2 versus i analysis of the 1980 fringes indicates the presence of a non-negligible fraction of fringes, with zero or red-shifted velocities associated with them. The observed 1983 fringes in general have only one component present in them and they do not show any significant velocity in the R^2 versus i analysis. The 1983 epoch represents a declining solar activity period, having an activity of almost half of that of 1980 epoch (Loucif & Koutchmy 1989). It is probable that the ambient corona on an average, may not show any significant velocity, when the activity is low. However, a detailed analysis of about 53 line profiles from the same interferogram by Chandrasekhar et al., (1991) covering two pockets of 5303 emission and a position angle interval of $110°$ showed the presence of more than one component in 21 of them. Out of 31 line profiles obtained from the coronal red line observations, two of them showed evidence of double Gaussian components.

Our analysis indicates that the slopes of R^2 versus i curves for the 1980 fringes

have larger than expected values, with large standard deviation . At this point, it will be interesting to see whether $(R_{i+1}^2 - R_i^2)$ show any radial or azimuthal variations. One added advantage in dealing with the $(R_{i+1}^2 - R_i^2)$ values is that the variations in this quantity could not be affected by the error in the fringe centre. The solar coordinate corresponding to R_{i+1} was found by a coordinate transformation from the interferogram coordinates to the solar coordinates. The values of $(R_{i+1}^2 - R_i^2)$, radial and azimuthal coordinates were found out for about 750 fringes. The values of $(R_{i+1}^2 - R_i^2)$ uniformly distributed over the interferogram at a 10° interval are plotted against coronal radial distance in Figure 4.2. A least square straight line fit is plotted together to see the correlation. The value of correlation coefficient (q) is mentioned at each plot. A statistically significant correlation between the increase in velocity and coronal radial distance can be seen for the 1980 observation. The correlation is insignificant for the 1983 interferogram. In order to make sure that the observed result did not arise from any unnoticed bias in the analysis, $(R_{i+1}^2 - R_i^2)$ values from the calibration interferogram were plotted against the fringe number for the two occasions. The observed correlation coefficients are mentioned, only for comparison. Calibration fringes do not show any correlation as expected, thus ruling out the possibility of any bias in the analysis. A clear positive correlation seen in the 1980 fringes, indicates that the line of sight velocity generally increases with the coronal radial distance. A large scatter in the diagram however, indicates that there is a non-negligible fraction of fringes exist, for which the line of sight velocity either decreases or remains a constant. The 1983 fringes do not show any significant correlation beyond the error limit.

It is worthwhile to see whether the increase in $(R_{i+1}^2 - R_i^2)$ with the coronal radial distance is related with the coronal azimuths. In this analysis, fringe centroids
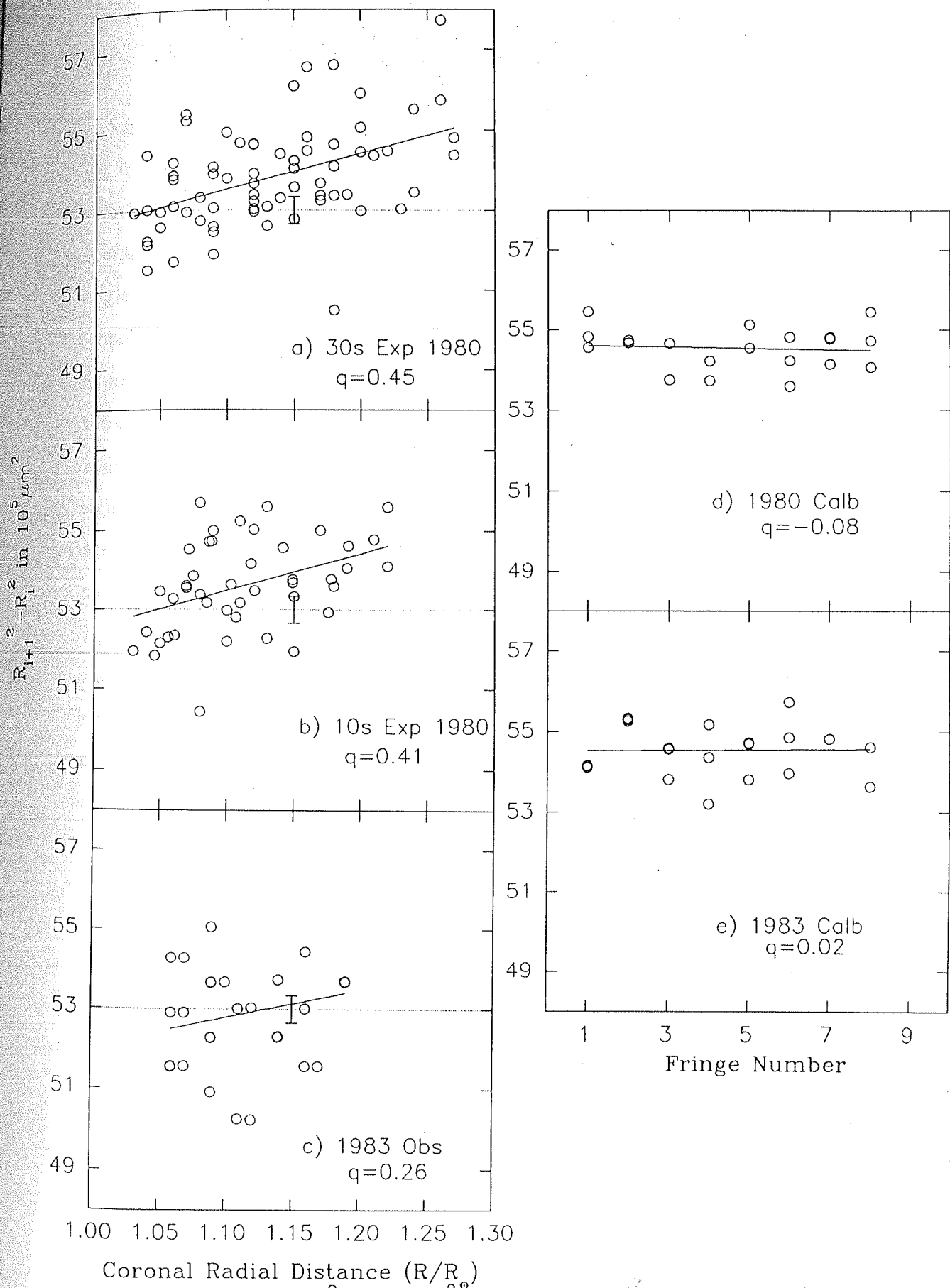
Fig. 4.2 The value of $R^2_{i+1} - R^2_{i^\circ}$ against coronal radial distance plotted for various interferograms. A straight line fit is shown in each plot; q represents the correlation coefficient of the fit.

rather than fringe peaks were used in order to reduce the scatter. $(R_{i+1}^2 - R_i^2)$ values for various fringes were grouped together in an interval of $10°$. The line of sight velocity at each point was calculated according to its deviation from the slope corresponding unshifted line. The Figure 4.3 shows these plots for various coronal position angles. A least square third degree polynomial has been fitted in some of the plots where the correlation was found to be good, to see the behavior very clearly. The expected velocity which corresponds to the slope of the unshifted line, derived from the calibration fringes is plotted as the dotted line along with the measurement error which is about $\pm$ 2 $km\,s^{-1}$. It may be easily seen that the increase in the line of sight velocity found in the inner corona depends very much on the coronal azimuth. Many of the position angles from the polar and quiet regions (pa 10,350,340,330) do not show any correlation between the two. A small correlation is seen in the quiet regions adjacent to the active region (pa 300& 290). Active region (pa 270& 280) shows maximum correlation and thereafter the increase in the line of sight velocity reduces(pa 260& 250). The same quantities derived for the 10s exposure interferogram of the 1980 and the 1983 interferogram are also plotted in Figure 4.3. The azimuthal correlation is not clearly seen in the 1983 interferogram fringes. Some of the position angles (pa 110,100,80) from the eastern active region belonging to the 10s interferogram show a significant increase of line of sight velocity with the coronal radial distance. The results are discussed in more detail in the final section of the chapter.
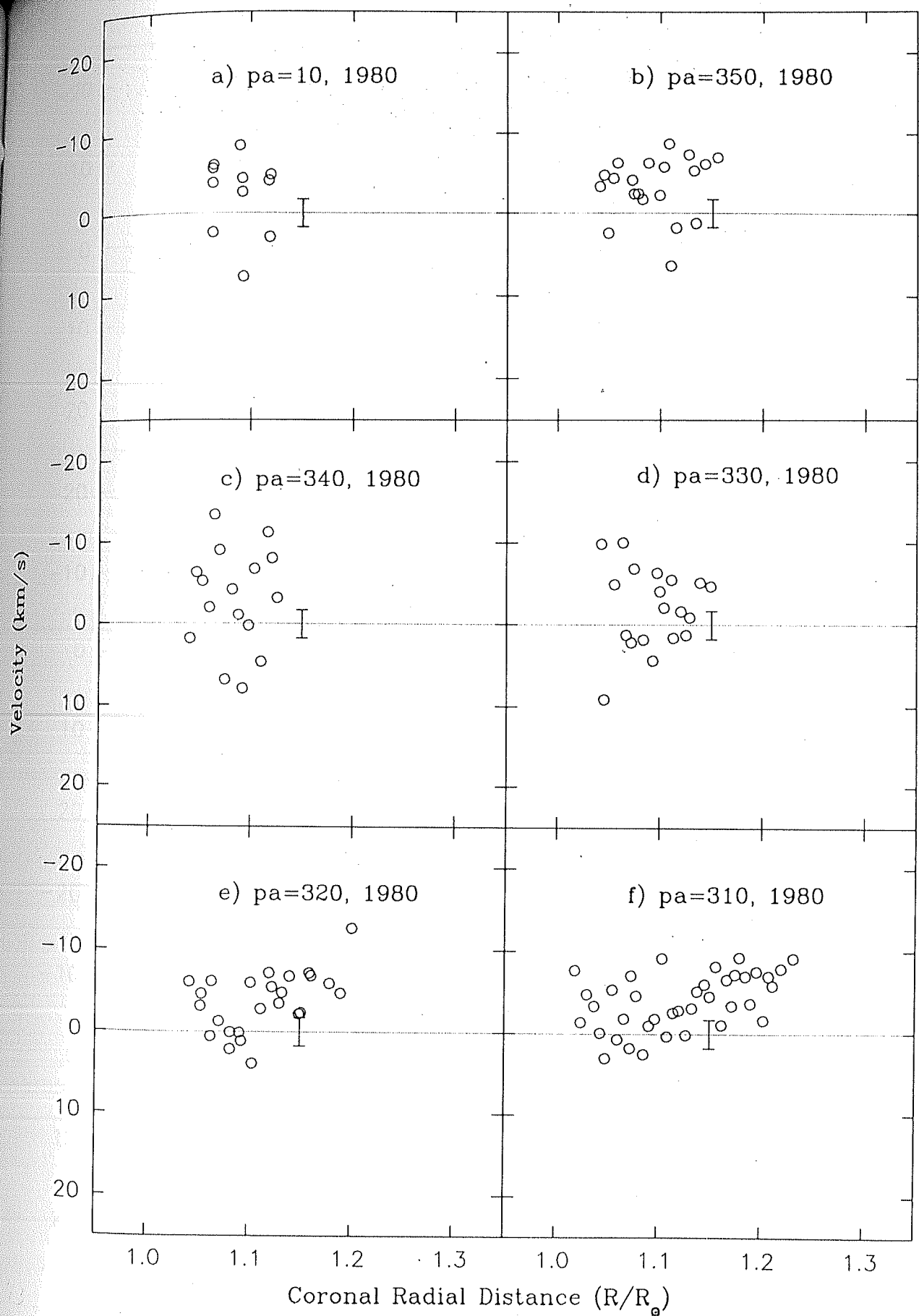
Fig. 4.3   The line of sight velocity against radial distance in various position angles in the corona as derived from the position of the fringe centroids; circles denote the observed points, the horizontal dotted line represents the values corresponding to the calibration fringes; error involved in the measurement is indicated at each plot.

g) pa=300, 1980

h) pa=290, 1980

i) pa=280, 1980

j) pa=270, 1980

k) pa=260, 1980

l) pa=250, 1980

Velocity (km/s)

Coronal Radial Distance (R/R$_\odot$)
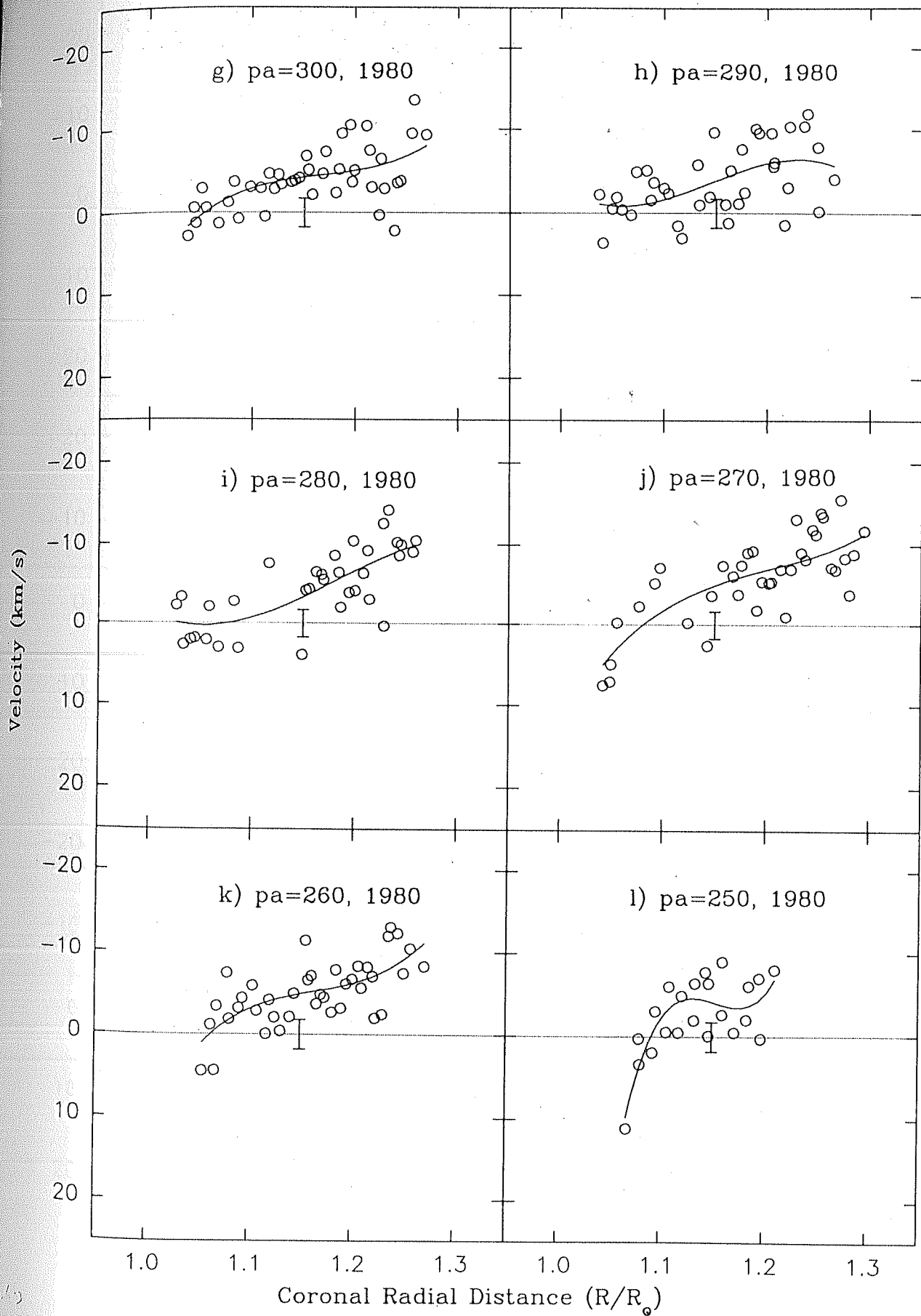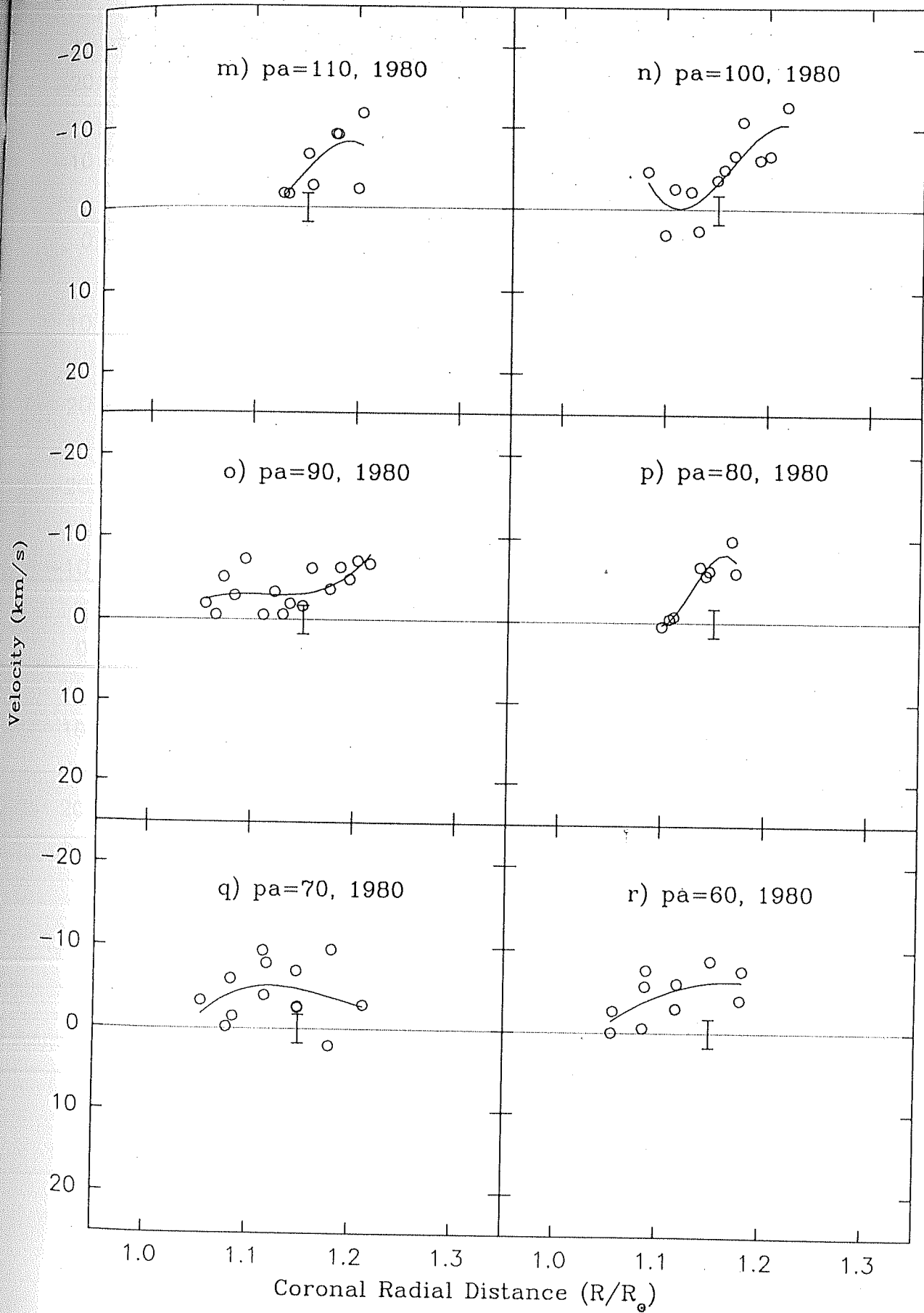
Fig.4.3 continued

Fig. 4.3 continued

87
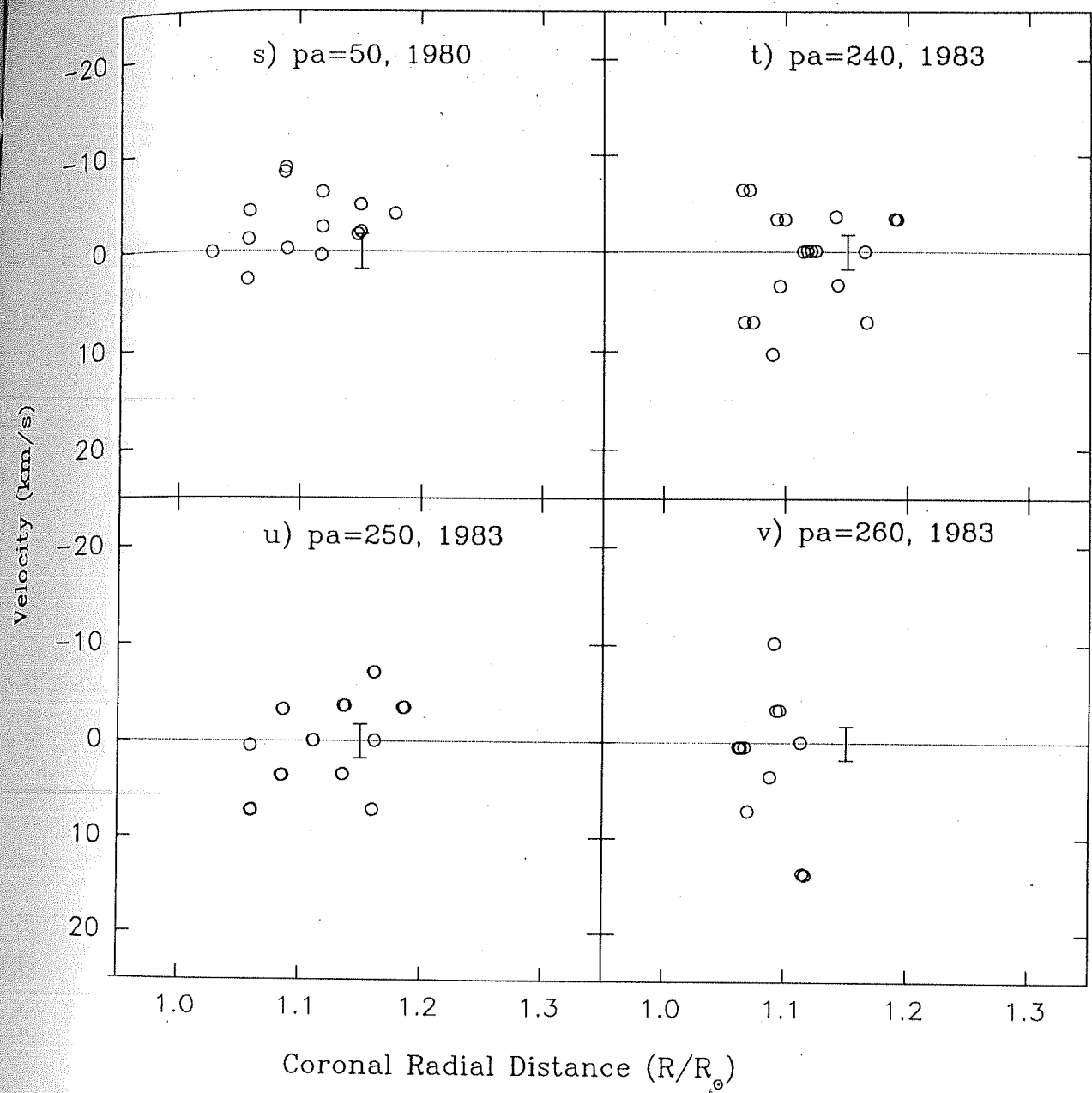
Fig. 4.3 continued

4.2 Line Profile Analysis-A Detailed Study

Majority of the 1980 line profiles showed signatures of either weak or strong components. Line profiles of 1983 showed only weak signatures of multicomponents. When the line profiles showed clear signatures of multicomponents, a least square multi-Gaussian fitting program was employed in some cases. It is possible to know the temperature, velocity and the relative strength of the individual components from such a technique. A computer software (Press et al., 1988) was used to perform this operation. The method adopted is as follows; the given line profile was examined in detail to decide the characteristics of the individual components approximately, namely the wavelength position of components, their halfwidths and relative intensities. These values go as the trial values into the program. The program calculates the χ^2 merit function from the given data points; the best fit parameters are then determined by the minimization of χ^2. Since the model to be fitted is a non-linear model, the minimization has to be carried out through iterations. Given the trial values for the parameters, a procedure that improves the trial solution is adopted. This is repeated until χ^2 stops or effectively stops decreasing. Mathematically, the whole procedure may be represented as follows.

The model to be fitted is

$$y = y(x; a) \tag{4.5}$$

where a's are the parameters which characterize the Gaussians, and are to be determined.

The χ^2 merit function is

$$\chi^2(a) = \sum_{i=1}^{N} \left[\frac{Y_i - Y(x_i; \mathbf{a})}{\sigma_i} \right]^2 \tag{4.6}$$

89

where σ_i is the individual standard deviation.

The gradient of χ^2 with respect to the parameters **a**, which will be zero at χ^2 minimum, has components,

$$\frac{\partial \chi^2}{\partial a_k} = -2 \sum_{i=1}^{N} \frac{[Y_i - y(x_i; \mathbf{a})]}{\sigma_i^2} \frac{\partial y(x_i; \mathbf{a})}{\partial a_k} \quad k = 1, 2, .., M \tag{4.7}$$

$$\frac{\partial^2 \chi^2}{\partial a_k \partial a_l} = 2 \sum_{i=1}^{N} \frac{1}{\sigma_i^2} \left[\frac{\partial y(x_i; \mathbf{a})}{\partial a_k} \frac{\partial y(x_i; \mathbf{a})}{\partial a_l} - [Y_i - y(x_i; \mathbf{a})] \frac{\partial^2 y(x_i; \mathbf{a})}{\partial a_l \partial a_k} \right] \tag{4.8}$$

Defining

$$\beta_k = -\frac{1}{2} \frac{\partial \chi^2}{\partial a_k}, \quad \alpha_{kl} = \frac{1}{2} \frac{\partial^2 \chi^2}{\partial a_k \partial a_l} \tag{4.9}$$

Sufficiently close to minimum, χ^2 function is well approximated by a quadratic form, and the minimizing parameters a_{min} may be written as

$$a_{min} = a_{cur} + D^{-1} \left[-\nabla \chi^2 (a_{cur}) \right] \tag{4.10}$$

where a_{cur}'s represent the current trial parameters. D is an M×M matrix and is given by

$$[\alpha] = \frac{1}{2} D \sum_{l=1}^{M} \alpha_{kl} \, \delta_{kl} = \beta_k \tag{4.11}$$

This set is solved for the increments δa_l, that gets added to the current approximation, giving the next approximation. Thus the iteration is carried out and the final result is obtained when there is no final reduction in χ^2.

It must be mentioned here that the program which was used to separate the components in a given line profile, is a general nonlinear least square fit method and hence obtaining a unique set of parameters that fit the observed profile is impossible. The possibility of getting a good fit depends on the choice of trial values to a certain extent. The program thus becomes quiet time consuming especially if more than two components are present and if the individual components are not well separated.

Nevertheless, reasonably good fits were obtained in a good number of profiles. The following procedure was adopted as a working method in the analysis; i) correctly judging the line profile to decide the trial parameters viz. the width, position and relative velocity of the components ii) judging the fit by eyes and iii) the criteria of standard deviation.

About 20 line profiles were analyzed in the above fashion. Some of the examples of the best fitted data are shown in Figure 4.4. The observed line profile, the best fit and the individual components are shown in the figure. The details of the best fit program are given in Table 5.1. The coronal radial distance, position angle and the details of the individual components are tabulated in different columns. The results of the above exercise are summarized below.

i) The line profiles belonging to the solar maximum corona of 1980 epoch generally show presence of multicomponents. Line profiles in the quiet and polar region, in general, consist of two or three components with a main component and weak subsidiary components. Line profiles in the active region are made up of three or more components with two of the components having comparable intensity.

ii) The main component found in the quiet and polar regions (Figure 4.4, cases 7–12 and Table 4.1) is least shifted in velocity and it has the characteristics of ambient coronal medium. Subsidiary components are associated with large velocities with magnitudes upto 73 $km\,s^{-1}$. The widths of the subsidiary components are either equal to or more than that of the main component.

iii) The subsidiary components in the active region (Figure 4.4, cases 1–6 and Table 4.1) have velocities in the range 10–60 $km\,s^{-1}$, with respect to the main component. The half widths of the stronger components were found to be very low
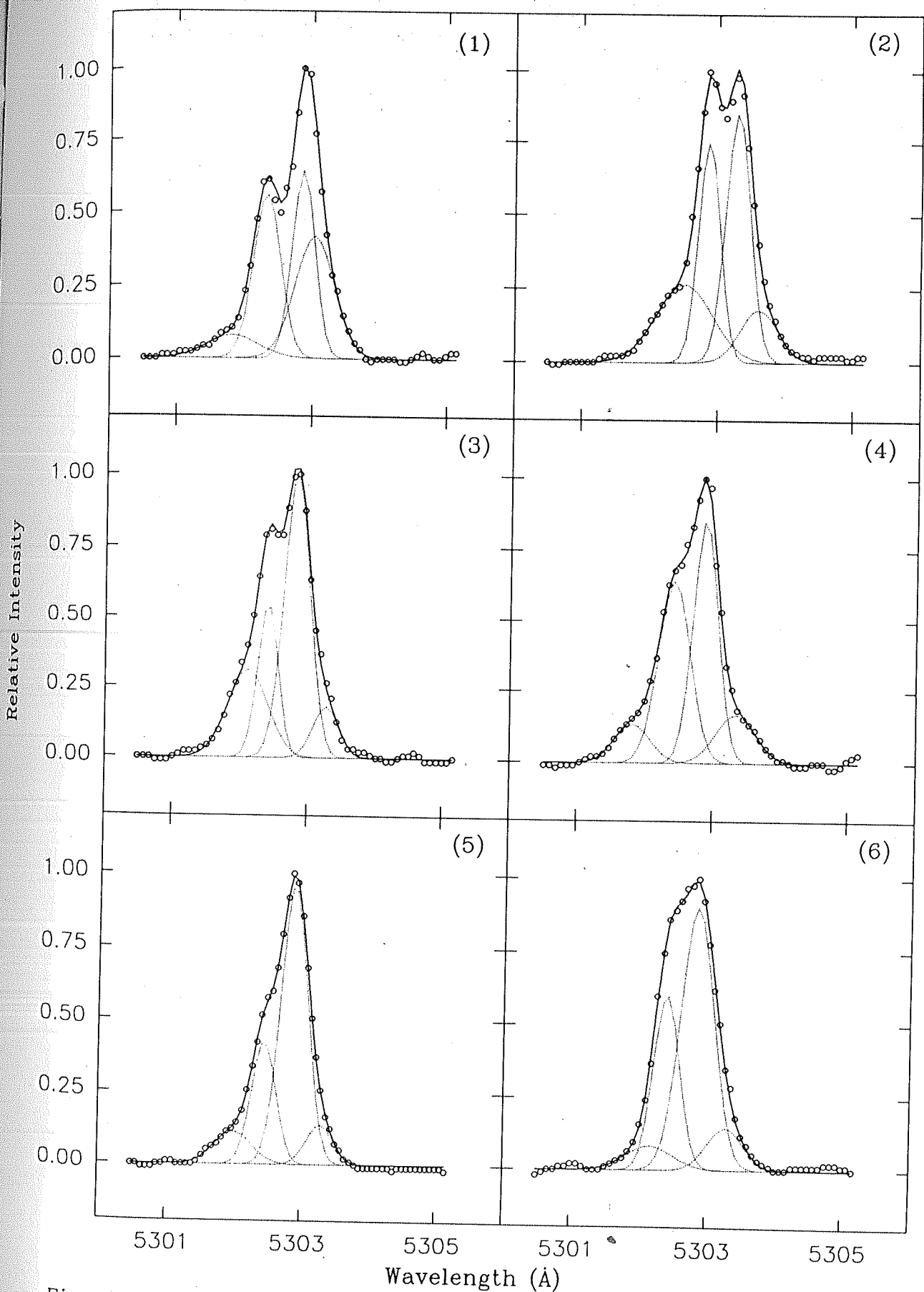
Fig. 4.4 Multi-Gaussian fit to the observed line profiles; circles denote the observed data points, solid line denotes the best fit curve and the dotted curves represent the individual Gaussian components. Details of the fit are given in Table 4.1.
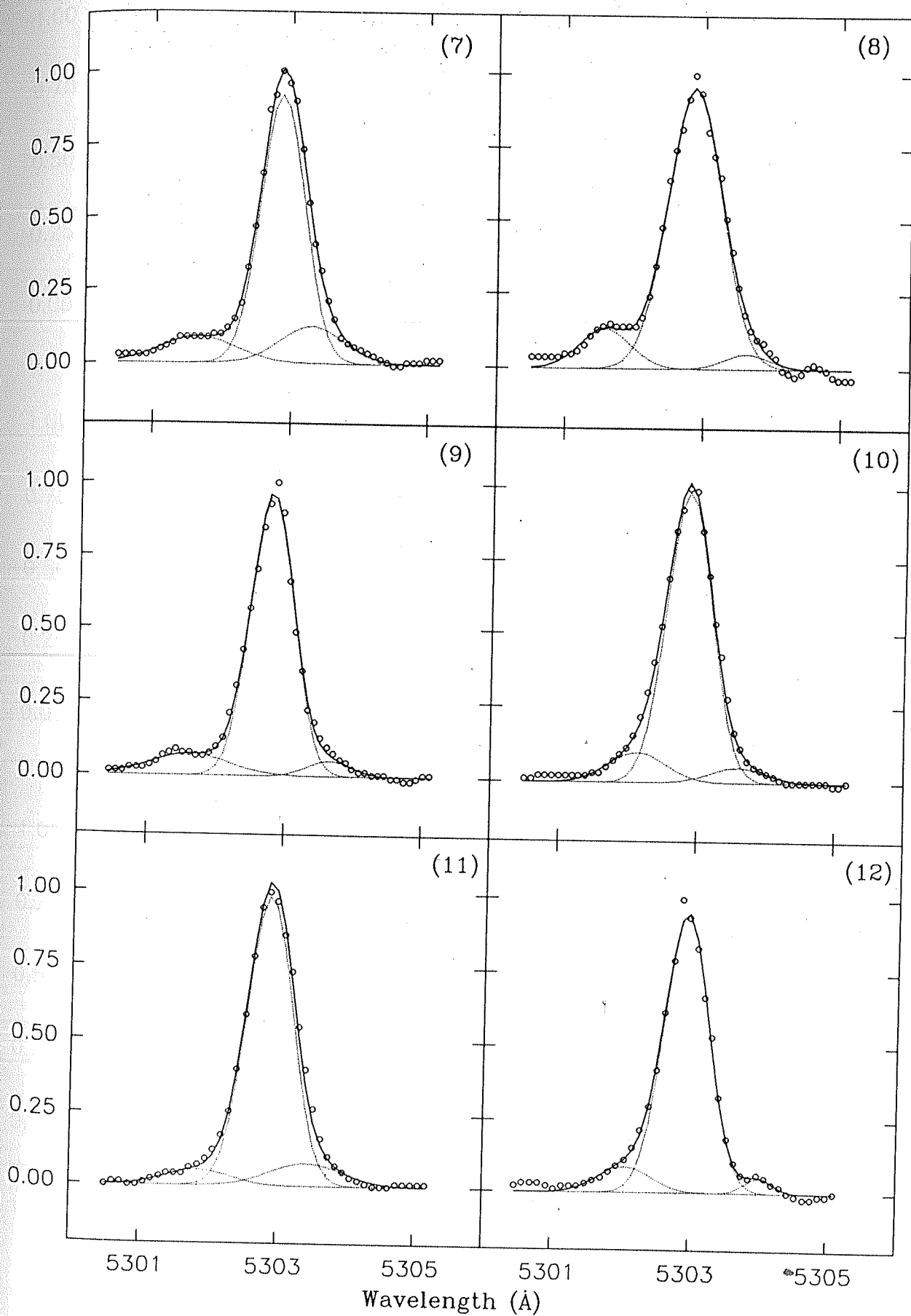
Fig. 4.4 continued
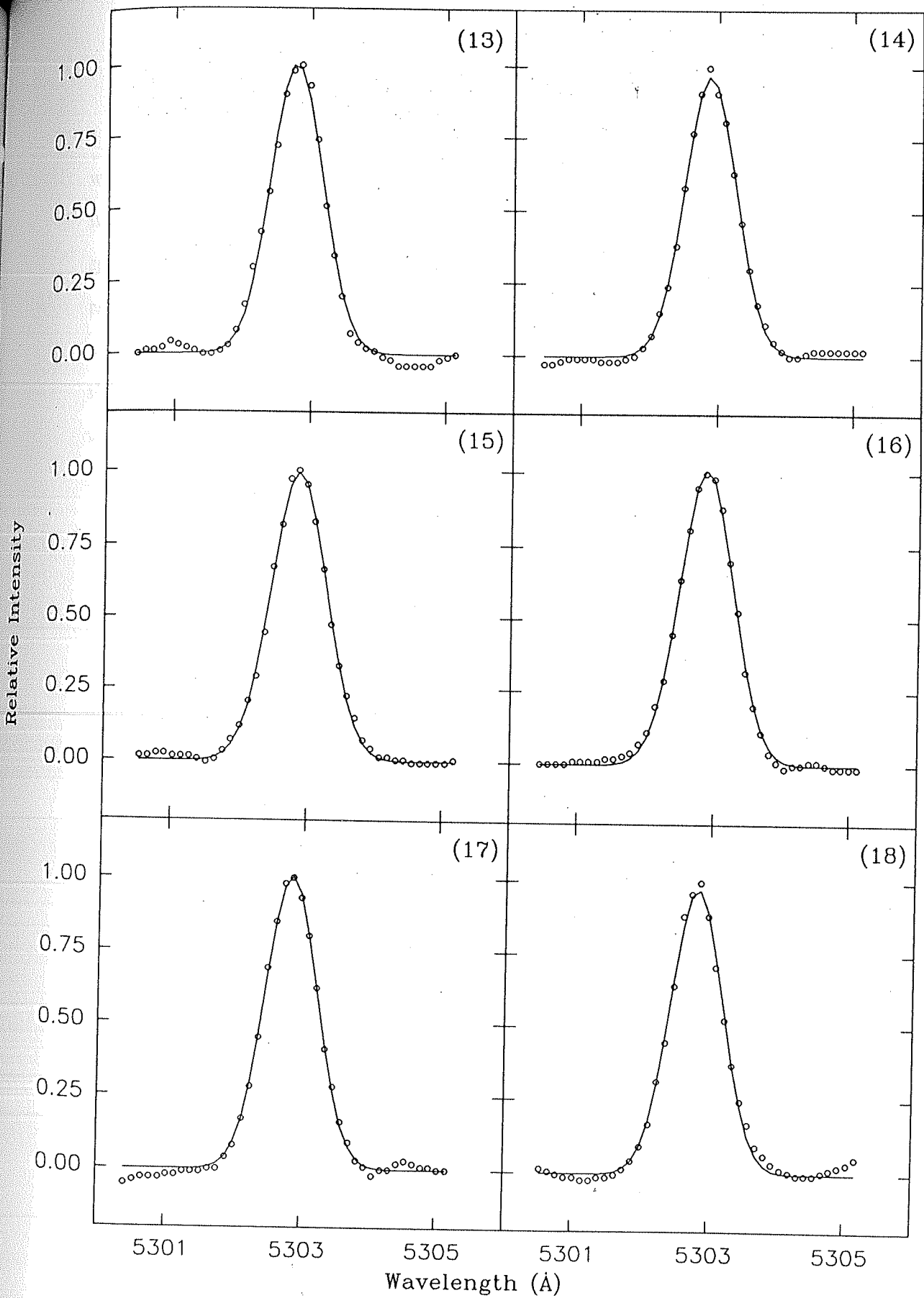
Fig. 4.4 continued

which may correspond to a temperature less than 1 million K. The main component itself was found to have a temperature of the same order. It is more probable that in such cases, the main component could be representing the discrete coronal structures rather than the ambient medium. In the multi-Gaussian fit, we find one subsidiary component in the blue region, which is more or less at the coronal temperature and this component may be then representing the ambient coronal medium. However, in the absence of more such examples, it may be difficult to arrive at a general conclusion. Suffice to say that low temperature loop plasma exists in the active region corona, a result which agrees with the findings of Foukal (1975, 1976) and Jordan (1975).

iv) The line profiles in the selected region of the 1983 interferogram were in general found to contain only one very dominant component (Figure 4.4, cases 13–18 and Table 4.1). The widths of single Gaussian components were found to be high, which if directly converted into temperature, would give values of 2.9 million K. Chandrasekhar et al., (1991) find the turbulent velocity to be very high ($\sim$18 km s^{-1}) at these locations.

4.3 Modelling of the Coronal Green Line Profile

The presence of flux tubes in the corona is now well established through various observations (Athay et al., 1983b, Priest 1984, Kopp et al., 1985). The role of flux tubes in coronal dynamics, energy balance and heating is currently a subject of active research. Our results support this view very strongly. The presence of excess intensity in the wing region of Fabry-Pérot line profiles and their behavior vis-a-vis the ambient corona, the increase of line of sight velocity deduced from the $(R_{i+1}^2 - R_i^2)$ values of the interferogram fringes and the actual finding of line splitting and the signatures

Table 4.1: Details of the multi-Gaussian fit to the observed profiles; columns denote case number, position angle, coronal radial distance in units of $R/R_\odot$, relative intensity, velocity in $km\,s^{-1}$, half width in Å of the different components, χ^2, and standard deviation respectively

no	pa	coronal radial distance	components												χ^2	st dv
			1			2			3			4				
			Int	Vel	Hw	Int	Vel	Hw	Int	Vel	Hw	Int	Vel	Hw		
1	270.9	1.22	0.08	−58.8	0.89	0.56	−30.5	0.47	0.64	0	0.39	0.42	9.6	0.68	0.014	0.016
2	268.9	1.20	0.26	−20.4	0.97	0.75	0	0.38	0.85	23.8	0.43	0.18	41.9	0.66	0.018	0.018
3	267.7	1.21	0.31	−40.2	0.69	0.55	−23.8	0.35	1.00	0	0.45	0.18	25.5	0.45	0.011	0.013
4	268.6	1.25	0.13	−60.5	0.61	0.64	−26.0	0.54	0.86	0	0.43	0.17	25.5	0.69	0.011	0.014
5	262.3	1.09	0.11	−50.4	0.65	0.42	−24.9	0.42	0.96	0	0.46	0.14	22.1	0.46	0.005	0.008
6	266.6	1.23	0.08	−39.0	0.82	0.60	−25.5	0.44	0.90	0	0.57	0.14	24.3	0.62	0.010	0.013
7	306.9	1.06	0.09	−68.5	1.27	0.92	0	0.74	0.12	24.9	1.08				0.007	0.012
8	302.3	1.03	0.13	−73.0	0.86	0.95	0	0.74	0.05	43.6	0.74				0.023	0.021
9	303.0	1.06	0.07	−67.3	1.35	0.96	0	0.73	0.05	48.7	0.76				0.018	0.018
10	303.7	1.09	0.10	−41.3	0.97	0.99	0	0.76	0.05	41.3	0.95				0.010	0.014
11	6.4	1.06	0.06	−56.6	1.02	0.88	0	0.78	0.16	18.1	1.06				0.004	0.010
12	6.4	1.09	0.06	−49.2	0.90	0.95	0	0.75	0.05	61.1	0.48				0.015	0.019
13	245.3	1.06	1.00	0	0.90										0.027	0.026
14	249.6	1.06	0.97	0	0.88										0.010	0.016
15	249.7	1.09	0.99	0	0.96										0.008	0.015
16	251.8	1.06	1.01	0	0.93										0.006	0.013
17	251.8	1.09	1.01	0	0.90										0.013	0.018
18	253.1	1.09	0.98	0	0.89										0.018	0.022

of weaker components in the line profiles, all support the above argument. Under these circumstances it was decided to model a green coronal line profile theoretically, considering the physical conditions in corona with the presence of coronal loops as an added parameter, to see the effects of loop motion on the line profiles. A detailed modelling of the green line profile considering the effect of expansion of the corona could be seen in Peraiah and Varghese (1989).

The resulting line profile was calculated when the line of sight encounters a coronal loop in an otherwise spherically symmetric corona. The calculation was done for a simple situation when the line of sight encounters only one loop which is oriented along the line of sight and having a flow velocity presumed to be arising from a siphon flow along the loop. Some of the physical quantities associated with the loop such as electron density inside the loop and flow velocity were varied in the observed range and the resulting profiles were calculated. It was found that the features in the observed line profiles could be reproduced with such a calculation.

The line intensity calculations are described in ChapterV. Physical characteristics of quiet corona are also described there. Here we describe only the relevant steps. The calculations were performed for quiet corona having an isothermal temperature of 2 million degree K. Coronal loop parameters were taken from Priest(1984). The coronal green line intensity may be given by

$$I_l = \frac{h\nu}{4\pi} n_j A_{ji} \qquad (4.12)$$

where n_j is the number density of the excited level obtained from the condition of statistical equilibrium between the two levels(Billing 1966, Gibson 1973).

$$n_j(A_{ji}) = n_i(R_{ij} + n_e C_{ij}) \qquad (4.13)$$

The line profile was calculated by finding out the intensities in the nearby wavelengths,

assuming a Gaussian shape for the profile. The line of sight integration was performed within the limits $-2R_\odot$ to $+2R_\odot$. The re-absorption of the emitted intensity in the solar atmosphere was neglected. This is justified if we consider the optical depth in the corona which is 10^{-4} (Van de Hulst 1953).

In the next stage, we have considered a single coronal loop with a semi-circular shape and an orientation along the line of sight. The geometry of the calculation is shown in Figure 4.5. The loop characteristics are given below.

$$\text{Loop length(2L)} : 2\times10^5 \text{ km s}^{-1}$$
$$\text{Loop diameter} : 2\times10^4 \text{ km s}^{-1}$$
$$\text{Loop summit} : 1.10 \text{ R}_\odot$$
$$\text{Loop electron density} : 0.5\text{--}2\times10^9 \text{cm}^{-3}$$
$$\text{Electron temperature inside the loop} : 1\text{--}3\times10^6 \text{ K}$$
$$\text{Flow velocity at the loop summit} : 0 \text{ to } -60 \text{ km s}^{-1}$$
$$\text{(Priest, 1984).}$$

The assumed loop length is larger by a factor two than that given by Priest (1984). Loops of the assumed length are very well seen in coronal photographs (Rusin & Rybansky 1983); Skylab EUV observations reveal the existence of loops of length upto one solar radius (Habbal et al., 1985). Flow velocities are all taken as negative, because we see mostly blue shifted velocities in the corona. Flow velocities in the opposite direction will produce an asymmetry of exactly the same magnitude on the higher wavelength side.

The resulting line profiles were calculated at a radial distance 1.10 $R_\odot$. The various cases are shown in Figure 4.6. Details of the calculations may be seen in Table 4.2. It is clear from the above calculation that the presence of loops in the
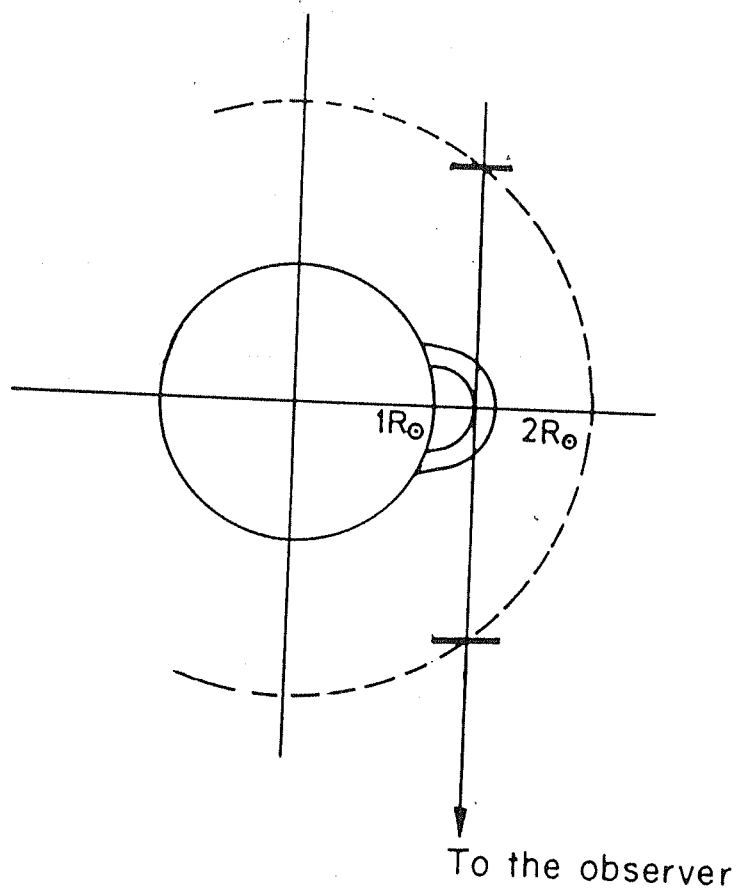
To the observer

Fig. 4.5   Geometry of the calculation used in line profile modelling.

corona appreciably changes the line profiles from their single Gaussian shapes. In Figure 4.6 the first case represents the line profile which originates from the spherically symmetric corona with ambient temperature ~2 million K; the other cases (Figure 4.6 cases 2–12) represent situations when the line of sight encounters a coronal loop with different characteristics. When the flow velocities are low (~ 20 km s^{-1}) line profiles are only mildly affected by their presence; the only apparent effect is to change the line peak to shorter wavelengths (Figure 4.6, case 2). The observed -5 km s^{-1} average velocity associated with the main peaks seen in the 1980 interferogram fringes could be due to a similar situation; the presence of a large number of discrete components with velocities ~ -5 km s^{-1}, shift the line profile to shorter wavelength, without changing the shape very much. One puzzling observation described in the earlier section is the presence of stronger components with narrow widths seen in the active regions. This could be due to the existence of coronal loops in the active region with low kinetic temperatures, a somewhat similar situation we encounter in the case 8 of Figure 4.6. It may also be seen that when the orientation of loop is appropriate, it may even surpass the ambient coronal medium in intensity.

However, it may be seen that the model overemphasizes the loop characteristics because of the assumption that the line of sight passes through the loop at the plane of sky; the maximum contribution to the line intensity arises from here. The actual situation in corona can be much more complicated. A large number of coronal loops with varying size, flow velocity, electron density, temperature and turbulence and different orientations with respect to the observer, may affect the observed line profile. Also, we did not take into account the possible acceleration of coronal material along the loops. Nevertheless, the model is successful in asserting two things; i) loop flows in the corona give rise to structures in the emission line profile and ii) the features of the line profiles could be explained by similar calculations.

Table 4.2: Details of the theoretical calculation of line profiles shown in Figure 4.6; columns denote the case number, loop electron density, loop kinetic temperature, the flow velocity of the loop plasma and the half width of the calculated profile, respectively

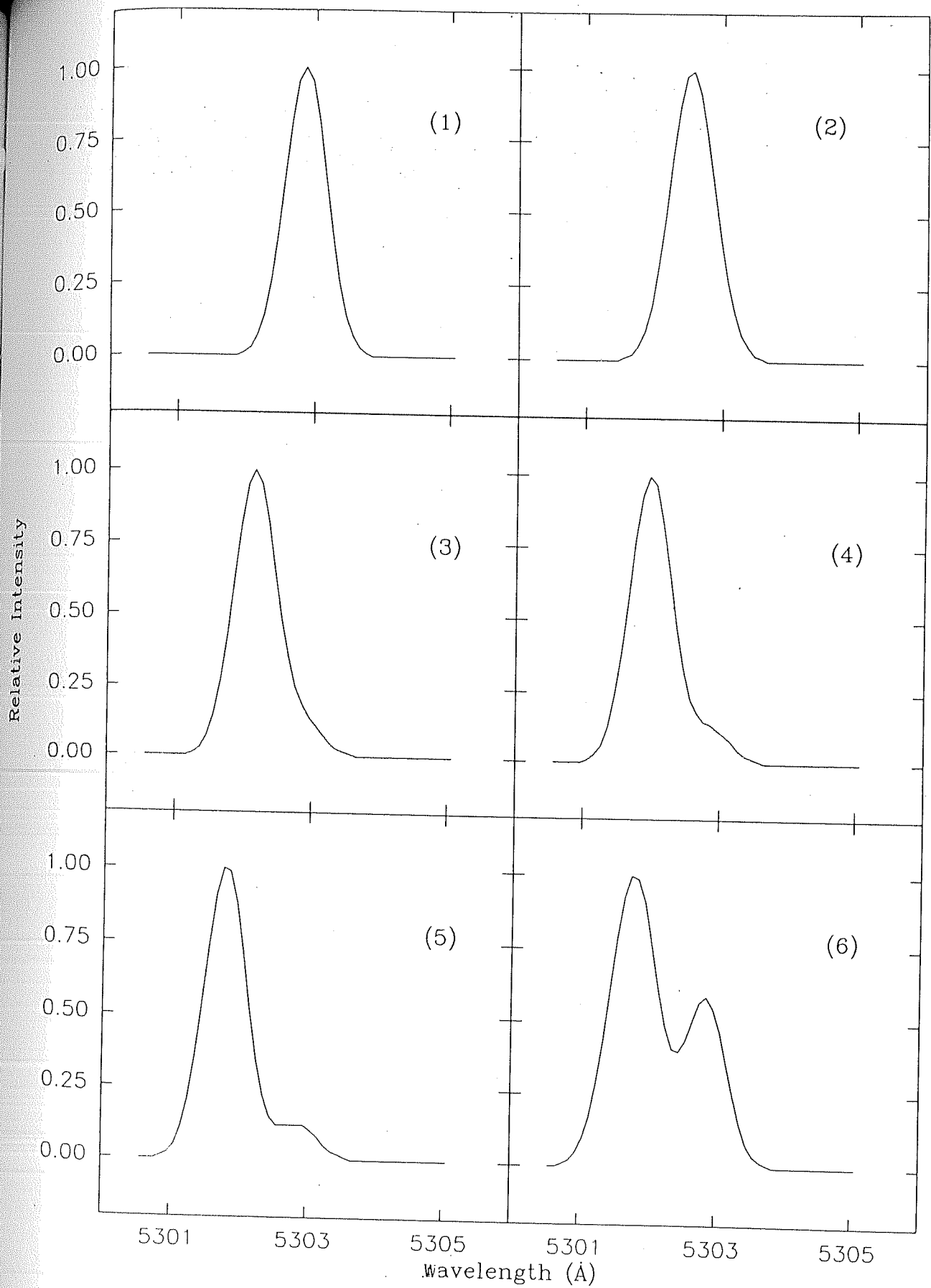| no	Loop characteristics			Hw
	$n_e(10^8)\ cm^{-3}$	Temp(10^6)K	v km s^{-1}	Å
1	–	–	–	0.72
2	1	2	−20	0.74
3	1	2	−40	0.75
4	1	2	−50	0.74
5	1	2	−60	0.73
6	1	2.5	−60	1.62
7	1	1.0	−40	0.72
8	1	1.5	−40	0.68
9	1	2.5	−40	1.27
10	1	3	−40	0.94
11	0.5	2	−40	1.10
12	2	2	−40	0.72

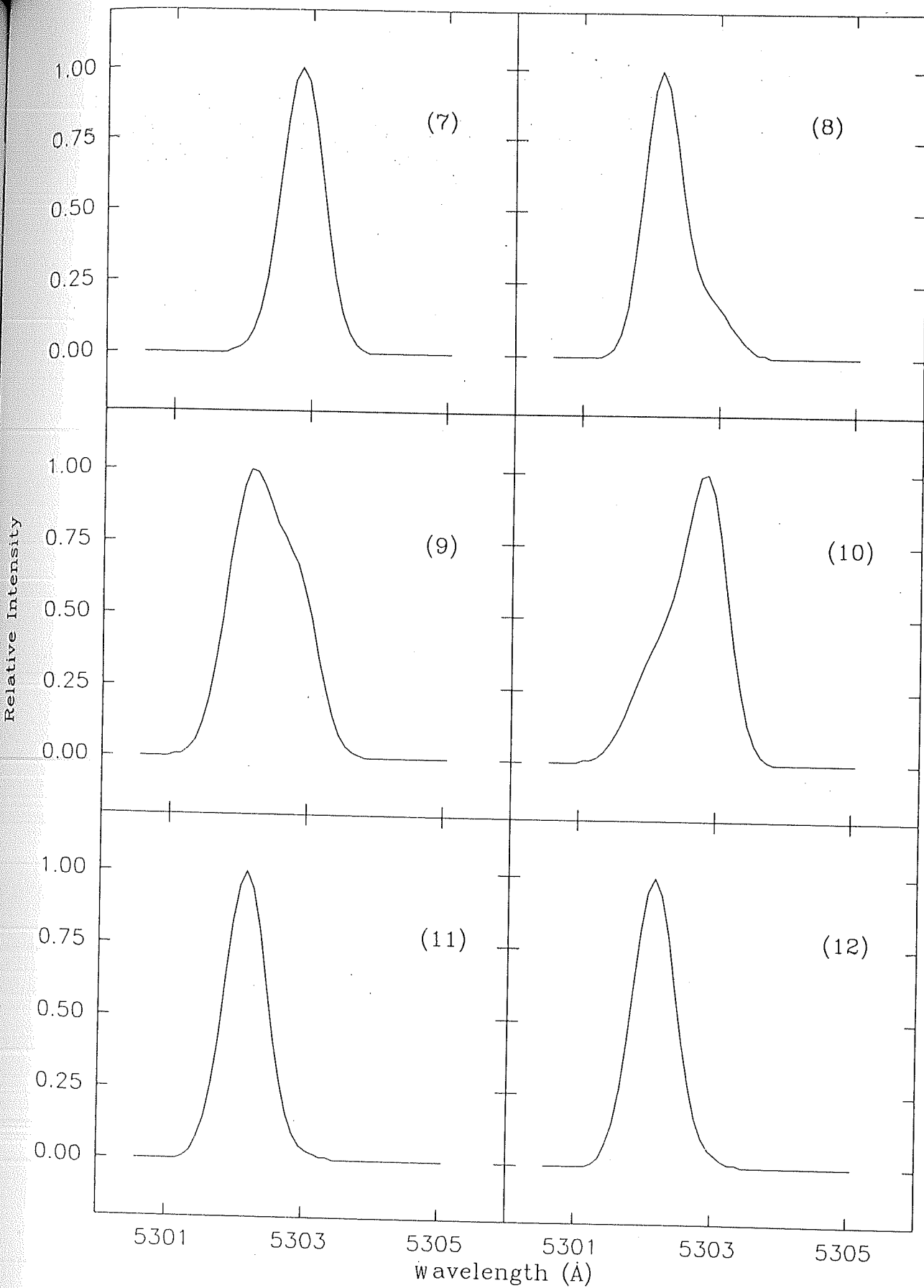Fig. 4.6 Line profiles obtained from the model calculations.

Fig. 4.6 continued

4.4 Discussion

It is generally known that the inner solar corona is static with no macroscopic motions greater than a few $km\,s^{-1}$ (Newkirk 1967). About 15 recent interferometric and multislit investigations of coronal emission lines have not shown evidence of moving elements (Delone et al., 1988). On the other hand, there exists a class of observations which reported large scale motions in the corona (Harvey & Livingston 1981, Chandrasekhar 1982, Desai et al., 1982, Singh et al., 1982, Delone et al., 1988, Chandrasekhar et al., 1991). The subject of mass motions in corona is thus, remains controversial. The occurrence of velocity field and its relation with solar activity is also not completely understood. Thus our studies of the comparison of velocity fields pertaining to two phases of solar activity become quite relevant.

It is clear from the above observations that mass motions do exist in a solar maximum corona. The velocity field appears to be considerably complex at solar maximum periods. The Important results described in the earlier sections can be summarized as follows.

1. Line profiles of the 1980 corona, in general, show evidence of strong multicomponents. Majority of the line profiles derived from the 1983 observation do not show evidence of multicomponents.

2. Large excess of blue shifted components in the 1980 coronal line profiles.

3. The average velocity associated with the main component of the line profiles from the solar maximum corona is -5 ± 5 $km\,s^{-1}$ with a measurement error of ± 2 $km\,s^{-1}$. In the declining activity phase of 1983, it is 0 ± 2.9 $km\,s^{-1}$ with the same error.

4. Increasing line of sight velocity with coronal radial distance mainly associated with the active regions of solar maximum corona.

5. Line splitting in the active regions in the 1980 solar maximum corona.

6. Line profiles from the active regions could be best fitted with three or more Gaussians; presence of strong components with generally low velocities and half widths.

7. Line profiles belonging to the quiet and polar regions of the 1980 corona show two or more components with the main component representing the ambient corona. Subsidiary components are generally weak and their line widths are equal to or more than that of the main component; the velocity of the subsidiary components are very large (upto ~ 73 km s^{-1}).

8. Line profiles from the 1983 observations are mostly, best described by single Gaussians with large widths indicative of a turbulent velocity of ~ 18 km s^{-1} .

The following sections contain the detailed description of some of the important results cited above. The -5 km s^{-1} average velocity seen in the main components could be due to the presence of a large number of small discrete motions in the line of sight which are moving preferentially towards the observer. The discrete components do not appreciably change the line profiles but do cause a slight shift in the line peaks. The large scatter in the observed velocity could be either due to the presence of a non-negligible fraction of red shifted components or due to static components in the corona. The large scatter in the $(R_{i+1}^2 - R_i^2)$ plots against the coronal heights also arises from the same reason.

However, the presence of excess blue shifted components is not properly understood. This implies that the preferential direction of motion of the coronal plasma in the inner regions, is towards the observer. At this point, it is interesting to note that corona displays many asymmetries in its behavior. The activity of the northern hemisphere is generally found to be greater than that of the southern hemisphere in recent solar cycles with the maximum asymmetry seen at heliographic latitudes $\pm(10-20)^\circ$ (Gibson 1973, Petropoulos 1988). A different kind of asymmetry is seen in the observed velocities in the chromosphere-corona transition region. The observed velocities are mainly red shifted, possibly arising due to the downward motions of coronal matter at these heights (Athay & White 1977, Brueckner 1980, Athay el al., 1983). Our observation of $(R_{i+1}^2 - R_i^2)$ values at the active region (PA 250,260,270 of 1980) show a weak indication that in the innermost regions of corona ($\sim 1.05\ R_\odot$) the velocities become predominantly red shifted. The velocities of mass flow seen in the transition region lines, show a reversal in the sign of velocity at some point along the loop (Athay et al., 1983b). It may be speculated that the velocities are predominantly red shifted in the transition region and in the innermost regions whereas it becomes more blue shifted at greater coronal heights.

The increase in line of sight velocity with coronal height mainly seen in the active region corona is of considerable interest. The possibility of coronal rotation can be easily ruled out from the consideration that the magnitude of rotational velocity amounts to less than 2 $km\,s^{-1}$ at the observed heights while the observed increase in velocity is upto 15 $km\,s^{-1}$. Also, the east and west active regions show similar increase which cannot be expected from the rotation. The observed velocity increase may be due to three distinct possibilities; i) the existence of constant velocity loop flows which are mainly directed towards the observer ii) the acceleration of the loop flow towards the loop summit iii) wave propagation preferentially directed towards

the observer. Though none of the above possibilities can be ruled out, it seems most likely that the flow of plasma along the loop such as that arising from a siphon flow (Meyer & Schmidt 1968, Cargill & Priest 1980, Priest 1984) produces the observed effect. Wave propagation is generally not seen in the inner regions of corona (Parker 1983). If we assume the presence of constant loop flows, then the apparent increase in velocity could be produced by the increasing line of sight component of the velocity, which reaches a maximum at the loop summit. Velocity will vary as $\vec{v}\cos\theta$ where $\vec{v}$ is the constant loop flow velocity along the loop and θ is the angle between the line of sight and the instantaneous flow direction.

The presence of multicomponents in the line profiles must be arising due to the discrete motion of plasma in the line of sight with respect to the ambient medium. Since the loop evolution is a rather slow process with time scales of a few days, it is interpreted as due to the motions inside the loops. The motion of plasma along the coronal loop is considered in the coronal emission line modelling. The main features of the line profile could be reproduced from such a model. In the model, however, we have stressed the characteristics of loops rather than the ambient medium through the inherent assumptions, and hence in most of the cases (Figure 4.6), we see that the loop intensity has surpassed that of ambient medium. The situation is not a general case, but seems to be very relevant for the line profiles from the active region. From the multi-Gaussian decomposition of the observed line profiles from the active regions, we see the existence of strong, low velocity components with extremely low widths. Considering the small uncertainties in the nonlinear fitting program and the limitations of the photographic film which may introduce a 10% uncertainty in the widths, we may not give much importance to the absolute values of them. However, it is clear that stronger components do show lower widths, which then imply that at least some of the denser loops have lower kinetic temperatures (0.5–1 million K). The

MHD modelling of coronal loops (Hood & Priest 1979) shows that as the loop pressure increases, with its heating and length held fixed, the loop summit temperature rises to a maximum and then decreases to a critical value; further increase in pressure leads to a state of thermal non-equilibrium in which plasma cools and seeks a new equilibrium below 10^5 K. This mechanism provides an explanation for the existence of extremely cool cores that Foukal (1975,1976) and Jordan (1975) had observed in some coronal loops. A similar mechanism could explain the lower temperatures observed in the coronal green line. Alternatively, it could be due to the low temperature of the ambient medium in active regions, which seems unlikely.

In the line profile modelling, we encounter a similar situation (Figure 4.6 case 8), where the line profile represents the coronal loop more than the ambient corona. Since the temperature of the loop (1.5×10^6 K) which is less than that of the ambient corona(2×10^6 K), the width of the line profile drops to that corresponding to the loop temperature. The multi-Gaussian analyses of the line profiles from regions other than active regions, show subsidiary components with half widths equal to or more than that of the main component. This means that the kinetic temperature of the coronal loops and the ambient medium is more similar in the quiet corona while they are considerably different in the active region corona. The above result corroborates the earlier results from the wing intensity analysis of Fabry-Pérot fringes, that the coronal loops and ambient medium have different physical conditions in active regions while they are more similar in the low-activity regions. Strong magnetic fields in the active region producing a complete thermal isolation of the flux tubes, may be one of the possible reasons (Priest 1984).

The line of sight velocity associated with the subsidiary components in the 1980 solar maximum corona is in the range 10–73 km s^{-1} . There are evidences for

the existence of velocities both on the lower and higher sides. The observation of a $-5\ km\,s^{-1}$ average velocity associated with the main component could be due to the presence of large number of discrete components with velocities less than $10\ km\,s^{-1}$. The excess intensity found in the wing regions of Fabry-Pérot fringes could be due to the presence of discrete components with velocity $\sim 100\ km\,s^{-1}$.

The majority of the 1983 coronal line profiles do not show strong evidence of motion. The observed position angle covers only a 30° azimuth and is near the western equatorial region where a limited activity is seen. The background intensity in the 1983 profiles remained very strong and it is not possible to distinguish the weak components from the grain noise. However, a detailed analysis carried out later from a wider position angle coverage showed the presence of double or triple Gaussians (Chandrasekhar et al., 1991) in some of them. The relative velocity between the components was found to be $10-40\ km\,s^{-1}$.

Our observations convincingly show evidences of mass motions in solar corona which is associated, mostly, with the coronal loop flows. Strong mass motions with velocities $0-100\ km\,s^{-1}$ are observed in the solar maximum corona of 1980 while relatively weak mass motions with velocities $10-40\ km\,s^{-1}$ are seen in the declining activity phase of 1983. Some of the implications of mass flow are discussed here. The speed of sound in solar corona is about $200\ km\,s^{-1}$ (Roberts 1987) and hence the observed velocities are subsonic. Cargill and Priest (1980), from a model of the siphon flow along the coronal loop, find that for small pressure difference between the loop foot points, the flow remains subsonic; for large pressure difference between the loop foot points the flow becomes supersonic and is then slowed down by a shock wave in the downflowing leg. The observed velocities are consistent with the model of subsonic coronal siphon flow and this would suggest that the pressure differences are

small between the loop foot points. The skylab EUV observations revealed frequent brightening of the loops near the loop foot points which was interpreted as due to in-situ energy release and the infall of coronal material. Also, the coexistence of loops containing plasma at different kinetic temperature, an observation we verify in the coronal green line, suggests heating by fast mode MHD waves (Habbal et al., 1985). The effect of mass motion in a semicircular loop of length 1.2×10^4 km and radius 3.8×10^3 km with a constant cross section of 300 km was studied by Mariska (1984). The emission measure-based calculations indicate steep temperature gradient which would produce departures from the ionization equilibrium.

The existence of coronal loops and loop flows are important in coronal heating. The mass motions such as bulk flows and magnetic flux tube emergence are considered as a plausible mechanism of coronal heating (Narain & Ulmschneider 1990). The heating of the upper solar atmosphere by spicules is proposed by Athay and Holzer (1982). Downflows observed in the coronal flux tubes are found to contribute to the atmospheric heating (Hasan & Schüssler 1985). The heating by the emerging flux tubes is considered by Gokhale (1975); the magnetic energy from an emerging flux tube such as a single x-ray bright point is found to provide the sufficient heating for eight hours. Magnetic reconnection between the adjacent flux tubes (Uchida & Sakurai 1977) and topological heating by the slow relaxation of the stressed magnetic field by the foot point shuffling (Parker 1983, 1987, 1990) are two another flux tube related heating mechanisms which could involve mass motions. It appears that the role of siphon flow along the coronal loops in coronal heating, should be considered in detail in the theoretical modelling.

Chapter 5

Studies on the Coronal Green Line

The green line at 5303 Å of [FeXIV] is often the strongest line in the visible coronal spectrum. Though it is one of the most observed line, the details of the emission mechanism are not properly understood. It is generally believed that the line originates mainly due to the excitation of FeXIV ions through the collisions of electrons and protons with them (cf Chandrasekhar 1982). However many authors have reported significant contribution from radiative excitation at varying coronal heights (Singh 1985, Raju & Singh 1987, Zirin 1988). The availability of a few coronal photographs both in the white light and in the green line obtained during the 1980 total solar eclipse, enabled us to re-examine this problem. The idea of a structured corona is increasingly being appreciated in recent years, with nearly two orders of magnitude difference in the electron density and a factor of two to three difference in the kinetic temperatures in various coronal regions. It is therefore thought worthwhile, to study the excitation mechanism in different coronal regions to know the possible variations.

The line to continuum intensity ratio which can be obtained from the coronal photographs is in itself, an interesting quantity with a certain dependence on the coronal activity.

The excitation mechanism of the coronal green line is discussed in the first section of this chapter. The method of approach was the following. The relative roles of various excitation mechanism was computed from the known coronal physical conditions. The line to continuum intensity ratio of the green emission line was calculated by using the standard equations. This is then compared with the observed values of the same and inferences were made. The line to continuum intensity ratio in various position angles was derived from the photographs of corona, one taken without filter and another with a band width filter centered at 5303 Å. The excitation mechanism in various coronal regions was deduced from the behavior of the curves of line to continuum intensity ratio against the coronal height. The variation of the ratio in various coronal regions is discussed in the next section. A possible determination of ionization temperature from the line to continuum intensity ratio in the corona is also explained.

5.1   Excitation Mechanism of the Coronal Green Line

The excitation mechanism of the coronal green line remains to be understood, especially regarding the individual contributions from collisional and radiative mechanisms (Singh 1985, Zirin 1988). It is extremely important to decide the actual mechanism

from the point of view of coronal modelling. This is because the observed line intensity has different functional dependence on the physical quantities according to the two excitation mechanisms. We have made an attempt to determine the dominant mechanism for the excitation of this line. A detailed theoretical calculation of the various excitation mechanisms and the resulting line to continuum intensity ratio for an average coronal region may be seen in Raju & Singh (1987). However, their estimation of the continuum intensities based on the levels of minima between FP fringes can be subjected to significant errors in the presence of large random velocities in the corona (Desai et al., 1990). We, in the present analysis, derived the line to continuum ratio from a narrow band coronal filtergram in 5303 line and a white light picture of the corona obtained during the 1980 total solar eclipse.

5.1.1   Observation and Data Analysis

Details of the observation are given in chapter II. (Desai et al., 1981, Sahu etal., 1981, Chandrasekhar 1982). Both the filter and white light photographs were digitized and the analysis of the digitized frames were carried out on a computer. The solar center in each frame was taken as the reference point for data scanning. Knowing the diameters of the lunar and solar disks during the 1980 epoch to be 33′ 23″ and 32′ 38″ respectively, appropriate corrections were performed to get the solar coordinates from the frames. Matching of the two frames was also carried out at this stage, to get the corresponding directions in two frames. This was done by a one to one comparison of the individual streamer structures at their top side where they are seen as narrow rays in the two frames. The photographic density against the coronal radial distance was calculated for various position angles using a computer software. The photographic densities of three adjacent directions of 0.5° angular separation were averaged at each

113

radial point, in order to minimize the noise. The photographic densities were then converted into the relative intensities, using a photographic characteristic curve.

5.1.2 Results and Discussion

In the filter photograph, the measured exposure can be represented as

$$E_l = \alpha I_l + \beta I_c \tag{5.1}$$

and in the continuum picture, the measured exposure can be written as

$$E_c = \gamma I_c \tag{5.2}$$

where α, β and γ are constants depending upon the instruments as well as the exposure time. α and β are proportional to the fractional transmission of the line and continuum intensity through the filter respectively and γ is a proportionality constant. I_l is the integrated intensity across the line while I_c is the continuum intensity per angström.

The ratio (α/β) can be obtained from the transmission profile of the filter. A pre-calibrated grating spectrometer was made use of, for this purpose. Transmission at different wavelengths (T_λ) in the filter passband was determined. $(\int T_\lambda d\lambda)$ give the value of α multiplied by a constant. β was found similarly by knowing the transmission characteristics of an average coronal green line profile through the filter. We have obtained $(\alpha/\beta) = 0.08$. This implies that the transmitted light through the filter have only an 8% contribution from the line, rest coming from the continuum. This has put a limit on the radial coverage of the useful values of line to continuum intensity ratio to about 1.6 $R_\odot$.

The white light picture was taken with a polarizer in the ray path. So, to get the actual unpolarized intensities, a correction was made, taking into account the radial variation of polarization in the solar corona as given by Athay(1976) (Figure 5.1) and the known orientation of the polarizer. The transmitted intensity through a polarizer is related to the unpolarized intensity according to

$$I_0 \left[\left(\frac{1-f}{2} \right) + f \sin^2 \theta \right] = I_p \qquad (5.3)$$

where I_0 and I_p represent the unpolarized and the polarized intensities respectively, f is the degree of polarization and θ is the angle of orientation of the polarizer.

We have from equations 5.1 and 5.2,

$$\frac{E_l}{E_c} = \frac{\alpha}{\gamma} \frac{I_l}{I_c} + \frac{\beta}{\gamma} \qquad (5.4)$$

The dominant mode of excitation of the coronal green line can be inferred from the behavior of E_l/E_c with r. This was done by theoretically calculating the line to continuum intensity ratio in the corona and comparing its behavior with the ratio of the observed exposures.

The radiative component of I_l is given by

$$I_l \, (rad) \, (r) = c_1 \int_{-\infty}^{+\infty} n_e(r) \, w(r) \, dl \qquad (5.5)$$

where w(r) is the geometrical dilution factor. It is given by

$$w(r) = \frac{1}{2} \left[(1-u) \left(1 - \left(1 - \frac{1}{\rho^2} \right)^{1/2} \right) + \frac{u}{2} \left(1 - \rho \left(1 - \frac{1}{\rho^2} \right) \ln \left(\frac{\rho+1}{\rho-1} \right)^{1/2} \right) \right] \qquad (5.6)$$

u is the limb darkening coefficient; u=0.69 for green line (Allen 1973). r is the coronal radial distance in units of $R_\odot$. c_1 is defined in eq.(5.10).
The collisional component of I_l is

$$I_l \, (col) \, (r) = c_2 \int_{-\infty}^{+\infty} n_e^2(r) \, dl \qquad (5.7)$$
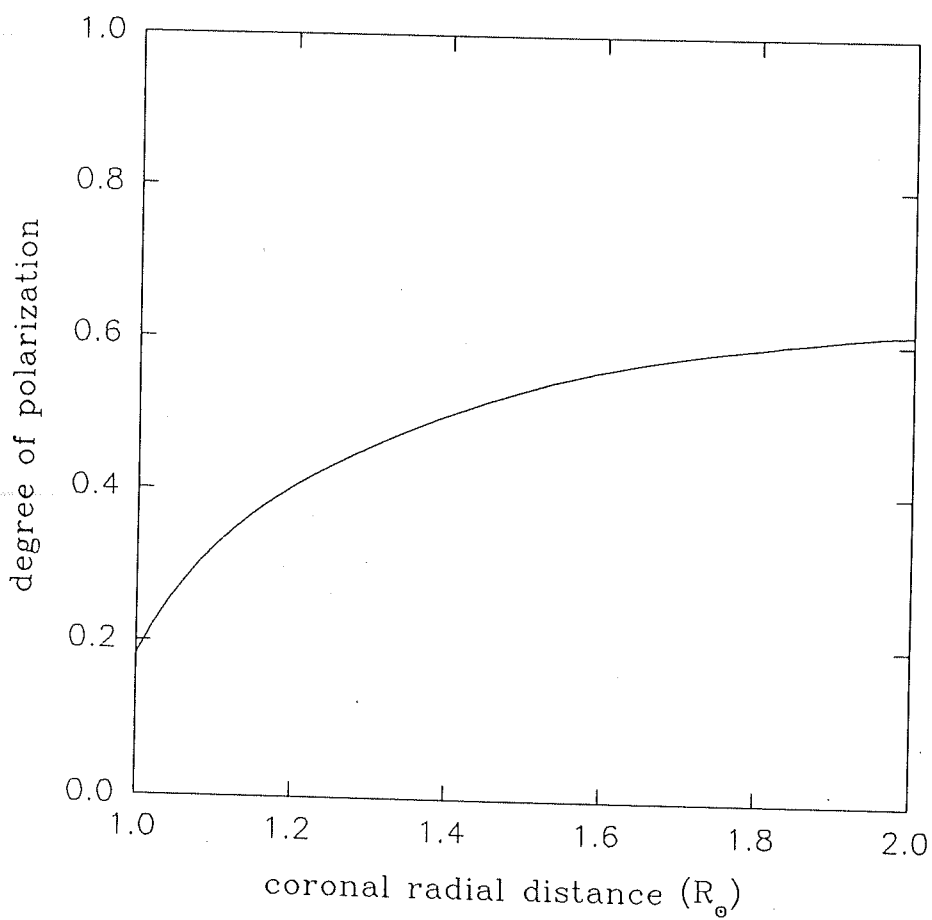
Fig. 5.1   Degree of polarization in the corona (Athay 1976).

c_2 is defined in eq.(5.11). Hence the total intensity is given by

$$I_l(r) = I_l(rad)(r) + I_l(col)(r) \qquad (5.8)$$

In writing the above equation, we have neglected the collisional and radiative deexcitaion terms in the radiation balance equation, which are very small in comparison with the spontaneous emission term. Typical values in corona at about 1.10 $R_\odot$ are radiative deexcitation rate $\sim 0.54 \text{sec}^{-1}$, collisional deexcitation rate $\sim 0.78 \text{sec}^{-1}$ and spontaneous emission rate=60 sec^{-1} (cf Peraiah & Varghese 1989).

The Continuum intensity is given by

$$I_c(r) = c_3 \int_{-\infty}^{+\infty} n_e(r)\, w(r)\, dl \qquad (5.9)$$

where

$$c_1 = R_\odot \frac{g_j}{g_i} \left[\exp\left(\frac{h\nu_{ij}}{kT_R} \right) - 1 \right]^{-1} \frac{N(FeXIV)}{N(Fe)} \frac{N(Fe)}{N(H)}$$

$$0.83\, A_{ji} \frac{h\nu_{ij}}{4\pi} \qquad (5.10)$$

$$c_2 = R_\odot \left[8.63 \times 10^{-6} \frac{\Omega_{eff}}{T_e^{1/2} g_i} \exp\left(-\frac{h\nu_{ij}}{kT_e} \right) \frac{N(FeXIV)}{N(Fe)} \frac{N(Fe)}{N(H)} 0.83 \right.$$

$$\left. +1.38 \times 10^{-9} \times 0.83 \right] A_{ji} \frac{h\nu_{ij}}{4\pi} \qquad (5.11)$$

$$c_3 = R_\odot J_0^\lambda \sigma_e \qquad (5.12)$$

where

g_i, g_j are the statistical weights of the lower and upper transition levels; g_i=2, g_j=4

T_R is the radiation temperature oft he photosphere; T_R=5795 K

A_{ji} is the spontaneous transition probability; A_{ji}=60 sec^{-1}

Ω_{eff} is the effective collision strength; Ω_{eff}=2.84 for T_e=2$\times10^6$ K (Mason 1975)

T_e is the electron kinetic temperature; T_e=2$\times10^6$ K

J_0^λ is the mean solar intensity at 5303 Å; $J_0^\lambda = 3.06 \times 10^6$ erg cm^{-2} sterad^{-1} Å^{-1}

σ_e is the Thomson scattering cross section. $\sigma_e = 6.66 \times 10^{-25}$ cm^2

The ratio $\frac{N(FeXIV)}{N(Fe)}$ is given by Jordan (1969); those values for which the dielectronic recombination was taken into account, were used for the present calculation. The iron abundance ratio, $\frac{N(Fe)}{N(H)} = 7 \times 10^{-5}$. Electron density $n_e(r)$ is tabulated by Newkirk (1961, 1967) and Dürst (1982).

It can be seen that c_3 is a constant while c_1 and c_2 are constants only for an isothermal corona. The line of sight integral was evaluated within the limits – 2R$_\odot$ and +2R$_\odot$, since no appreciable contribution to line intensity was found to come beyond this. Line to continuum intensity ratios were calculated using the electron density distribution given by Newkirk (1961) for the equatorial solar maximum corona and for an average coronal temperature of 2 million degree K. The result is shown in Figure 5.2. (I_l/I_c) values for the radiative and the collisional mechanisms are plotted separately. It can be seen that for pure radiative excitation, the ratio (I_l/I_c) is a constant while for pure collisional excitation, it decreases with increasing radial distance (Billings(1966), Singh(1985), Raju & Singh(1987)). The calculations show that the collisional processes are highly dominated in the line excitation, especially in the inner regions of corona. Both the contributions become equal at about 1.6R$_\odot$.

Since (I_l/I_c) is linearly related to the observed exposure ratio (E_l/E_c), the behavior of the former with r may be judged from that of the latter. In Figure 5.3, we have plotted the ratio (E_l/E_c) against coronal radial distance for various coronal position angles. The figure shows that (E_l/E_c) becomes constant at different radial distances in different position angles. (E_l/E_c) becoming constant with respect to r

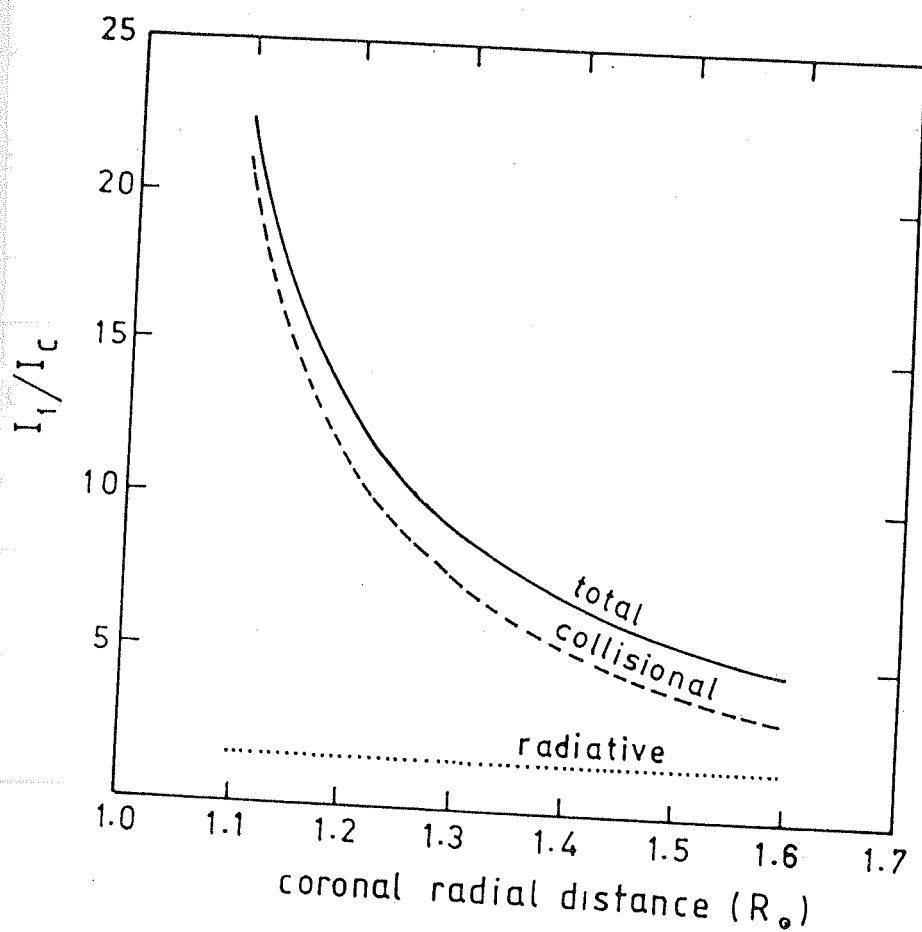Fig. 5.2   Computed values of line to continuum intensity ratio for equatorial, isothermal (2 million K) solar maximum corona. The collisional and radiative contributions as well as the total intensity are marked.
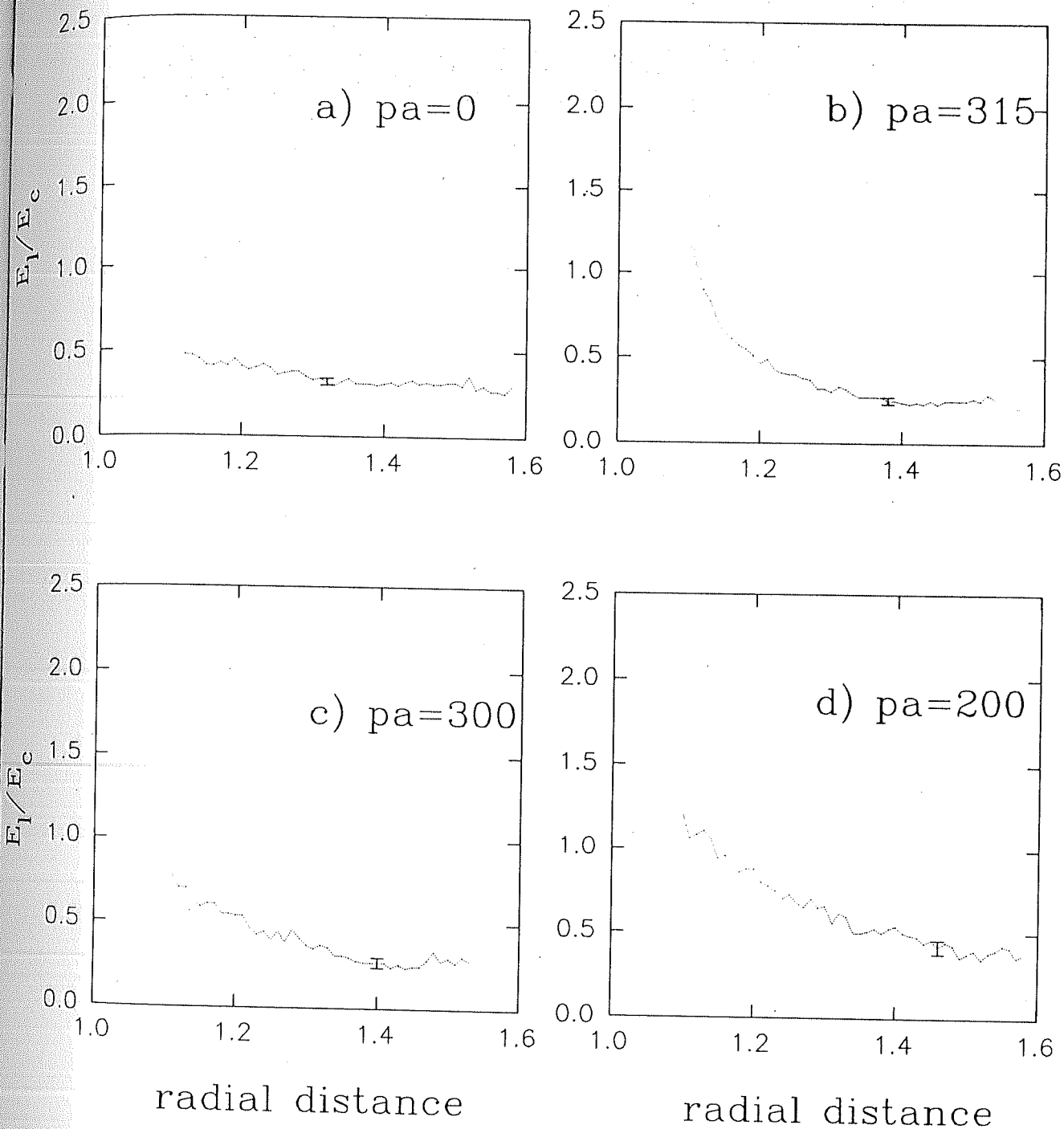
Fig. 5.3 Ratio of the observed exposures (E_l/E_c) against coronal radial distance in units of $R_{\odot}$; respective position angles and the error involved in the measurement are indicated.
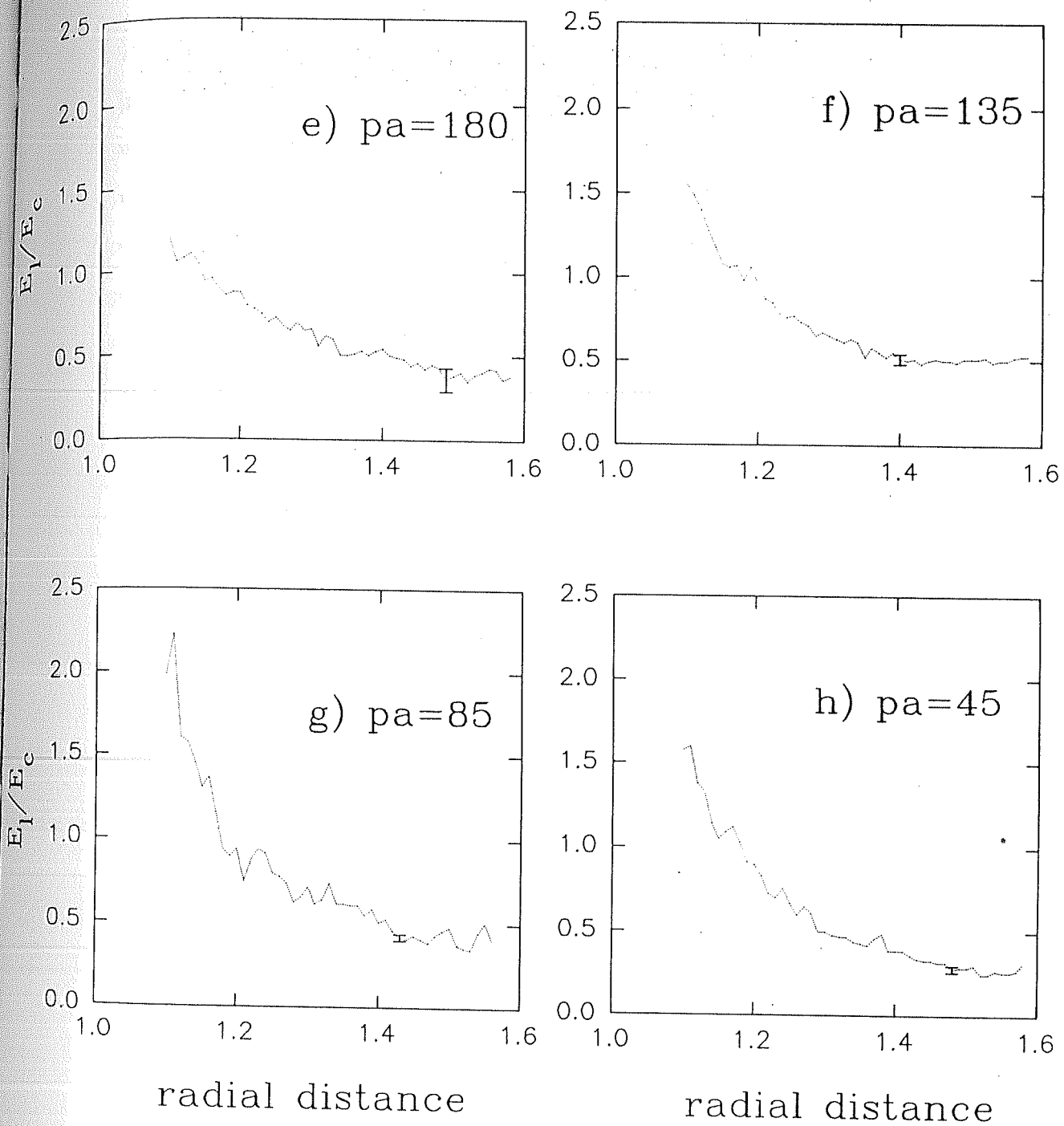
Fig. 5.3 continued

indicates either the domination of radiative excitation or $(\alpha I_l \ll \beta I_c)$. In table 5.1, we have tabulated the values of (E_l/E_c) at the respective radial distances when they become constant. The constant value of (E_l/E_c) observed at different azimuths has no significant variation above the uncertainties of the measurement. However, at two specific azimuths (pa 135 & 85), it is distinctly larger. This could be due to the contribution of radiative excitation to the line intensity. In these azimuths, the value of E_l is larger than the same for other azimuths, at constant (E_l/E_c). The higher value of (E_l/E_c) may be due to the significant contribution from radiative excitation and the favourable temperature at these azimuths. It should be kept in mind that the line intensity is sensitive to the temperature of the region observed and the green line intensity reaches a maximum at a temperature of 1.8 million K (Jordan 1969).

The variation in the excitation mechanism of the line in different coronal regions was studied in the following way. The line by continuum intensity ratio was calculated for different coronal regions and then it was compared with the observed ratios from the appropriate position angles. Table 5.2 gives the electron density distribution in different coronal regions such as 'quiet', 'polar' and 'active' are tabulated by Newkirk (1961). The results of the theoretical calculations are plotted in Figure 5.4. The observed (I_l/I_c) values for the three representative position angles are shown alongwith, for the purpose of illustration. The details of the calculations are also given in table 5.3. The contribution from the radiative mechanism to the line intensity in different coronal regions is shown separately. The model calculations indicate that line excitation mechanism depends very much on the activity of the coronal region. Collisional mechanisms are more important in the inner coronal regions; however radiative mechanism becomes progressively important outwards. In active regions, radiative contribution is only an insignificant fraction of the total intensity in the innermost

Table 5.1: Radial distances at which (E_l/E_c) become constant; Columns denote the position angle, the radial distances where (E_l/E_c) become constant in units of $R_\odot$, the ratio (E_l/E_c) and the value of E_l in arbitrary units, respectively

pa	$E_l/E_c = const$ at (r)	E_l/E_c	E_l
0	1.32	0.32±0.02	3.89
315	1.38	0.25±0.02	2.45
300	1.40	0.25±0.03	2.00
200	1.46	0.27±0.04	1.45
180	1.49	0.39±0.07	1.15
135	1.40	0.50±0.03	4.68
85	1.43	0.41±0.02	6.31
45	1.48	0.27±0.02	2.75

Table 5.2: Electron density distribution in different regions of corona (Newkirk 1961); Columns denote coronal heights in units of solar radius and electron densities in different coronal regions in units of(10^8) cm^{-3}

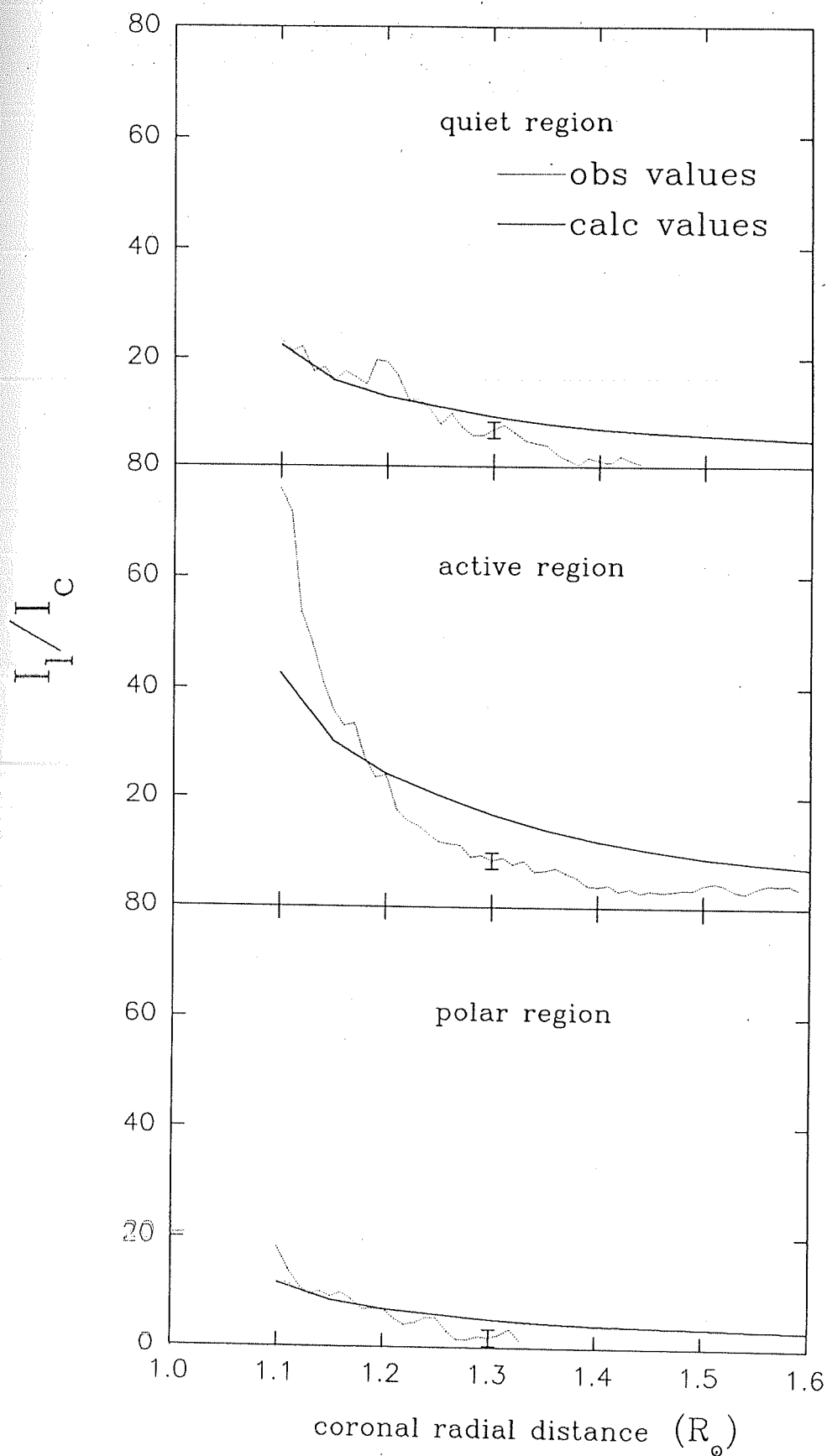| r in $R_\odot$	Quiet (10^8) cm^{-3}	Active (10^8) cm^{-3}	Polar (10^8) cm^{-3}
1.0	9.0	16.30	4.3
1.125	2.9	5.7	1.4
1.25	1.2	2.4	0.57
1.375	0.57	1.14	0.27
1.50	0.33	0.61	0.16
1.625	0.20	0.35	0.095
1.75	0.13	0.213	0.062
2.0	0.062	0.090	0.029

Fig. 5.4   Line to continuum intensity ratios in various coronal
regions, solid curve represents the model calculations;
dotted line represents the observed values.

regions. In polar regions the contributions from the two excitation mechanisms become more or less equal at about $1.6R_\odot$. The value of the constant (α/β) was found from the ratio (E_l/E_c) at large r $(\sim 1.5R_\odot)$ where $\alpha I_l \ll \beta I_c$. Knowing the constants (β/γ) and (α/β), the actual line to continuum ratio (I_l/I_c) was calculated. From the above discussion, it is apparent that the dominant mode of excitation of the green line can be decided from the behavior of the line to continuum intensity ratio in coronal heights. Though the assumption of an isothermal corona may not be fully justified, the departures from it are unlikely to cause significant changes in the behavior of the curve. Thus it can be expected that a strong dependence of (I_l/I_c) on coronal heights should signify a dominant collisional mechanism while a weak dependence should indicate a dominant radiative excitation. In Figure 5.5, we have plotted (I_l/I_c) values against coronal heights for different position angles. The radial extent upto which the green line emission was recorded in the FP interferogram is also marked in the figure. Figure 5.6 (reproduced from Rusin & Rybansky, 1982) shows the structures seen in solar corona during the 1980 total solar eclipse. It is now possible to compare the activity of the particular coronal region and the associated excitation mechanism of the green line.

From the behaviour of (I_l/I_c) versus coronal radial distance plotted in Figure 5.5, we conclude that the main excitation mechanism of the coronal green line, in most of the corona towards the inner regions at solar maximum periods, is collisional processes. In the open north polar region (pa 0, 10, & 20), the dominant excitation mode could be radiative excitation, as evident from the extreme weak dependence shown by the curves. However, in the southern polar region, where no structures are apparent, the dominant mode is collisional processes. Most of the coronal position angles are filled with streamer structures and coronal loops and the dominant mode of excitation in these regions is collisional processes as seen from the rapid fall

126

Table 5.3: Computed values of (I_l/I_c) for different coronal regions and the percentage of radiative contribution

r	Quiet		Active		Polar	
($R_\odot$)	I_l/I_c	radiative %	I_l/I_c	radiative %	I_l/I_c	radiative %
1.10	22.52	6.9	42.81	3.6	11.79	13.2
1.15	15.88	9.8	30.46	5.1	8.55	18.2
1.20	12.90	12.1	24.40	6.4	7.04	22.2
1.25	10.96	14.2	20.39	7.7	6.04	25.8
1.30	9.24	16.9	16.95	9.2	5.17	30.2
1.35	7.86	19.9	14.10	11.1	4.51	34.6
1.40	6.90	22.6	11.92	13.1	4.09	38.1
1.45	6.22	25.1	10.26	15.2	3.81	40.9
1.50	5.69	27.4	8.98	17.4	3.56	43.8
1.55	5.21	29.9	7.96	19.6	3.32	47.0
1.60	4.80	32.5	7.16	21.8	3.18	49.1

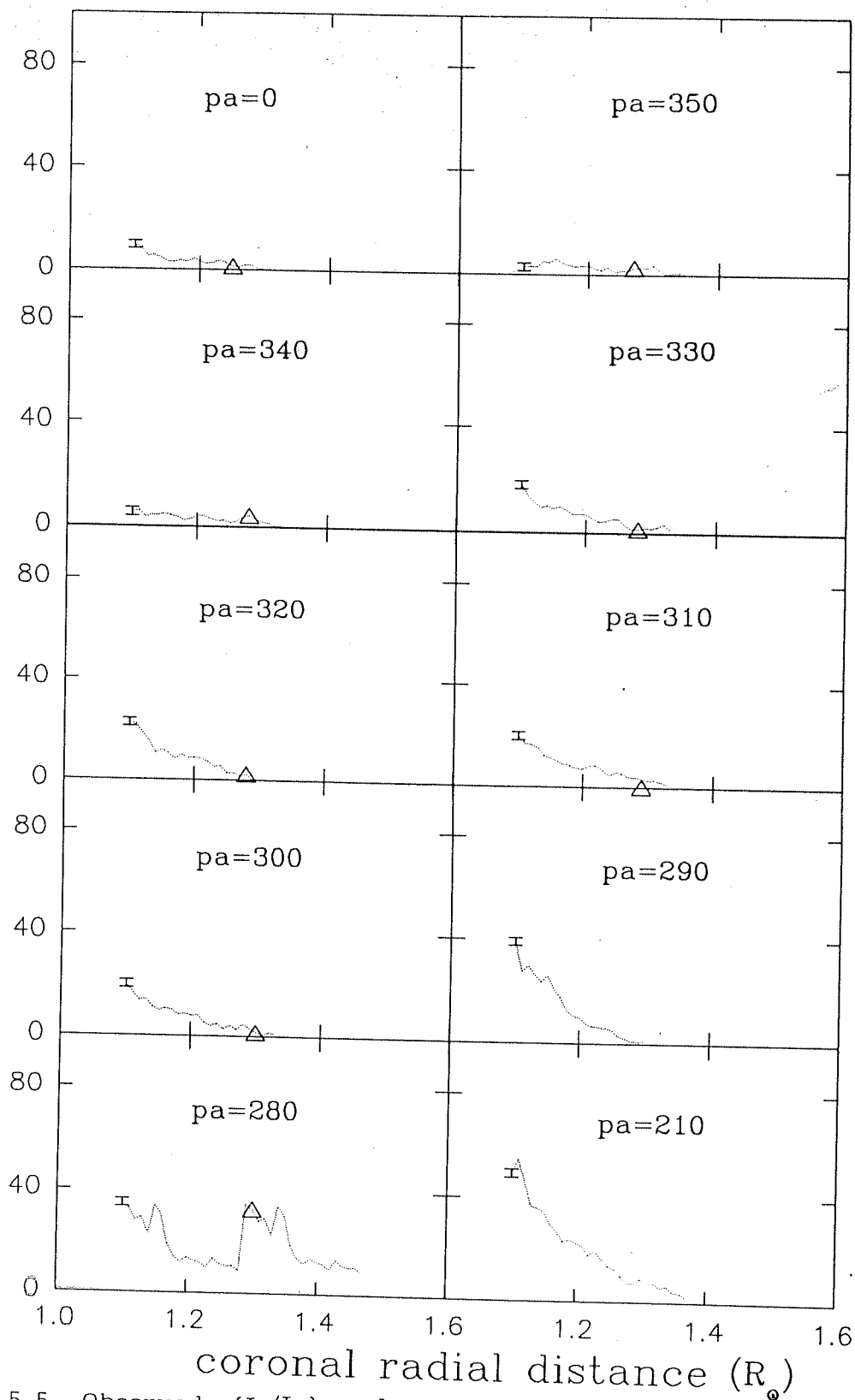Fig. 5.5 Observed (I_l/I_c) values against coronal radial distance in various coronal position angles; measurement error is shown at the beginning of every plot; triangles represent the radial position upto where green line emission is seen in interferograms.
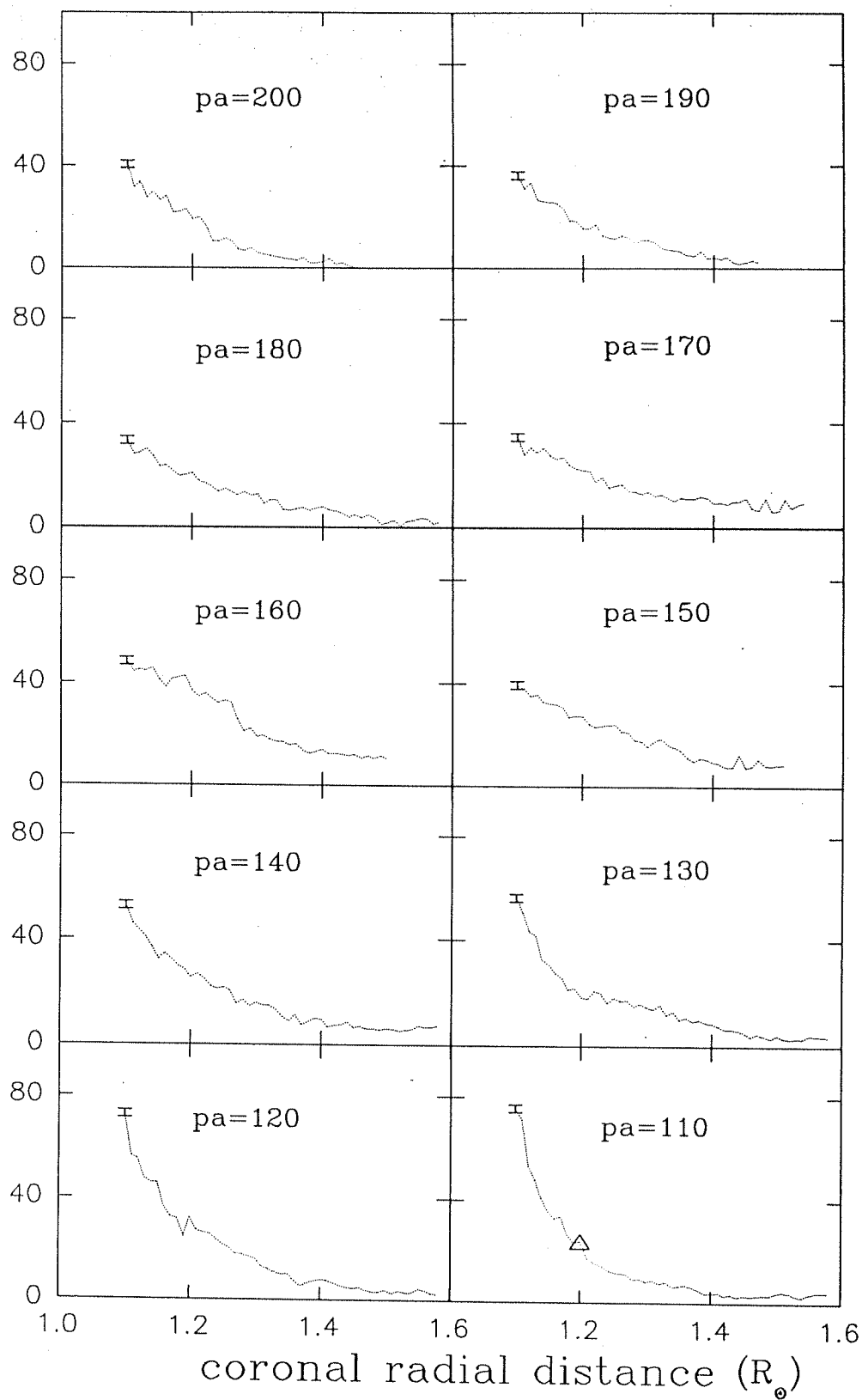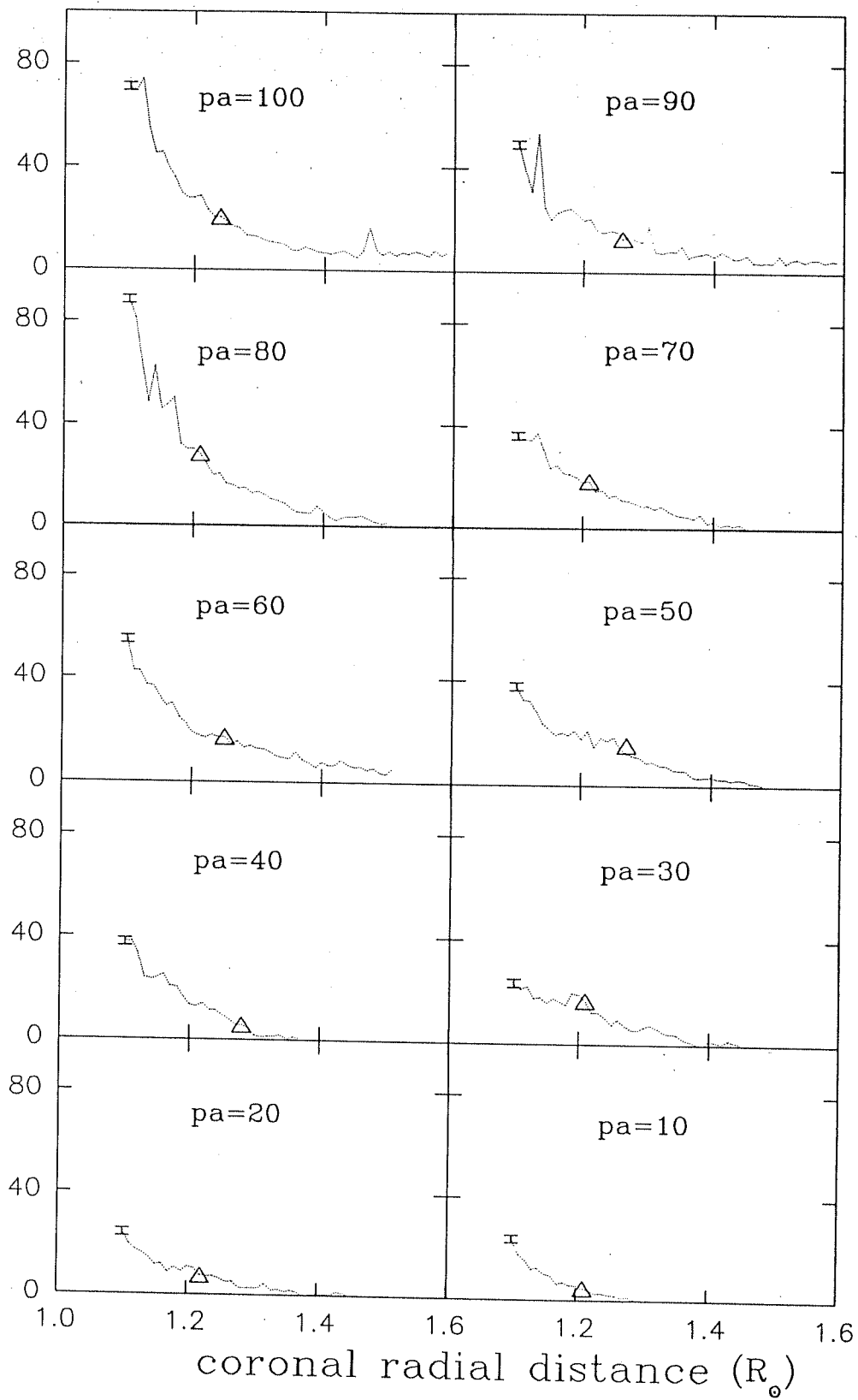
Fig. 5.5 continued
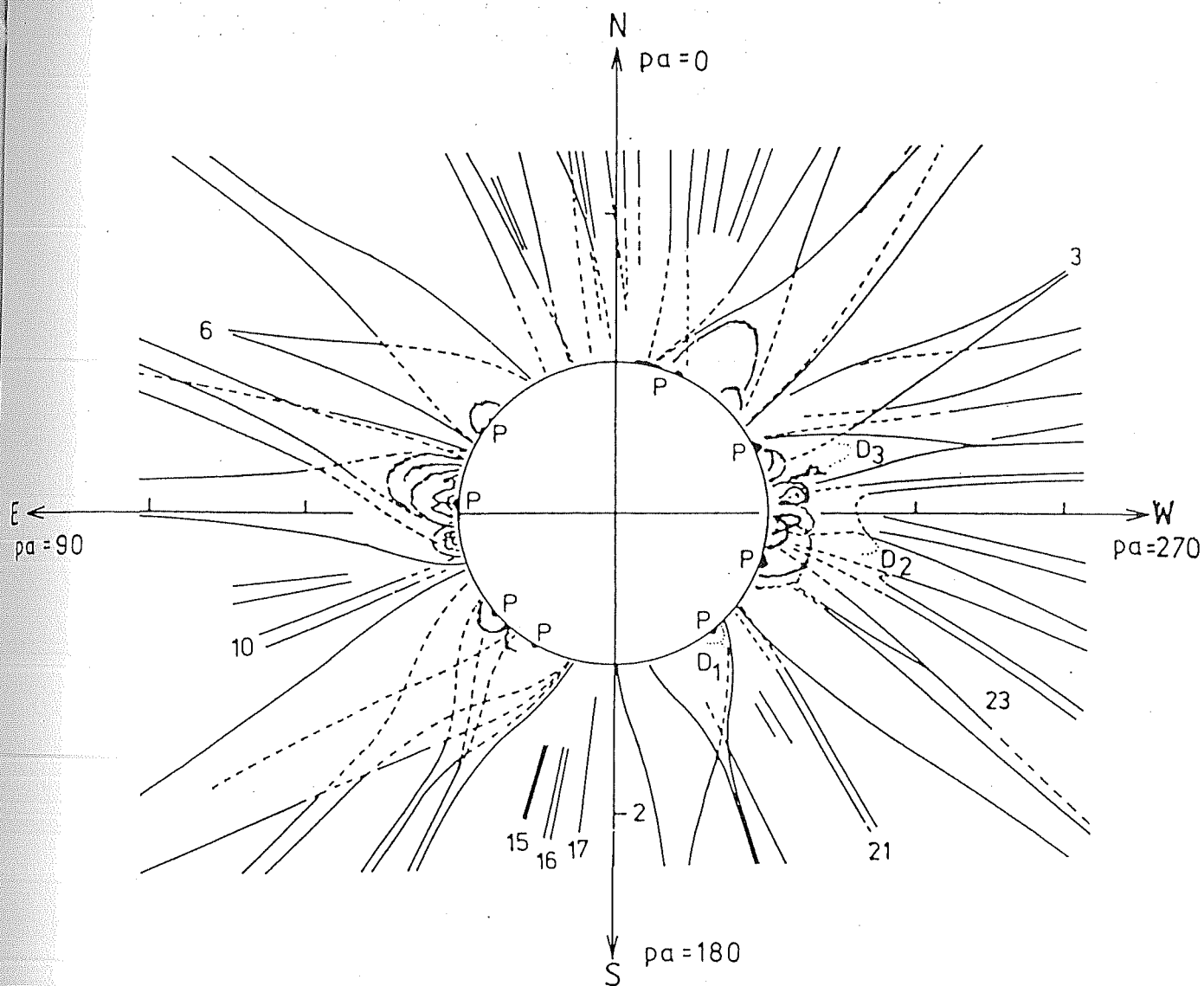
Fig. 5.5 continued

Fig. 5.6   Structure of the solar corona during the 1980 total solar
eclipse (Rusin & Rybansky 1983); position angles are
marked.

of the curves in these position angles. The electron density in the structured corona was found to be high and the expected mechanism is mostly collision dominant, as also seen from the theoretical calculations. It is interesting to note some hump-like structures in the curves, in some position angles especially in the active regions (pa 80, 290, 280). A discontinueous change in the physical conditions in corona such as a situation where the line of sight encounters a coronal loop with a larger than ambient electron density and a more favourable temperature could be the possible reason. A very distinct evidence for radiative excitation is seen in the eastern active region (pa 100, 90 & 80) beyond the radial distance 1.45 $R_\odot$ to about 1.60 $R_\odot$; the ratio (I_l/I_c) becomes constant at these positions, but remained well above the value observed at other position angles. In the western active region unfortunately no data was available to see this interesting aspect. The epoch 1980 represents the peak of solar activity cycle. One expects a different situation in a declining activity epoch such as 1983 where the electron densities are less by a factor of two (Newkirk 1967). However no photographs were available to make an inter-comparison.

5.2 Line to Continuum Intensity Ratio

The observed line to continuum ratio was calculated as described above, in most of the position angles at a 10° interval, in the radial range 1.10–1.60 $R_\odot$. A contour plot (Figure 5.7) of the same was made with superposed solar coordinates to see the azimuthal and radial variation of the ratio in different coronal regions. In active regions the value was found to be approximately 100 at 1.10 $R_\odot$. The ratio is about 30–40 in the coronal streamers and in polar regions it is less than 10 at the mentioned radial point. It can be seen that the values of line to continuum intensity ratio differ
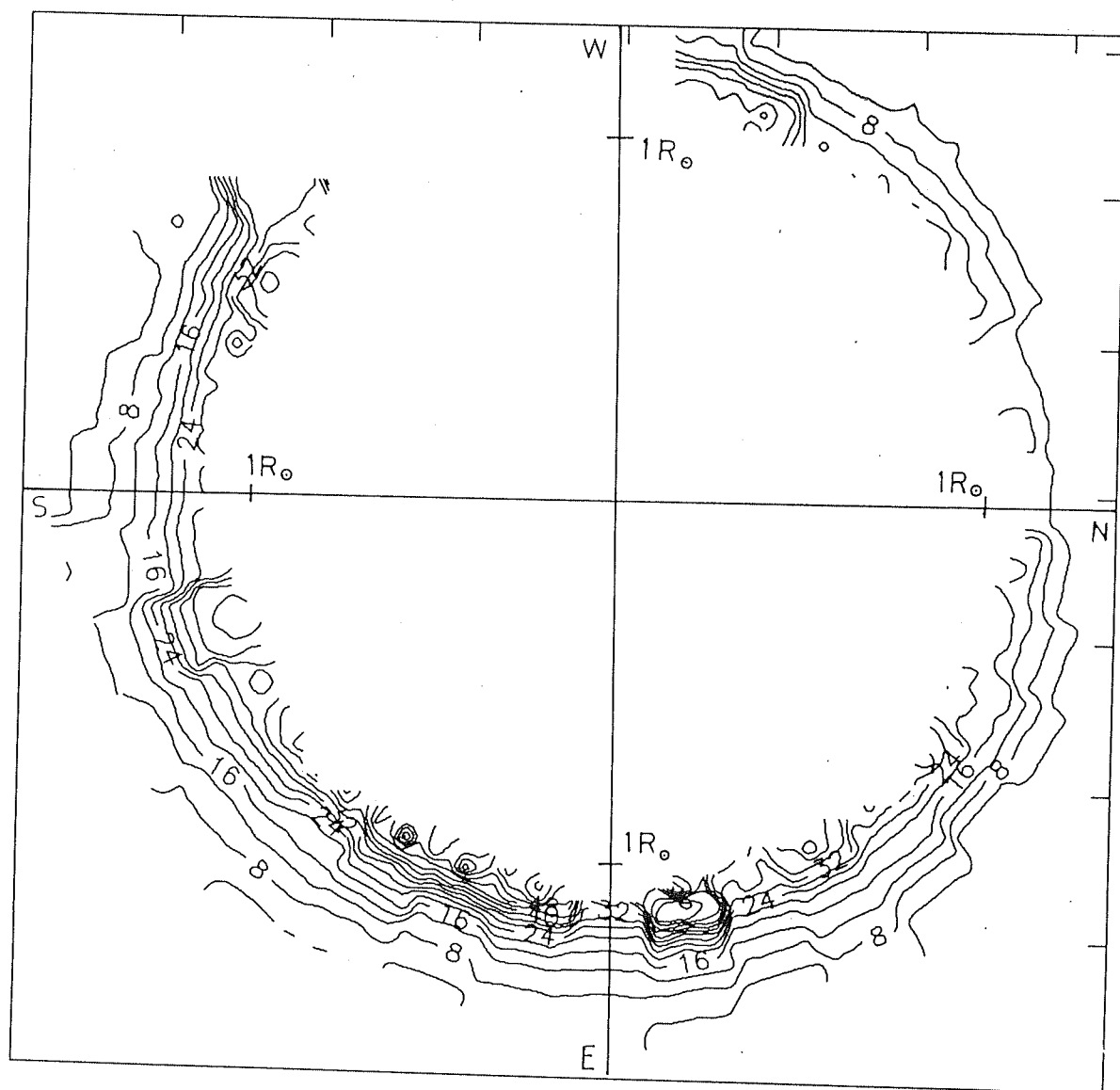
Fig. 5.7 Contour map of (I_1/I_c) over the solar corona observed during the total solar eclipse of 16 Feb. 1980; contour interval is 4.

by two orders of magnitude, in the active and hole regions at the solar maximum periods.

A possible use of the value of line to continuum ratio is the determination of the actual coronal temperature. The measurement of coronal temperature from the emission line width is frought with the uncertainties of microturbulent velocity (Billings 1966, Newkirk 1967, Chandrasekhar 1982). The estimation of the temperature from the ratio of line intensity to the square of continuum intensity is described by Liebenberg et al., (1975) and Chandrasekhar (1982). The estimation can be done more accurately by comparing the observed line to continuum ratio distribution with the theoretically calculated ratio for different assumed isothermal coronal temperatures. However, because of the nature of the ionization curve (Jordan 1969), one value of the ratio can be produced by two temperatures on either side of 1.8 MK, which corresponds to the peak of the curve. Alongwith the emission line width measurements which give the approximate temperature distribution, this provides a very accurate measurement of coronal temperature.

Chapter 6

A Fabry-Pérot Interferometric Study Of The Orion Nebula

6.1   Introduction

In this chapter, we deal with an entirely different astrophysical plasma–the HII region, which may be defined as that part of an interstellar cloud, where the ionizing radiation from a newly born O or B star has formed a hydrogen plasma around it. The electron density and magnetic field are smaller by six orders of magnitude while the kinetic temperature is smaller by two orders of magnitude, in HII region than that of the solar corona. Consequently, the origin, evolution and dynamics of the two regions are quiet different. However, from the observational point of view some similarities can be pointed out; both are extended objects and both emit strongly in forbidden emission lines in the visible spectra. During the course of study, we have carried out an observational program of some of the bright HII regions such as the Orion, Rosette

and Lagoon Nebulae. Fabry-Pérot observations were made in a relatively infrequently studied emission line [SII] 6731 Å , which is prominent in the farthest regions of nebula from the ionizing star. Here we describe the observations and the preliminary results obtained from the study. In the first section, HII region is introduced in the interstellar context explaining its importance in the star formation. A brief observational history on the kinematics of Orion Nebula is described in the second section. The next section deals with the observation and data reduction techniques which is more or less the same as in the case of solar corona. In the final section the results obtained are explained.

6.1.1 Interstellar Medium

In the solar neighborhood of our galaxy, the ratio of the average distance between stars to star diameter is of the order 1pc:10^6 km; this means that only a tiny fraction of the space, of the order of 10^{-22} is occupied by the stellar matter. There are however, great masses of gas and dust existing in the medium between the stars. The total mass of the interstellar matter in a galaxy is estimated to be 5–10% of the total galaxy mass (Scheffler & Elsässer, 1988). The average density of the interstellar matter is on an average 1 atom per cm^{-3} in a galaxy, but often high concentrations in the form of clouds are seen. The details of the origin of such clouds are not really known, but they are found to be scattered along the spiral arms of the galaxy. The nearest cloud is the Orion Molecular Cloud, which lies in the lower fringes of the spiral disk, some 450 pc farther out from the Sun (Waldrop 1982). The composition of the molecular cloud is mainly hydrogen, with small admixtures of carbon, oxygen, nitrogen and the silicate dust. Line radiation from the molecular clouds has also revealed the presence of about 40 different types of molecules, both organic and inorganic. They include hydroxyl

radicals, carbon monoxide, ammonia and alcohol. The complex molecules are found in larger and massive concentrations which are impenetrable to the optical radiations, while in less dense clouds, one often finds only the simple and stable molecules.

When an early type (spectral type O or B) star is born in such a cloud, it ionizes the surrounding medium considerably by its copious supply of uv radiation, thereby producing a thin thermal plasma (10^4 K) around the star. Such a region is known as an ionized hydrogen region or HII region. Strömgren(1939) showed that the region of ionized hydrogen around the hot star should have relatively sharper outer boundary. Well known examples of galactic HII regions are Orion Nebula(M42), Rosette, Lagoon(M8), Trifid(M20) etc. Important physical properties of some of these objects are described in Table 6.1. A large variety in the sizes of HII regions are observed. Radio observations revealed the existence of small compact HII regions, many of which do not have an optical counterpart. They are probably the early stages of HII regions. Giant extragalactic HII regions with linear dimensions greater than 100pc are observed in emission lines such as H_α and [OIII]. Their velocity widths are particularly useful as distance calibrators (Melnick et al., 1979).

One of the early observations of Orion Nebula was made by Christian Huygens in the 17th century (Habing 1974). John Herschell made a detailed study of the Nebula in around 1820 with a telescope. In 1857, G.P.Bond determined the position of a large number of stars in the nebula and also made an engraving of it (Ashbrook 1975). William Huggins viewed the spectrum of the nebula as early as in 1869 and identified the hydrogen emission lines in it. The widespread nature of the interstellar phenomena was known only after the introduction of photography into astronomical observations. Henry Draper produced the first successful photograph of Orion Nebula in 1880. The existence of the general interstellar medium was convincingly known

Table 6.1: Physical characteristics of some of the bright galactic HII regions (Scheffler & Elsässer 1988); columns denote the name of the nebula, apparent dimension in arc minutes, Distance in kiloparsec, greatest linear extent in H_α in parsec, name and spectral type of the exciting star, electron density and electron temperature

Name	App Dim (arc min)	Dist (kpc)	Ext (pc)	Excit Star Name	Spect type	n_e cm^{-3}	T_e K
Orion M42=NGC1976	90×60	0.5	13	θ^1 Ori C	06p	2000	9,000
Rosette NGC2237-46	80×60	1.6	37	6 stars of NGC2244 cluster	05-O9v	30	7,700
Trifid M20=NGC6514	20×20	2.1	12	HD 164491 NGC2244 cluster	07	100	8,200
Lagoon M8=NGC6523	45×30	1.4	18	stars of NGC6530 cluster	05-B0	60	7,500
Omega M17=NGC6618	20×15	2.1	12	stars of a cluster	04-O8v	800	8,700
Eagle M16=NGC6611	120×25	2.2	77	stars of NGC6611 cluster	05-B0	100	8,000
North American NGC7000	120×30	1.2	42	CygOB2 Assoc HD199539	06	15	

138

only after the two important discoveries made around 1930. The gas component was discovered by the observation of the systematic increase in the strength of interstellar absorption lines in the stellar spectra by O.Struve in 1928. The general extinction due to the dust component was found out by R.Trumpler in 1930, from a comparison of photographic and geometric determination of the distance to the open clusters (Shu 1982, Scheffler & Elsässer 1988). The year 1930 accordingly marks the approximate starting point of the study of interstellar matter as a new branch of astronomy.

Interstellar clouds are the sites of star formation. HII regions are the localities of interstellar clouds where star formation is at an advanced stage. A complex interaction between the cloud and the HII region through the involvement of the ionization fronts and the associated shocks, stellar winds, turbulence, magnetic field and possibly the external agencies such as supernova shocks produces generations of stars in the cloud complex. Therefore interstellar clouds are come to known as 'stellar nurseries' where stars are born and reared.

6.1.2   Orion Nebula

The Orion Complex is the most convenient object in the sky for the study of interstellar matter and star formation. The first observations of the protostars as well as most of the interstellar molecules were made here (Genzel & Stutsky 1989). The proximity and brightness of the nebula have lead to many important discoveries about the interstellar matter. For the same reasons, Orion Nebula served as the prototype object for HII region studies. Excitation of the Orion Nebula arises from the four Trapezium stars θ^1Ori A,B,C,D. θ^1Ori C is the only O star, rest are B type and hence it is the primary ionizing star. Some 1.5′ to the south-east one finds two stars called

θ^2OriA and θ^2OriB. Trapezium stars are the brightest members of the OB association IOri, which contains 56 stars of spectral type earlier than B2 (Habing 1974, Genzel & Stutsky 1979).

A model of the Orion Nebula and nearby regions was developed in recent years (Zuckerman 1973, Balick et al., 1974, Pankonin et al., 1979). The main features of the model are shown in Figure 6.1. This combined with the champagne phase of evolution of the HII region provides a good description of the nebula (Tenorio-Tagle 1979). A vast molecular cloud with intermixed dust known as the Orion Molecular Cloud (OMC1) is the starting point in the model. Massive high temperature stars (Trapezium stars) were born at the periphery of the cloud facing the terrestrial observer, and their ionizing uv radiation produced an HII region at the edge of the cloud. The gradual heating of the HII region resulted in a local expansion, and collision with the side of the cloud facing the observer. The evaporating ionized gas which streams away from the cloud surface to the HII region forms a champagne flow towards the observer thereby explaining the blue shift of the ionized gas relative to the neutral gas (Genzel & Stutsky 1989). The stellar winds emanating from the young stars may also affect the evolution. The intensity maxima of the molecular emission comes from the compressed region in the background. The KL infrared Nebula is situated behind θ^1C, near the front surface of OMC1. More recent work has shown that this object is really a number of individual sources some of which are stars at the earliest stages of formation while others are more likely compact knots of gas and dust. These components are presently known as IRc1, IRc2 etc. (Celnik 1985).

Many of the optical and radio observations indicate that there is no significant temperature gradient exists in the vicinity of the Trapezium stars (McCall 1979, Pankonin et al., 1979). Electron density decreases away from the core and is peaked
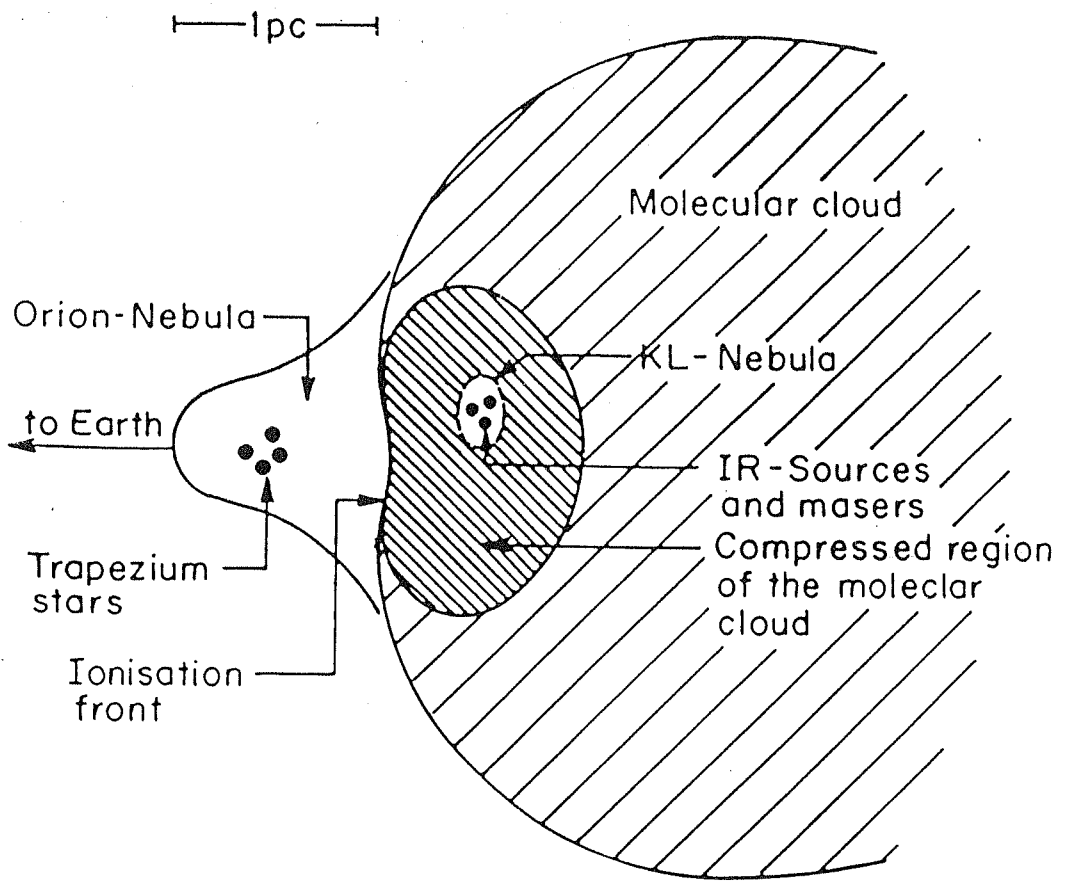
MODEL OF THE ORION NEBULA

Fig. 6.1   Model of the Orion Nebula (Zuckerman 1973).

at 30″ from the Trapezium stars suggesting the existence of a ring of high density material (Elliot & Meaburn 1973, Cosmovici et al., 1979). Magnetic field strength in the vicinity of Orion, is about 10 μG, as measured from the Zeeman splitting of hydrogen 21 cm line (Heiles & Troland 1982). The polarization measurements show that the dust grains are aligned with the magnetic field, which suggests that magnetic field is trapped in and is oriented along the long axis of the cloud. The directions of the several optical outflows are aligned with the large scale magnetic field, indicative of the important role played by the field in star formation (Genzel & Stutsky 1989).

One unique feature of the Orion complex is that the Orion OB association and the molecular clouds are surrounded by a tenuous shell of ionized gas, more than 100 pc in diameter. The shell is expanding outwards at about 100 km s^{-1}. It is suggested that the shell may be either the outer edge of a shock wave propagating into the ISM from a supernova or the stellar winds from the OB stars. Barnard's Loop, a partial ring of ionized gas discovered in 1898 by E.E.Barnard is simply the inner rim of this shock wave (Waldrop 1982).

6.1.3   The Orion Complex and Star Formation

The young stars are usually found at the edges of the interstellar clouds and this led to the suggestion that star formation is set off by an impact from outside. The process is continued inside the cloud and ultimately exhausts there itself. However, in some cases such as in S106, the star formation appears to emanate from the center of the molecular cloud (Scheffler & Elsässer 1988). In Orion complex, star formation seems to have progressed in an ordered way. The OB stars are arrayed in a linear fashion, where younger stars are seen progressively away from the earth. The chain

leads directly into the Trapezium cluster and continues past the visible nebula into the densest parts of the cloud, where the next generation of stars are just seen as hot spots in the infrared spectra (Waldrop 1982). Elmegreen and Lada (1977) proposed a model of star formation inwhich they pointed out that a newly-born massive star ionizes the surrounding molecular cloud and pushes it outward with a velocity of 5 to 10 km s^{-1} which creates a shock wave that sweeps up the cloud material as it expands. The shocked gas after a million years, condense to form a second generation of stars. Many of the second generation stars will be hot enough to ionize the surrounding medium, produce shocks and form a third generation of stars. This sequence of star formation is continued into the cloud, leaving behind the chain of stars as we see in the Orion complex.

6.2 Kinematics of Orion Nebula

Kinematic study of Orion Nebula began with the development of Fabry-Pérot techniques, by the turn of this century. Fabry and Buisson studied the internal motions in M42 by Fabry-Pérot interferometry first in 1911 and later in 1914 (Fabry & Buisson, 1911, Buisson et al., 1914). Observational techniques have improved tremendously since then, with the observations in the other wavelength regimes such as radio and infrared and with the new sophisticated electronic detectors. In recent years space-borne measurements were also made, including that using space telescope.

The two traditional approaches in the kinematical studies of nebulae have been the large aperture Fabry-Pérot Spectrometer and the echelle spectrograph (Celnik 1985). Observations generally indicate that the emitting gas inside the nebula is extremely inhomogeneous. Strong variations in the line intensity, line profiles and

Doppler displacements are observed. Evidences of several motion fronts and filaments along the line of sight are seen (Loren 1979, Sugitani et al., 1986, White & Phillips 1988). It is found that mean radial velocities of HII regions in general, follows the differential galactic rotation; thus the observed radial velocities are an indicator of their distance. There is a large scale velocity change observed along the Orion A cloud from the south-east to the north-west and this has been interpreted as the rotation of the cloud along the east-west axis. The rotation period is estimated to be 4×10^7 years. The sense of rotation is found to be opposite to that of the differential galactic rotation (Kutner et al., 1977).

One of the pioneering observation on the kinematics of Orion Nebula was carried out by Wilson et al., (1959). The velocity field in a region of $4' \times 4'$ centered on Trapezium stars was obtained in [OII]$\lambda 3726$, [OIII]$\lambda 5007$ and H$_\gamma$ using the Coude spectrograph and the 200inch Palomer reflector. The average non-thermal velocity of 5–7 km s^{-1} and a mean radial velocity of 10 km s^{-1} with respect to the Trapezium stars were found which was interpreted as the expansion of the HII region into the surrounding gas. Later observations indicated line splittings in many regions of the nebula which were seen to be associated with the major ionization fronts and large neutral masses (Smith & Weedman 1970, Meaburn 1971, Deharveng 1973, Dopita et al., 1973, Elliot & Meaburn 1974). Line splitting was also observed in other HII regions such as M17 (Elliot & Meaburn 1975) which is being interpreted as the expansion of HII regions by a series of ionization fronts eating into the densest parts of the adjacent inhomogeneous neutral clouds. The existence of three velocity components are seen in the central parts of the Orion Nebula in [OIII] 5007 Å measurements (Goudis et al., 1984, Castaneda 1988). Presence of strong supersonic mass motions were reported by many authors (Lee 1969, Taylor & Munch 1975). It is generally found that the kinematical features shown by high ionization lines such as Hα, O^{2+},

He^{2+} are different from that shown by lines of low ionization lines such as O^0, C^+, N^+ and S^+. The difference arise because the lines of first category arise from the nebular interiors where the gas travels at sound speed relative to the ionization front, whereas the lines of the latter category arise in a region near the ionization front where pressure gradients are only partially effective in accelerating the gas. Fabry-Pérot observations of the nebula in different spectral lines show that $v_{OIII} \leq v_{H_\alpha} < v_{NII} < v_{SII}$. (Balick et al., 1980). Radio observations show a good correlation between the kinematics of Hn_α with that of H_α and high ionization lines (Balick et al., 1980, Kaler 1969). Radio recombination line observation of $H76_\alpha$ show a general pattern in the velocity field in which the more negative velocities near the edge of the nebula and the more positive near the center. The characteristics were interpreted as the ionizing star being located at the edge of the massive neutral cloud and the ionizing material being flown away from the neutral cloud towards the general direction of the observer (Pankonin et al., 1979).

Massive stellar winds that are million times stronger than solar wind are seen to be associated with the star formation processes. Axon and Taylor(1984) pointed out the existence of biconical pattern of outflows from the massive protostars embedded in the molecular cloud. Observations of many other regions of star formation indicate that bipolar outflow is a common phenomenon associated with the protostars (Zuckerman 1984).

There are a number of observations which point out that the gas in HII region is in a state of turbulent motion (Wilson et al., 1959, O'Dell 1985, Roy et al., 1986, O'Dell 1986). Turbulence is studied from the velocity widths, radial velocities and the structure function, calculated from the emission line profiles obtained from the nebula. It is found that turbulent motions are well ordered, but they show deviations from

Table 6.2: Spectral characteristics of the sulphur doublet (Allen 1973); columns denote the spectral transition, Wavelength of the lines and the transition probability respectively

Transition	Wavelength Å	Trans Prob A s^{-1}
$3p^3\ ^4S_{3/2}-^2D_{5/2}$	6716	0.0005
$3p^3\ ^4S_{3/2}-^2D_{3/2}$	6731	0.0043

the equilibrium theory of turbulence predicted by the Kolmogorov theory (O'Dell 1985, 1986). Dependence of random velocity upon scale length is found, but the variations of the slope indicate that turbulent energy enters the nebula at different scales (O'Dell et al., 1987, Castaneda 1988). Outflows from the embedded young stars are considered as a possible source driving the turbulent motion in the cloud (Fukui et al., 1986).

[SII] line at 6731 Å

The forbidden emission line at 6731 Å , is the stronger component of the sulphur doublet in red; both are electric quadrupole transitions with very low transition probabilities. The characteristics of the two lines are given in Table 6.2. The line intensity ratio of the doublet is used to calculate the electron density in nebulae (Osterbrock 1974). The relative strengths of the two lines are 0.05 and 0.09 respectively for the 6716 and 6731 line (Grandi 1975). The ionization potential of sulphur is less (10.36 eV) as compared to the higher ionization species such as singly ionized oxygen, and

hence the sulphur emission lines are believed to be stronger in the regions near to the ionization fronts in a nebulae (Balick et al., 1980) and because of this it serves as a good probe of the various phenomena associated with ionization front. Line emission is consequently extended to the farthest regions of the nebula. It is found that the velocities in the [SII] line are larger than that observed from the other lines (Hanel 1987). However sulphur lines are intrinsically fainter. Balick et al., (1980) find that the emission line flux is only about 3% of the H_α flux. Hence one may require relatively large telescope aperture and exposure times for the kinematical observations. Recently selected regions of Orion Nebula were observed with the Hubble Space Telescope (HST) with a spatial resolution of 0."1(Hester et al., 1991, Sky & Telescope Mar 1991). The [SII] line emission is found to be dominated by filamentary features which highlight the ionization fronts moving into the dense neutral clouds; they trace the shocks at the walls of an ionization jet, which apparently emanates from a star embedded in the dark cloud.

6.3 Observation and Data reduction

Observations were made at Kavalur, India with the 1m Carl-Zeiss telescope on 7 December 1989. An imaging Fabry-Pérot interferometer with an image intensifier and photographic film (Chandrasekhar et al., 1988) serving as the detector, was used to get the interferograms. The emission line [SII] 6731 Å was separated out by a narrow band interference filter. The instrument details are as given below.

FP etalon type	: solid etalon
Refractive index of the etalon material	: 1.46
Quoted spacing of the etalon	: 250 μm
Reflectivity	: 85(5500-7000) Å
Free spectral range	: 6.21 Å
Instrumental resolution	: 0.41 Å
Filter bandwidth	: 10 Å
Filter peak transmission	: 60 %
Film used	: 2415 kodak
Plate scale in the film	: 17."5 /mm

Image Intensifier

Since the observed emission line is relatively faint, a high gain second generation image intensifier was made use of, in the data collection. The working principle of the image intensifier is very simple. The optical image which falls on a S-20 cathode is converted to an electron image, which is then passed through microchannel plates producing an intensified electron image; this intensified image is converted again into the optical image by a phosphor screen of p-39 type. An optical fiberglass plate is used to transfer the image from the phosphor screen to the detector, which in this case is a photographic film. The magnification factor of the image intensifier used was 1.2. The parameters of the image intensifier used (Debiprasad 1988) are listed below.

Effective diameter of the multialkali photocathode	: 25 mm
Spectral range	: 3500–9100 Å
Wave length of the peak response of intensifier	: 6000 Å
Variable gain	: 20,000 to 40,000
Weight	: 300g
External power supply	: 3 V dc

The schematic diagram of the observational set up is shown in Figure 6.2. A calibration interferogram was taken in 6707 Å from a Li spectral lamp. The interferogram of the Orion Nebula is shown in Figure 6.3. The four Trapezium stars can be clearly seen in the picture. The interferograms thus obtained were digitized with a PDS microdensitometer with a pixel size of 10 μm. The stored data consists of three information; the x,y coordinates of the pixels and the photographic density. The data was stored record by record and later analyzed in a computer.

Following procedure was adopted to estimate the relative line of sight velocities of various points in the nebula; first, the fringe maxima points were identified in the frame. The density values in the five adjacent records which correspond to $\sim 1''$ were averaged. The data was then scanned record by record. In every record, those points which satisfy the following two criteria were selected as the probable locations of fringe maxima; i) the density of the pixel should be more than that of 25 nearest pixels on either side; ii) the pixel thus selected should have a density, more than a threshold value. The resulting points were then thoroughly checked for the star images and other noise patterns such as image intensifier spots; they were removed manually, to get the actual fringe maxima.
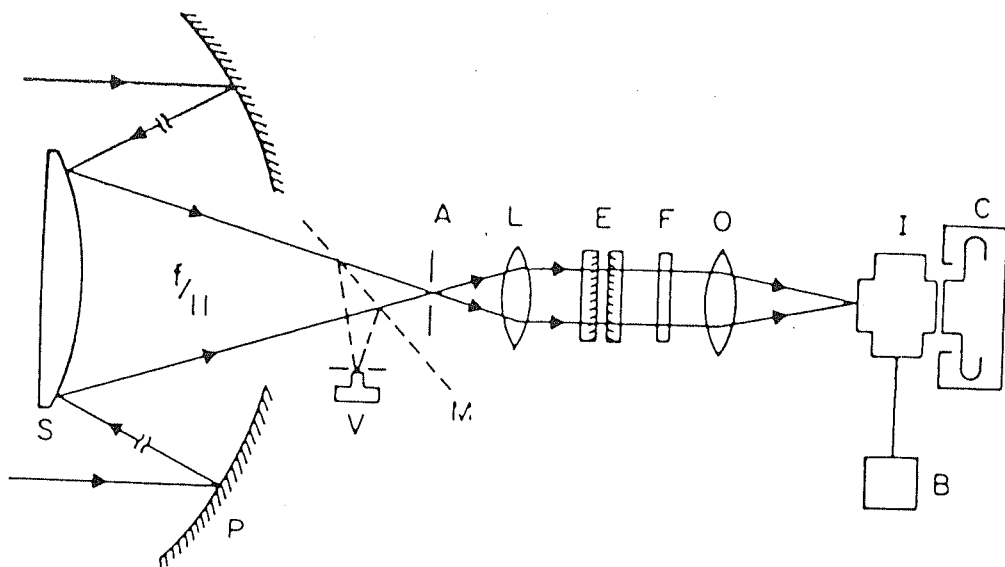
Fig. 6.2   A schematic diagram of the imaging Fabry-Perot Interfero-
meter used in the observations of the Orion Nebula.

S = Secondary mirror of the telescope

P = Primary mirror of the telescope

V = Visual port   M = Flip mirror assembly

A = Entrance aperture   L = Collimator lens

E = Fabry-Perot etalon   F = Narrow band filter

O = Camera lens   I = Image intensifier

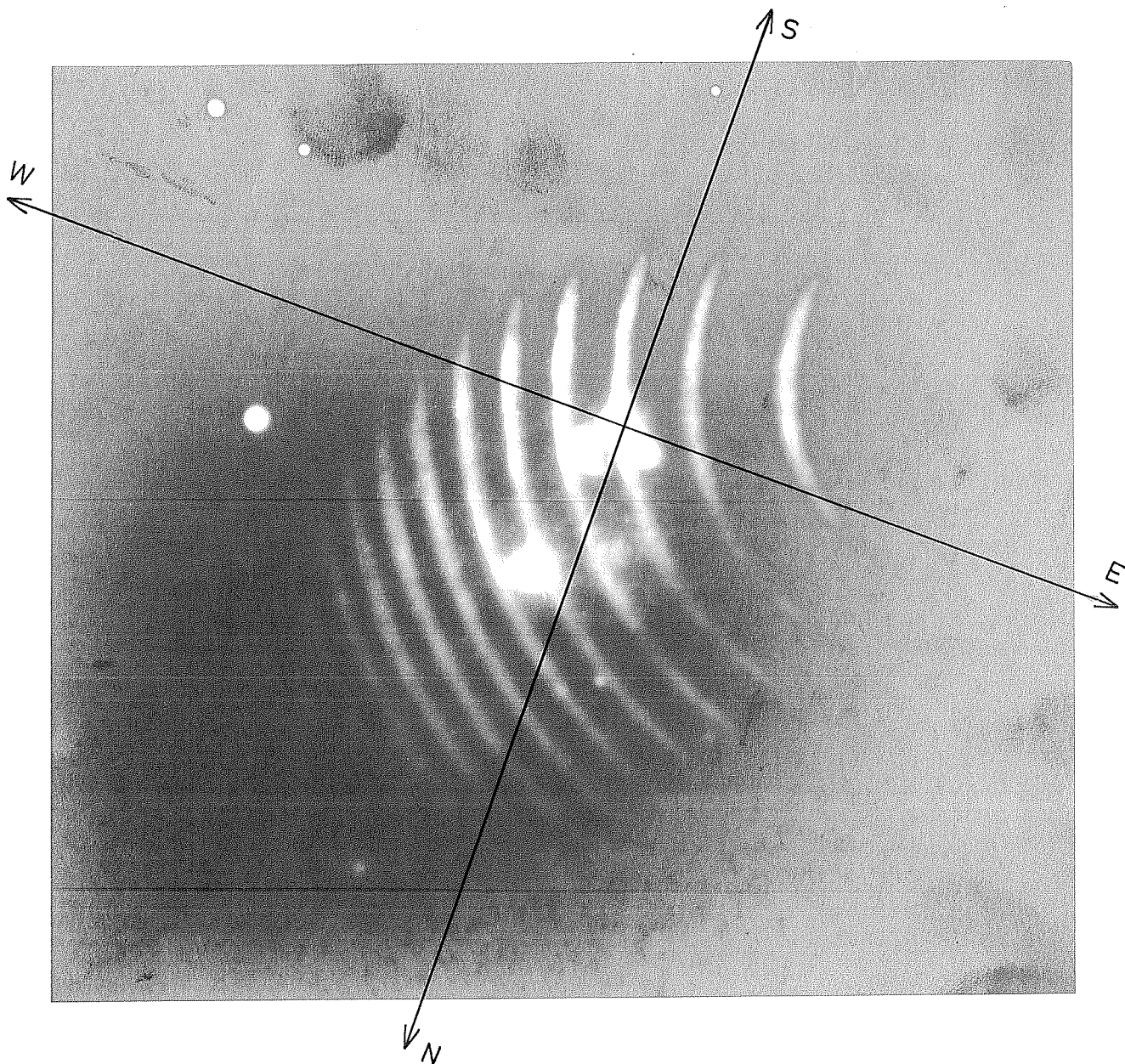B = Battery supply   C = Camera.

Fig. 6.3 [SII] interferogram of the Orion Nebula; Four Trapezium
stars can be seen in the middle.

A least square circle is then fitted to the coordinates of the fringe maxima, to get the most probable center of the fringe system. The difference between the square of the individual fringe maxima point and the square of the radii of the average radius of the fringe was noted down. The relative line of sight velocity was then calculated according to

$$\left(R_i^2 - \overline{R}^2\right) = \frac{F^2}{\mu t}\, n\, \Delta\lambda \qquad (6.1)$$

which follows directly from the constructive interference condition in the Fabry-Pérot etalon. R_i is the radius of the individual fringe maxima point, $\overline{R}$ is the average radius of the fringe. The value of the etalon constant $\left(\frac{F^2}{\mu t}\right)$ is obtained from the calibration fringes.

$$\frac{F^2 \lambda}{\mu t} = {R'_{i+1}}^2 - {R'_i}^2 \qquad (6.2)$$

The primed quantities denote the radii of the calibration fringes.

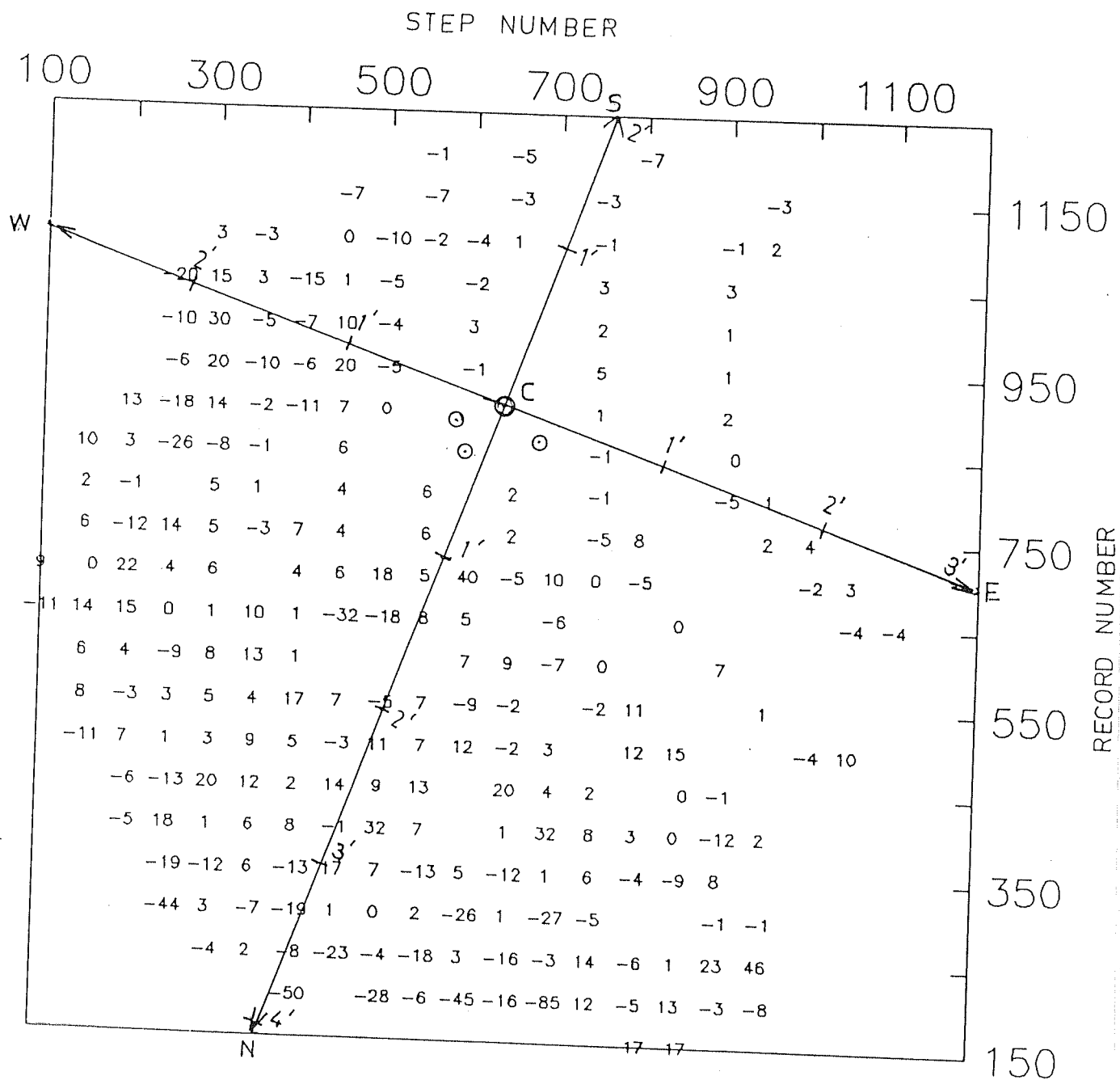$$\frac{\Delta\lambda}{\lambda_0} = \frac{v}{c} \qquad (6.3)$$

The procedure was repeated for all the fringe maxima points and hence a velocity map was constructed.

6.4 Results and Discussions

The observed field corresponds to about $6' \times 6'$ on the face of the nebula. The sulphur emission is extended slightly beyond the nebula and hence it is a useful probe of the HI-HII interface (Balick et al., 1980). From the interferogram, we see that the emission is more extended in the regions NW of the Trapezium stars. During the analysis, we have calculated the relative line of sight velocities at about 1500

points in the nebula. Relative line sight velocity represents the deviation from the average velocity in the nebula and hence it is expected that the presence of mainly the localized phenomena such as outflows from the newly formed stars, stellar winds, jets and shock discontinuities associated with the ionization fronts will be seen in a two dimensional map of the same. Most of the systematic motions in the nebula will be averaged out in the present analysis. For this reason, it may not be necessary to correct the observed velocities to the local standard of rest (LSR). The error involved in the measurement of individual velocity is ± 4 km s^{-1}. The relative line of sight velocities averaged over a grid size of 10$''$ on the face of the nebula (1$''$ corresponds to 0.0021 pc) are shown in Figure 6.4. A similar map of radial velocities observed in Lagoon Nebula is given by Hanel (1987). A contour map of the observed velocities is displayed in Figure 6.5. The positions of four Trapezium stars θ^1Ori A,B,C,D are marked in the figure. The origin of the coordinate system is taken as θ^1C, the primary ionizing star of the nebula. The intervals of 1$'$ field are marked in the diagrams. In Figure 6.5, we have plotted only those contours whose magnitudes are above ± 10 km s^{-1} and the interval between the contours is 5 km s^{-1}.

An examination of the two figures reveals three points immediately; i) velocities in the southern regions of Trapezium stars are small and is of the order 2 km s^{-1} ii) velocities are of the order $+10$ km s^{-1} in the regions immediately below Trapezium stars iii) large velocities ~ 30 km s^{-1} lie in the nebular boundaries. We compare our results with that of Balick et al., (1980) obtained from the observation of Orion Nebula in six emission lines (H$_\alpha$, HeIλ5876, [OIII]λ5007, [NII]λ6584, [SII]λ6717 and [OI]). On the basis of the above-mentioned observation, they have proposed a flow model for Orion HII region which is a refinement of the earlier model developed by Zuckerman (1973), Balick et al., (1974), Pankonin et al., (1979), Meaburn (1975). The basic features of the model are the following; the ionizing radiation from the

Fig. 6.4 Relative line of sight velocities averaged over a grid size 10" on the face of the Orion Nebula. Step number and record number indicate the parameters of digitization.
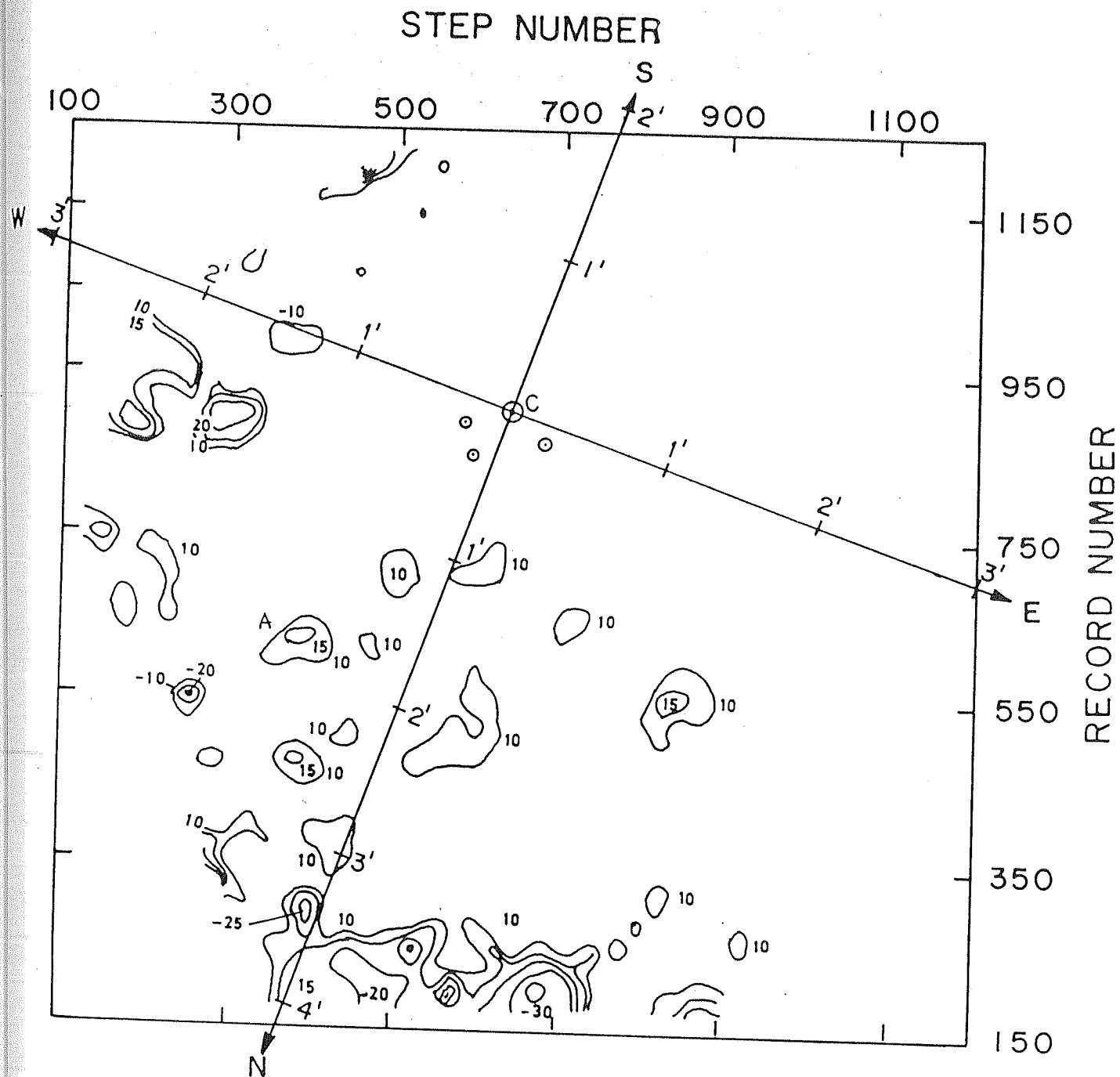
Fig. 6.5 Contour map of relative line of sight velocities of all the observed points; only those contours above the magnitude 10 km/s are shown; contour interval is 5 km/s. The contour A in the diagram matches with the position of the jet reported from the HST observation. Step number and record number indicate the parameters of digitization.

hot stars in the nebular interior drives an ionization front into the dense molecular cloud on the far side of the nebula; newly ionized gas is driven away from the front into the nebula by a strong pressure gradient and hence forms a flow or effusion, mainly directed towards the observer. Other weaker flows (tributaries) exist elsewhere in the nebula, in directions other than the main flow. In the central regions of the nebula Balick et al., find, predominantly positive velocities, which is attributed to the tributary flows. The contour diagram (Figure 6.5) show many contours of velocity $\sim +10$ km s^{-1} in the central regions of the nebula and hence our observation is consistent with the tributary flow model described by Balick et al. . The large velocity contours (~ -30 km s^{-1}) seen at the nebular boundaries lie in proximity to the HI-HII interface. They are probably the outflows associated with the ionization fronts which are directed towards the observer. Alternatively, they could be jets emanating from the embedded stars at the formation stage. However in the absence of other corroborative evidences it is difficult to give a complete interpretation of the results. The contour marked A in Figure 6.5, coincides with the jet reported by Hester et al., (1991), which is apparently associated with an embedded star. The gradient in the velocity seen from the north-west to the south-east could be due to the rotation of the Orion cloud A pointed out by Kutner et al., (1977), which will be reflected in the velocities, even after the averaging.

Stellar outflows are proposed as one of the plausible mechanism which drive the turbulence in the interstellar matter (Fukui et al., 1986). The mass of the gas added into the nebula by a typical flow of velocity 10 km s^{-1} having a flow diameter 0.02 pc is estimated to be $1M_\odot$, during its life time (Balick et al., 1980). The role of outflows in the dynamics of nebulae is very critical. The flows are known to be oriented towards the general field of magnetic field (Genzel & Stutsky 1989) and hence they are important from the point of view of energy balance in the nebula.

To summarize, we have carried out an observational study of some of the bright nebulae and in particular the Orion Nebula; the preliminary results obtained from such an exercise are reported. Large outflows of ionized gas are found both in the central regions and in the boundaries of the nebula, whose implications could be important in the nebular dynamics and energy balance. One of the velocity system observed, coincides with the jet reported from the HST observations, which is apparently associated with an embedded star. The observational study of the other nebulae such as Rosette, and Lagoon will be continued in the future.

Chapter 7

Summary and Conclusions

The thesis comprises studies on two diversified astrophysical situations; one on the outer envelope of a late-type star at its main sequence stage (solar corona) while the other on the ionized cloud surrounding an early-type star at its formation stage (the HII region-Orion Nebula). The thesis basically addresses the following problems; the nature of velocity fields in the solar corona, the excitation mechanism of the coronal green line and the kinematics of an HII region in the farthest regions from the ionizing star. The observations on the solar corona were carried out by the PRL group during the total solar eclipses of 1980 and 1983, using Fabry-Pérot interferometric techniques and coronal photography. The velocity fields in the corona were studied by a detailed analyses of the line profiles obtained from the eclipse interferograms. The spatial variations of the velocity field in the solar corona were examined in detail to see the influence of magnetic fields on coronal dynamics. The Variations in the coronal velocity fields associated with the solar cycle were also probed, to a limited

extent, by an inter-comparison of the results pertaining to the two eclipses. The excitation mechanism of the coronal green line was found out from the line to continuum intensity ratios derived from filter and white light photographs of the solar corona obtained during the 1980 total solar eclipse. The spatial variations of the excitation mechanism in the magnetic and non–magnetic regions were found out, from an analysis of data from various position angles on the corona. An observational study on the kinematics of an HII region was carried out in an emission line, which is predominant in the ionization front in a nebula. The preliminary results obtained from such a study are reported.

7.1   The Emission Line Profile Studies

- The present study indicates that the corona can be viewed as made up of, an ambient plasma medium with embedded discrete moving components associated with the coronal structures. The coronal line profiles, in general, show signatures of multicomponents. They are found to be a composite consisting of a main component and two or more subsidiary components. While the 1980 coronal line profiles show the presence of strong multicomponents, those of 1983 show the presence of weak components. When the line profiles show signatures of multicomponents, the velocity associated with the main component is found to be the least; this implies that subsidiary components in the line profile move with a relative velocity with respect to the main component. Since it is generally accepted that the average velocity in the inner corona does not exceed 10 $km\,s^{-1}$ (Newkirk 1967), we conclude that the main component in the line profile corresponds to the ambient coronal medium and the subsidiary components correspond to discrete moving plasma structures such as coronal loops, which

159

are seen in large numbers in the solar corona. The large velocity (0–100 $\mathrm{km\,s^{-1}}$) associated with the subsidiary components is due to velocity of mass motions inside the coronal loops.

- The average velocity of the ambient coronal plasma was found to be -5 $\mathrm{km\,s^{-1}}$ with a standard deviation ± 5 $\mathrm{km\,s^{-1}}$, for the 1980 solar maximum corona. For the declining activity phase of 1983, the average velocity associated with the ambient medium was found to be 0 ± 2.9 $\mathrm{km\,s^{-1}}$. The error involved in the measurement was ± 2 $\mathrm{km\,s^{-1}}$.

- The line of sight velocities associated with the fringe peaks and fringe centroids in the 1980 corona were found to increase with the coronal height which is mainly seen in the active regions. The magnitude of the increase is upto 16 $\mathrm{km\,s^{-1}}$ from 1.0 to 1.3 $R_\odot$. The result was found to be consistent with the model of subsonic siphon flow of plasma along the coronal flux tubes (Cargill & Priest 1980)

- A large excess of blue shifted components are seen in the 1980 coronal line profiles; this implies that the direction of motion of the plasma in coronal flux tubes is mostly directed towards the observer, at the solar maximum phase of 1980. The reason for the asymmetry is not very clear but one of the probable reasons may be due to the north-south asymmetry in the coronal activity with the northern hemisphere being more active.

- Line profiles belonging to various coronal regions are seen to be morphologically different, indicative of the different physical conditions existing in different regions. Whereas the line profiles from quiet and polar regions show evidences

of two or three components, the line profiles from the active regions show evidences of three or more components with strong subsidiary components. In active regions, the strength of the components being such that often it is not possible to distinguish the main component from the subsidiary components. Line splitting is seen in some of the active region line profiles.

• It was found that line profiles were best-fitted with multi-Gaussian models; the characteristics of the individual components in the line profiles were obtained from such models. The main component, found in the quiet and polar regions, is least shifted in velocity and it has the characteristics of the ambient coronal medium. The subsidiary components in the line profiles are found to have a velocities of magnitude 10–73 $km\,s^{-1}$, associated with them. The weak subsidiary components in the line profiles were found to have a large velocity (40 $km\,s^{-1}$ or more) associated with them and their half widths are equal to or more than that of the main component. The strong subsidiary components in the active regions have velocities $\sim 25\ km\,s^{-1}$; their half widths are much less than that of the main component. This implies that in active regions there are many coronal loops in which the temperature is much below (less than 10^6 K) than that of the ambient coronal plasma (2×10^6 K). The result agrees with the finding of Foukal (1975, 1976) who reported the existence of low temperature plasma at the coronal heights. The above result suggests that the physical conditions in the coronal loops and the ambient corona are more similar in the quiet and polar regions while they are very different in the active regions. The result also reiterates the role of magnetic fields in the dynamics of corona, by showing thermally isolated structures in the active region corona.

- The line profiles from the 1980 solar maximum corona show excess intensity in the wing regions, while similar excesses were not observed in the wing regions of the line profiles belonging to the 1983 corona. A typical coronal line profile as recorded by the Fabry-Pérot interferometer was modelled, to calculate the expected intensity at the wing regions which arise due to various factors. It was found that the excess intensity in the wing regions of Fabry-Pérot profiles arise due to the presence of fast moving ($\sim$100 km s^{-1}) discrete components in the corona. A covariation was observed in the fringe peak intensity and the excess wing intensity against the coronal radial distance in some of the position angles, where the coronal activity is found to be minimum. In the active regions the covariation between the two quantities was not seen indicative of the different physical conditions existing in the ambient coronal medium and in the coronal loops, a result which corroborates the earlier result.

- The coronal green line profile was modelled, by taking into account of the known physical quantities of the corona and the effect of mass motions inside coronal loops. The model line profiles successfully explain the main features in the observed line profiles. It is expected that more realistic models, with different loop sizes and loop orientations would agree with the observed line profiles more readily.

Future Studies:

- There have been only a few attempts regarding observational aspects on the kinematics of the inner solar corona. This remains one of the severe draw backs for the advancement of coronal science. A good data base on the temporal and spatial variations of the coronal temperature, velocity and magnetic field

is absolutely essential in order to have a better understanding of coronal phenomena. Because of its inherent advantages and relative ease of observation, the Fabry-Pérot interferometer still is, one of the best instrument for eclipse-based, kinematic studies of the corona. Instead of photographic film, imaging electronic detectors such as the Imaging Photon Detector (IPD) or Charge Coupled Device (CCD) could be used. The use of such devices having high quantum efficiencies and a wider dynamic range, not only improves the signal to noise ratio, but also makes the data reduction process relatively easier. Simultaneous observations in emission lines having different ionization potentials reveal the spatial variations of physical conditions in the corona in a better way. The coronal red line (FeX λ6374, IP 235 eV), green line (FeXV λ5303, IP 355 eV) and yellow line (CaXV λ5694, IP 820 eV) could be tried out as the useful probes of different coronal regions. The short-term coronal phenomena such as loop flows and MHD waves could be studied by observing the corona at regular intervals during an eclipse. Fabry-Pérot interferometric observations could be made at various places along the eclipse path, for such a study. It is also important to study the solar cycle variations of the corona; this may be done by observing the corona at different phases of solar activity cycle. One puzzling observation we find from our study is the excess blue shifts in the velocity in the solar maximum corona. It would be worthwhile to look for such asymmetries in the line profiles, which hopefully will be derived from the future observations. In theoretical models of the corona, it is very important to consider the asymmetries in mass motions since it appears that these arise from the basic MHD nature of the Sun.

• The modelling of the coronal green line profile, could be extended to more realistic coronal situations. In our modelling we have assumed only a single

coronal loop which is oriented along the line of sight; in reality, however, a large number of coronal loops with different physical properties such as loop size and flow velocities exist in them, with many possible orientations. Though the calculations become more complicated, it is expected that the resulting theoretical line profiles will show better agreement with the observed profiles.

7.2 Studies On The Coronal Green Line

- The excitation mechanism of the coronal green line was found out by theoretically calculating the line to continuum intensity ratio and by comparing it with the observed values of the ratio derived from the 5303 Å filtergram and a white light photograph of the corona. The line intensity refers to the total intensity in the line while the continuum intensity refers to the intensity per angström. In most of the coronal position angles, the excitation of the green line is mainly through collisional processes, in the inner regions (upto about 1.4 $R_\odot$) of the corona; the contribution from radiative mechanism was found to increase radially outwards through the corona. A very distinct evidence of the dominant radiative excitation was seen in the eastern active region beyond the radial distance 1.45 $R_\odot$ to about 1.60 $R_\odot$.

- The line to continuum intensity was calculated for the active, quiet and polar corona using the model electron density values given by Newkirk (1961) and for an isothermal corona of 2×10^6 K; the computed values were compared with the observed ratios from the respective coronal regions. The agreement between the theoretically computed and the observed values was fairly good, and on the basis of this the contributions from different excitation processes in the line

excitation were tabulated.

- The observed line to continuum intensity ratios are given for 30 coronal position angles, in the radial range 1.10–1.60 $R_\odot$. In active regions the value is found to be ~ 100 at 1.10 $R_\odot$; in streamers, the value is 30–40 and in polar regions it is less than 10 at the mentioned radial point. It may be concluded that the line to continuum intensity radios differ by two orders of magnitude, in the active and coronal hole regions at the solar maximum period of 1980.

Future Studies

- The coronal temperature could be found out more reliably from the line to continuum ratios than from the emission line widths. A comparison of the derived temperature with emission line widths would then provide the exact turbulent velocities in the corona.

7.3   Studies on the Orion Nebula (M42)

- A kinematical study of the Orion Nebula was carried out using Fabry-Pérot interferometric observations in the forbidden emission line, [SII]λ6731. The sulphur emission line is known to be prominent in the farthest regions of the nebula from the ionizing star especially in the HI- HII interface. The preliminary results obtained from the observational study is reported. The relative line of sight velocities were calculated at about 1500 points on the face of the nebula in a $6' \times 6'$ field around the Trapezium stars. The error involved in the measurement of relative velocity on individual points was ± 4 km s^{-1} . The relative line of

sight velocities averaged over a grid size of $10''$ on the face of the nebula ($1''$ corresponds to 0.0021 pc) are given. A contour map of all the observed velocities was obtained, to see the overall behaviour of the velocity pattern. The following results have emerged from the analysis; i) the velocities in the southern region of the Trapezium stars are small and are ~ 2 $km\,s^{-1}$. ii) the velocities are $\sim +10$ $km\,s^{-1}$ in the central regions of the Orion Nebula and iii) large velocities of ~ -30 $km\,s^{-1}$ lie in the nebular boundaries. These results generally agree with the flow model of Balick et al., (1980), where the complex pattern of velocity in the nebula is explained as a main flow directed towards the observer due to the effusion of ionized material from the molecular cloud plus the tributary flows, directed elsewhere. Large velocity contours seen at the nebular boundaries could be either due to the outflow from the ionization front in the HI-HII interface or due to the jets emerging from the embedded protostars. It was found that one of the velocity systems reported in our observations coincides with the jet reported by the Hubble Space Telescope observations; the average velocity of this jet was found to be ~ 17 $km\,s^{-1}$.

Future Studies

• Our knowledge about the star formation processes remains highly inadequate. Kinematical observations of the HII region provide very valuable information on the star formation. Imaging Fabry-Pérot observations in various emission lines of different ionization and an inter-comparison of the results will be very helpful to know more about the ionization fronts and the central regions. [SII] and [NII] lines are particularly useful as the probes of the ionization front in a nebula. In addition to the radial velocity studies, line profile studies in such lines are

absolutely essential, to know more about the kinetic temperature, turbulence in the nebula and the discrete motion fronts. It will be very rewarding to make line profile studies in faint emission lines using advanced electronic detectors and large telescope apertures. A comparison of the derived physical quantities from different HII regions, will be useful in knowing more about the star formation phenomenon in general, and about the various other related processes in the interstellar medium.

Bibliography

[1] Adams, J., Pneuman, G.W. 1976, Solar Phys., **46**, 185.

[2] Alfvén, H. 1963 in the Solar Corona, ed. J.W.Evans, p.35 New York, Academic Press.

[3] Allen, C.W. 1973, 'Astrophysical Quantities', The Athlone Press, London.

[4] Altschuler, M.D., Newkirk, G. 1969, Solar Phys., **9**, 131.

[5] Antonucci, E., Dodero, M.A. 1977, Solar Phys., **53**, 179.

[6] Antonucci, E., Svalguard, L. 1974, Solar Phys., **38**, 439.

[7] Ashbrook, J. 1975, Sky and Telescope, **50**, 299.

[8] Athay, R.G. 1976, 'The Solar Chromosphere and Corona: Quiet Sun', D. Reidel Pub. Co., p.192.

[9] Athay, R.G., Gurman, J.B., Henze, W. 1983b, Astrophys. J., **269**, 706.

[10] Athay, R.G., Gurman, J.B., Henze, W. Shine, R.A. 1983a, Astrophys. J., **265**, 519.

[11] Athay, R.G., Holzer, T.E. 1982, Astrophys. J., **255**, 743.

[12] Athay, R.G., White, O.R. 1977, Proc. OS08 Workshop, Nov. 1977, University of Colorado.

[13] Athay, R.G., White, O.R. 1978, Astrophys. J., **226**, 1135.

[14] Athay, R.G. White, O.R., Lites, B.W., Bruner, E.C. 1980, Solar Phys., **66**, 357.

[15] Atherton, P.D., Reay, N.K., Ring J., Hicks, T.R. 1981, Opt. Engg., **20**, 806.

[16] Axon, K., Taylor, K. 1983, Mon. Not.R. astr.Soc. **207**, 4.

[17] Balick, B., Gammon, R.H., Hjellming, R.M. 1974, P.A.S.P., **86**, 616.

[18] Balick, B., Gull, T.R., Smith, M.G. 1980, **92**, 22.

[19] Bessey, R.J., Liebenberg, D.H. 1984, Solar Phys., **94**, 239.

[20] Bhatnagar, A., Jadhav, D.B., Jain, R.M., Shelke, R.N., Purohit, S.P. 1982, Proc. Nat. Sci. Acad., **A48**, Suppl.3, 29.

[21] Biermann, L. 1946, Naturwiss., **33**, 118.

[22] Biermann, L. 1948, Z. Astrophys., **25**, 161.

[23] Billings, D.E. 1957, Astrophys. J., **125**, 817.

[24] Billings, D.E. 1959, Astrophys. J., **130**, 215.

[25] Billings, D.E. 1966, 'A Guide to the Solar Corona', Academic Press, New York.

[26] Boris, J.T., Marirka, J.T. 1982, Astrophys. J., 258, L49.

[27] Buisson, H., Fabry, C., Bourget, H. 1914, Astrophys. J., **40**, 241.

[28] Brueckner, G.E., 1980, Proc. XVII General Assembly of the IAU.

[29] Bugoslavskaya, E.Y. 1949, Publ. Sternberg Inst., **19**

[30] Cargill, P.J., Priest, E.R. 1980, Solar Phys., **65**, 251.

[31] Castaneda, H.O. 1988, Astrophys. J., Supp. **67**, 93.

[32] Celnik, W.E. 1985, Astron. Astrophys., **144**, 171.

[33] Chabbal, R. 1953, J.R.C.N.R.S., **24**, 138.

[34] Chandrasekhar T. 1982, Ph.D. Thesis, Gujarat University.

[35] Chandrasekhar, T., Ashok, N.M., Debi Prasad, C., Desai, J.N. 1988, Opt. Engg., Jan, **27**, 67.

[36] Chandrasekhar, T., Ashok, N.M., Desai, J.N., Pasachoff, J.M., Sivaraman, K.R. 1984, Appld. Opt., **23**, 508.

[37] Chandrasekhar, T., Desai, J.N., Angreji, P.D. 1981, Appl. Opt., **20**, 2172.

[38] Chandrasekhar, T., Desai, J.N., Ashok, N.M., Pasachoff, J.M. 1991, Solar Phys., **131**, 25.

[39] Chapman, S. 1957, Smithsonian Contributions to Astrophysics, **2**, 1.

[40] Cosmovici, C.B., Olthof, H., Strafella, F.F., Barbieri, C., Canton, G., D'Anna, E. 1979, Astron. Astrophys., **72**, 241.

[41] Cuperman, S., Sternliab, A. 1972, Solar Phys., **25**, 493.

[42] Debi Prasad, C. 1988, Ph.D. Thesis, Gujarat University.

[43] Deharveng, L. 1973, Astron. Astrophys., **29**, 341.

[44] Delone, A.B., Makarova, E.A. 1969, Solar Phys., **9**, 116.

[45] Delone, A.B. Makarova, E.A., 1973, Astron. Cirk., No.**772**, 1.

[46] Delone, A.B., Makarova, E.A. 1975, Solar Phys., **45**, 157.

[47] Delone, A.B., Makarova, E.A. Yakunina, G.V. 1988, J. Astrophys. Astr.,
9, 41.

[48] Desai, J.N. 1984, Proc. Indian Acad. Sci., (Earth Planet Sci) **93**, 189.

[49] Desai, J.N., Bhatt, H., Angreji, P.D., Patel, P., Pandya, P. Observations
of the Total Solar Eclipses of 16 Feb. 1980 (Prel. Results),1981, INSA,
New Delhi.

[50] Desai, J.N., Chandrasekhar, T. 1983, J. Astrophys. Astron. **4**, 65.

[51] Desai, J.N., Chandrasekhar, T., Angreji, P.D. 1982, J. Astrophys. Astr.,
3, 69.

[52] Desai, J.N., Raju, K.P., Chandrasekhar, T., Ashok, N.M., Pasachoff,
J.M. 1990, eds. Priest, E.R., Krishan, V., 'Basic Plasma Processes on the
Sun', D.Reidel, Dordrecht, p.251.

[53] Dollfus, A. 1953, Compt. Rend., **236**, 996.

[54] Dollfus, A., 1957, Compt. Rend., **244**, 1880-83.

[55] Dollfus, A. 1971, 'Physics of the Solar Corona', ed. Macris, C.J., (D.Reidel
Pub. Co., Dordrecht-Holland).

[56] Dopita, M.A., Gibbons, A.H., Meaburn, J. 1973, Astron. Astrophys., **22**, 33.

[57] Doschek, G.A., Feldman, U. 1977, Astrophys. J., **212**, L143.

[58] Doschek, G.B., Mariska, J.T. Feldman, U. 1981, Mon. Not. Roy. astr. Soc., **195**, 107.

[59] Dulk, G.H., Mclean, D.J. 1978, Solar Phys., **57**, 279.

[60] Dürst, J. 1982, Astron. Astrophys., **112**, 249.

[61] Edlén, B. 1942, Z. Astrophys., **22**, 30.

[62] Elliot, K.H., Meaburn, J. 1973, Astron. Astrophys., **27**, 367.

[63] Elliot, K.H., Meaburn, J. 1974, Astrophys. Space Sci., **28**, 351

[64] Elliot, K.H., Meaburn, J. 1975, Astrophys. Space Sci., **35**, 1575.

[65] Elmegreen, B.G., Lada, C.J. 1977, Astrophy. J., **214**, 725.

[66] Fabry, C., Buisson, H. 1911, Astrophys. J., **33**, 406.

[67] Fisher, R.R. 1978, Solar Phys., **57**, 119.

[68] Fisher, R.R., Musman, S. 1975, Astrophys. J., **195**, 801.

[69] Foukal, P.V. 1975, Solar Phys., **43**, 327.

[70] Foukal, P.V. 1976, Astrophys. J., **210**, 575.

[71] Fukui, Y., Sugitani, K., Takaba, H., Iwata, T., Mizuno, A. et al., 1986, Astrophys. J., **311**, L85.

[72] Genzel, R., Stutzky, J. 1989, Ann. Rev. Astron. Astrophys., **27**, 41.

[73] Gibson, E.G. 1973, 'The Quiet Sun', (NASA SP 303, Washington).

[74] Gnevyshev, M.N. 1967, Solar Phys., **1**, 107.

[75] Gokhale, M.H. 1975, Solar Phys., **41**, 381.

[76] Goldberg, L. 1967, Ann. Rev. Astron. Astrophys., **5**, 279.

[77] Goudis, C., Hippelein, H., Meaburn, J., Songsathaporn, R. 1984, Astron. Astrophys., **137**, 245.

[78] Grandi, S.A. 1975, Astrophys. J., **196**, 465.

[79] Grotrian, W. 1933, Z. Astrophys., **7**, 26.

[80] Habbal, S.R., Ronen, R., Withbroe, G.L. 1985, Solar Phys., **98**, 323.

[81] Habing, H.J. 1974, The Interstellar Medium, p.91-125.

[82] Hanel, A. 1987, Astron. Astrophys., **176**, No.2, 338.

[83] Harvey, J., Livingston, W. 1981, 'International Symp. on Solar Eclipse', Late Abstracts, (INSA, New Delhi), p.2.

[84] Hasan, S.S., Schussler, M. 1985, Astron. Astrophys., **151**, 69.

[85] Heiles, C., Troland, J.H. Astrophys. J. 1982, **263**, 130.

[86] Hernandez, G. 1966, Appl. Opt., **5**, No.11, 1745.

[87] Hester, J.J., Gilmozzi, R., O'Dell, C.R., Faber, S.M., et al., 1991, Astrophys. J., **369**, L75.

[88] Hildner, E., Livingston, W.C., 1975, Solar Phys., **42**, 391.

[89] Hinata, S. 1979, Astrophys. J., **232**, 915.

[90] Hinata, S. 1980, Astrophys. J., **235**, 258.

[91] Hirschberg, J.G., Wouters, A., Hazelton, L. Jr. 1971, Solar Phys., **21**, 448.

[92] Hood, A.W., Priest, E.R., 1979, Astron. Astrophys., **77**, 233.

[93] Ionson, J.A. 1978, Astrophys. J., **226**, 650.

[94] Jacquinot, P. 1954, J. Opt. Soc. Am., **44**, 761.

[95] Jacquinot, P. 1960, Rep. Prog. Phys., **24**, 267.

[96] Jarrett, A.H., Von Klüber, H. 1955, Mon. Not.R. astr. Soc., **115**, 343.

[97] Jarrett, A.H., Klüber, H. von. 1961, Mon. Not. R. astr. Soc., **122**, 223.

[98] Jordan, C. 1969, Mon. Not. R. astr. Soc., **142**, 501.

[99] Jordan, C. 1975, in S.R. Kane (ed.) 'Solar Gamma, X- and EUV Radiation', IAU symp. **68**, 109.

[100] Kaler, J.B. 1969, Astrophys. J., **148**, 925.

[101] Kalinijak, A.A. 1949 in Trudy expedicii nabludenij polnogo solnechnogo zatmeniy 21 sentijbiy 1941 goda, Moskow, p.352.

[102] Kim, I.S., Nikolsky, G.M. 1975, Solar Phys., **43**, 351.

[103] Kopp, R.A., Orrall, F.Q. 1976, Astron. Astrophys., 53, 363.

[104] Kopp, R.A., Pnueman, G.W. 1976, Solar Phys., **50**, 85.

[105] Kopp, R.A., Poletto, G., Noci, G., Bruner, M. 1985, Solar Phys., **98**, 91.

[106] Koutchmy, O., Koutchmy, S., Nitschelm, C., Sykora, J., Smartt, R.N. 1988, Proc. of Sac. Peak Summer Workshop on Solar and Stellar Coronal Structure and Dynamics, ed. Altrock.

[107] Kuperus, M., Ionson, J.A., Spicer, D.S. 1981, Ann. Rev. Astron. Astrophys., **19**, 7.

[108] Kushman, G.W., Pense, W.A. 1976, Astrophys. J., **207**, L61.

[109] Kutner, M.L., Tucker, K.D., Chin, G., Thaddeus, P. 1977, Astrophys. J., **215**, 521.

[110] Lee, P. 1969, Astrophys. J., **157**, L111.

[111] Levine, R.H. 1974, Astrophys. J., **190**, 457.

[112] Liebenberg, D.H. 1975, Solar Phys., **44**, 331.

[113] Liebenberg D.H., Bessey, R.J. Watson, B. 1975, Solar Phys., **44**, 345.

[114] Lilliequist, C.G., 1966 (Paper presented at October meeting A.A.S.).

[115] Livingston, W., Harvey, J. 1982, Proc. Indian Nat. Sci. Acad., **A48**, Suppl.3, 18.

[116] Livingston, W., Harvey, J., Doe, L.A. 1970, Solar Eclipse 1970 Bulletin. F., 72.

[117] Loren, R.B. 1979, Astrophys. J., **234**, L207.

[118] Loucif, M.L., Koutchmy, S. 1989, Astron. Astrophys. Suppl. Ser. **77**, 45-66.

[119] Lyot, B. 1937, L'Astronomie, **51**, 203.

[120] Mariska, J.T. 1984, Astrophys. J., 435.

[121] Moussas, K., Papastamotiou, N., Rusin, V., Rybansky, M. 1983, Solar Phys., **84**, 71.

[122] Marshall, P., Henderson, G., 1973, Solar Phys., **33**, 153.

[123] Mason, H.E. 1975, Mon. Not. R. astr. Soc., **170**, 651.

[124] McCall, M.L. 1979, Astrophys. J., **229**, 962.

[125] McWhirter, R.W.P., Thoneman, P.C., Wilson, R. 1975, Astron. Astrophys., **40**, 63.

[126] Meaburn, J. 1971, Astrophys. Space Sci., **13**, 110.

[127] Meaburn, J. 1975, 'HII Regions and Related Topics', Lecture Notes in Physics, **42**, 224 (Berlin:Springer-Verlag).

[128] Meaburn, J. 1976, 'Detection and Spectrometry of Faint Light', D.Reidel, Dordrecht, Holland.

[129] Mein, N., Mein, P. 1980, Astron. Astrophys., **84**, 96.

[130] Mein, P., Simon, G., Vial, J.C., Shine R.A. 1982, Astron. Astrophys., **111**, 136.

[131] Melnick, G., Gull, G.E., Harwit, M. 1979, Astrophys. J., **227**, L29.

[132] Meyer, F., Schmidt, H.U. 1968, Z. Angew. Math. Mech. **48**, 218.

[133] Narain, U., Ulmschneider, P. 1990, **54**, 377.

[134] Ness, N.F., Scearce, C.S., Seek, J.B., 1963, J. Geophys. Res., **69**, 3531.

[135] Newkirk, G., 1961, Astrophys. J., **133**, 983.

[136] Newkirk, G., 1967, Ann. Rev. Astron. Astrophys. **5**, 213.

[137] Noci, G. 1981, Solar Phys., **69**, 63.

[138] Noxon, J.F., 1966, Astrophys. J., **145**, 400.

[139] O'Dell, C.R. 1985, Bull. Am. Astron. Soc., **17**, No.4, p.891.

[140] O'Dell, C.R. 1986, Astrophys. J., **304**, No.2, p.6767.

[141] O'Dell, C.R., Townsley, L.K., Castaneda, H.O. 1987, Astrophys. J., **317**, No.2, p.676.

[142] Osterbrock, D.E. 1961, Astrophys. J., **134**, 347.

[143] Osterbrock, D.E. 1974, 'Astrophysics of Gaseous Nebulae', (Freeman, San Francisco).

[144] Pankonin, V., Walmsley, C.M., Harwit, M. 1979, Astron. Astrophys., **27**, 367.

[145] Parker, E.N. 1955, Astrophys. J., **122**, 293.

[146] Parker, E.N. 1960, Astrophys. J., **132**, 821.

[147] Parker, E.N. 1983, Astrophys. J., **264**, 642.

[148] Parker, E.N. 1986, in 'The Sun and the Heliosphere in Three Dimensions', ed. R.G.Marsden (Dordrecht-Reidel).

[149] Parker, E.N. 1987, Physics Today, **40**, No.7, 36.

[150] Parker, E.N. 1990, Adv. Space Res., **10**, No.9, 77.

[151] Pasachoff, J.M., Landman, D.A. 1984, Solar Phys., **90**, 325.

[152] Pathak, P.N. 1972, Solar Phys., **25**, 489.

[153] Pecker, C., Billings, D.E., Roberts, W.O. 1954, Astrophys. J., **120**, 509.

[154] Peraiah, A., Varghese, B.A. 1989, Solar Phys., **124**, 53.

[155] Petropoulos, B. 1988, Solar Phys., **115**, 367.

[156] Poletto, G. 1981, Solar Phys., **73**, 233.

[157] Press, W.H., Flannery, B.P., Teukolsky, S.A., Vetterling, W.T. 1986, 'Numerical Recipe', Cambridge University Press.

[158] Priest, E.R. 1984, 'Solar Magnetohydrodynamics', D.Reidel, Holland.

[159] Raju, K.P., Desai, J.N., Chandrasekhar, T., Ashok, N.M. 1991, J. Astrophys. Astr., **12**, 311.

[160] Raju, P.K., Singh J. 1987, Solar Phys., **110**, 271.

[161] Roberts, B. 1987, solar magnetohydrodynamics in 'Cometary and Solar Plasma Physics', ed. B. Buti, World Scientific, USA.

[162] Rosner, R., Golub, L., Coppi, B., Vaiana, G.S. 1978, Astrophys. J., **222**, 317.

[163] Rosner, R., Tucker, W.H., Vaiana, G.S. 1978, Astrophys. J., **220**, 643.

[164] Roy, J.R., Arsenault, R., Joncas, G. 1986, **300**, No.2, p.624.

[165] Rusin, V., Rybansky, M. 1983, Bull. Astron. Inst. Czechosl., **34**, 257.

[166] Rybansky, M., Rusin, V., Dermendiev, V., Buyukliev, G. 1986, Bull. Astron. Inst. Czechosl. **37**, 253.

[167] Sahu, K.C., Desai, J.N., Kamble, V.B., Mehta, V. 1981, Bull. Astron. Soc. India, **9**, p.69.

[168] Schatzman, E. 1949, Ann. Astrophys., **12**, 203.

[169] Scheffler, H., Elsässer, H. 1988, 'Physics of the Galaxy and Interstellar Matter', Springer-Verlag Berlin Heidelberg.

[170] Schmidt, H.U. 1964, W. Hess (ed), NASA Symp. on Physics of Solar Flares, NASA, SP-50, p.107.

[171] Schwarzchild, M. 1948, Astrophys. J., **107**, 1.

[172] Shu, F. 1982, 'The Physical Universe: An Introduction to Astronomy', University Science Books, Mill Valley, California.

[173] Singh, J. 1984, Ph. D.Thesis, Punjabi University, Patiala.

[174] Singh, J. 1985, Solar Phys., **95**, 253.

[175] Singh, J., Bappu, M.K.V. Saxena, A.K. 1982, J. Astrophys., Astr., **3**, 249.

[176] Smartt, R.N., Zhang, Z. 1987, NASA Conf. Publ., NASA CP-2453, p.129.

179

[177] Smith, M.G., Weedman, D.W. 1971, Astrophys. J., **169**, 271.

[178] Strömgren, B. 1939, Astrophys. J., **89**, 526.

[179] Sugitani, K., Fukui, Y., Ogawa, H., Kawabata, K. 1986, Astrophys. J., **303**, 667.

[180] Taylor, K., Munch, G. 1975, P.A.S.P, **87**, 509.

[181] Tenorio-Tagle, G. 1979, Astron. Astrophys., **71**, 59.

[182] Thorne, A.P. 1974, 'Spectrophysics', Chapman and Hall, Science Paper backs, London.

[183] Tsubaki, T., 1975, Solar Phys., **43**, 147.

[184] Tsubaki, T., 1983, Solar Phys., **87**, 57.

[185] Tucker, W. 1973, Astrophys. J., **186**, 285.

[186] Uchida, Y., Sakurai, T. 1977, Solar Phys., **51**, 413.

[187] Ulmschneider, P. 1976, Solar Phys., 49, 249.

[188] Ushakov, A.N., Yaroslavsky, L.P., Delone, A.B., Makarova, E.A., Yakunina, G.V., Charusin, V.M., Dagaev, M.M., Degulev, V.S. 1984, Astron. Cirk., No.1340, 2.

[189] Vaiana, G.S., Rosner, R., 1978, Ann. Rev. Astron. Astrophys. 16, 393.

[190] Van Ballegooijen, A.A. 1986, Astrophys. J., **511**, 1001.

[191] Van de Hulst, H.C. 1953, 'The Chromosphere and corona' in the Sun, ed. Kuiper, G.P., Uni. of Chicago Press, Chicago.

[192] Wagner, W.J. 1984, Ann. Rev. Astron. Astrophys., **22**, 267.

[193] Waldmeier, M. 1942, Z. Astrophys., **22**, 1.

[194] Waldmeier, M.., 1945, Mitt. der Aarg Natur. Ges. **22**, 185.

[195] Waldmeier, M., 1947, Astron. Mitt. Zurich, No.151.

[196] Waldmeier, M. 1971, Solar Phys., **20**, 332.

[197] Waldmeier, M. 1975, Solar Phys., **45**, 147.

[198] Waldrop, M.M. 1982, Science, **215**, 647.

[199] Wang, P.K., Siscoe, G.L. 1980, Solar Phys., **66**, 187.

[200] White, G.J., Phillips, J.P. 1988, Astron. Astrophys., **197**, 253.

[201] Wilson, O.C., Munch, G., Flather, E.M., Coffeen, F. 1959, Astrophys. J. Supp., **4**, 199.

[202] Withbroe, G.L., Noyes, R.W. 1977, Ann. Rev. Astron. Astrophys., **15**, 343.

[203] Wolfson, R. 1983, Sci. Am. **248**, No.2, p.86.

[204] Yaroslavisky, L.P., Ushakov, A.N., Delone, A.B., Makarova, E.A., Yakunina, G.V., Charusin, V.M., Dagaev, M.M., Jegulev, V.S. 1986, in Resultaty nabludeniy solnechnogo zatmeniy 31 iuliy 1981, goda, VAGO, Moskow, p.54.

[205] Zirin, H., 1959, Astrophys. J., **129**, 414.

[206] Zirin, H. 1971, Phil. Trans. Roy. Soc. Lond. A., **270**, 183.

[207] Zirin, H. 1988, 'Astrophysics of the Sun', Cambridge Univ. Press, p.235.

[208] Zirker, J.B. 1980,' Total Eclipses of the Sun', van Nostrand Rienhold, Newyork.

[209] Zuckerman, B. 1984, Nature, **309**, No.5967, p.403.

[210] Zuckerman, B. 1973, Astrophys. J., **183**, 868.